Study of impulsive magnetic reconnection due to resistive tearing mode with the effect of viscosity and dynamic flow in fusion plasmas

Ahmad Ali

Abstract

Magnetic reconnection is a ubiquitous plasma process which plays a vital role in a wide range of phenomena in the universe, including the relaxation events of fusion plasmas, the dynamics of Earth's magnetosphere and the evolution of solar flares. All these phenomena exhibit an impulsive magnetic reconnection, where the slow build up phase is followed by an abrupt release of magnetic energy, resulting in a sudden increase of the reconnection rate. Tearing mode and sawtooth crashes are the typical examples of the impulsive reconnection in fusion plasmas. This thesis is thus devoted to understand the complex nonlinear dynamics of the tearing instability under various plasma conditions.

In the limit of large instability parameter Δ' (strongly driven regime), the nonlinear dynamics of resistive tearing mode exhibit an abrupt growth phase after the Rutherford's slow nonlinear phase, which is accompanied by a collapse of the typical X-point configuration to Y-type current sheet. The trigger mechanism for the X-point collapse, leading to the explosive growth dynamics is still an unresolved problem. Furthermore, the role of viscosity in the transition from the slow growth phase to the abrupt phase has not been considered in the previous works. One part of this thesis is thus dedicated to investigate the trigger mechanism for the X-point collapse and the role of viscosity in such process. For this purpose, we propose a secondary instability analysis based on the quasilinear modification of the equilibrium profile by the zonal current. The results show that the current peaking effect is plausibly responsible for the onset of the X-point collapse and the current sheet formation, leading to the explosive growth of reconnected flux. The effect of viscosity is then explored directly through linear and nonlinear simulations. It is observed that in the presence of finite viscosity, the scaling of critical island width for the X-point collapse $\Delta' w_c$ with the resistivity gets modified. A transition behavior is revealed at $P_r \approx 1$ for the viscosity dependence of $\Delta' w_c$ and the linear tearing instability.

In the other main part of this thesis, we analyze the effects of an imposed dynamic flow on the magnetic reconnection process. Results show that while the linear stability properties of the resistive tearing mode are moderately affected by the dynamic flow, the

nonlinear evolution is significantly modified by the radial parity, frequency and amplitude of the dynamic flow. After the Rutherford's slow nonlinear stage, the reconnection process is found to progress in two phases by including the dynamic flow. A Sweet-Parker like current sheet is formed in the first phase and plasmoid instability is triggered in the second phase, where multiple plasmoids are continuously generated and ejected along the current sheet, leading to a bursty impulsive reconnection. It is observed that onset and evolution of the plasmoid instability are strongly influenced by the frequency and radial parity of the dynamic flow. Most importantly, the effective reconnection rate is found to be independent of resistivity by including the dynamic flow.

Keywords: Magnetic reconnection, resistive tearing mode, X-point collapse, secondary instability, dynamic flow, plasmoid instability, impulsive reconnection.

Acknowledgments

First of all, I would like to express sincere thanks to my supervisors Prof. Yasuaki Kishimoto and Prof. Jiquan Li, who gave me the opportunity to pursue my PhD research in Kyoto University and who always supported me throughout my study. I am very much thankful to them for their generosity in sharing their knowledge and for keeping faith in my research. Prof. Yasuaki Kishimoto always encouraged me and gave me appropriate guidance how to pursue scientific research. I would like to pay special thanks to Prof. Jiquan Li, for his continuous input to improve my numerical skills and physical understanding of the magnetic reconnection phenomena. I would like to appreciate Prof. Kenji Imadera for his guidance regarding the use of supercomputer and other lab affairs. I am also very indebted to my two reviewers, Prof. Nakamura and Prof. Maekawa, who accepted to review this work.

Sincere thanks to all the members of our lab, especially to Paul and Mao for their help and fruitful discussions on the numerical study of magnetic reconnection. I am very much grateful to Ms. Nakamura, who always willingly helped me in paper work and other daily life issues.

I was quite lucky to have many nice friends during the early days in Japan. I would like to specially thank Kanstantin, Qoroush and Li Jia for spending their precious time with me to enjoy the weekend together by exploring the beauty of Kyoto. I am very much indebted to my friends Rafiq Ahmad and Iftikhar Ahmad, who shared with me the tears and joys of life in Japan. They helped me a lot in hardest times of my life in Japan, when I made a bicycle accident. Thank you all, for making my life joyful and comfortable in Japan.

Finally, I would like to pay my deepest love and gratitude to my parents and my wife, who always encouraged me during my stay in Japan. Also, I appreciate other members of my family, my sisters and brother. Their pray were a great source of power for me to work hard in my studies and get success. I owe them a lot.

Contents

Chapter 1

Introduction

The energy crisis is one of the biggest challenge world is facing in the 21st century. The energy demand by the mankind is continuously increasing due to the growing world population and fast industrial development of the emerging countries.

At present, most of the world energy is produced by burning the fossil fuels. Besides being limited resources, fossil fuels are seriously affecting earth's climate. It has been found that burning of fossil fuels is the largest source of carbon dioxide emission, which leads to global warming. To meet the energy needs of the growing world population in a sustained manner, we have to look for alternative energy resources which are virtually unlimited, worldwide accessible and most importantly, pose minimum threat to our environment. Fusion energy is one of the best candidates for supplying the future energy demands in a safe and clean manner. Fusion energy is considered as the best promising future energy option because it can provide safe and clean energy, with many other important advantages. These include: practically inexhaustible and globally accessible fuel resources; no emission of green house gases; lesser consumption of the fuel than the other energy resources for producing the same amount of energy; no issue of long lived radioactive waste (compared to the fission energy); and inherently safe. Current studies predict that the cost of electricity generated by the fusion could be comparable to that obtained from other energy resources [1].

In the next 20-30 years, the nuclear fusion technology is expected to establish itself through the development of ITER (International Thermonuclear Experimental Reactor) and DEMO (Demonstration Power Plant). Thus in the long-run, fusion power is likely to become commercially available and play a significant role in supplying the future energy demands of the world.

1.1. The Basics of Nuclear Fusion

The stars and the sun are excellent examples of nuclear fusion around us. The sun is made of hot dense plasma confined by its gravity, radiates a tremendous amount of energy to the earth which is produced by fusion reactions. Basically, nuclear fusion is the process in which two light nuclei combine or fuse to form a more tightly bound heavier nucleus. As a result, considerable amount of energy is released. The total mass after the nuclear reaction is less than before and the missing mass "Δm" appears in the form of energy according to the well known Einstein's law $E = \Delta m c^2$.

1.1.1. Fusion Reactions

The most promising fusion reaction to carry out for the energy production in the present day magnetic fusion devices, is that between the deuterium D (${}^{2}_{1}\mathrm{H}$) and tritium T (${}^{3}_{1}\mathrm{H}$). The possible reactions involving D and T are as follows [2-4]:

$$\mathrm{D} + \mathrm{T} \longrightarrow {}^{4}_{2}\mathrm{He} + \mathrm{n} + 17.6\mathrm{MeV} \quad (1.1)$$

$$\mathrm{D} + \mathrm{D} \longrightarrow \mathrm{T} + \mathrm{p} + 4.03\mathrm{MeV} \quad (1.2)$$

$$\mathrm{D} + \mathrm{D} \longrightarrow {}^{3}_{2}\mathrm{He} + \mathrm{n} + 3.27\mathrm{MeV} \quad (1.3)$$

$$\mathrm{D} + {}^{3}_{2}\mathrm{He} \longrightarrow {}^{4}_{2}\mathrm{He} + \mathrm{p} + 18.3\mathrm{MeV} \quad (1.4)$$

In the D-T reaction a total energy of 17.6MeV is produced which comes out in the form of kinetic energy of neutron (14.1MeV) and alpha particle (3.5MeV). Deuterium can be easily extracted from the sea water, where it exists at 0.0153%, representing an unlimited fuel source. The other element needed for the D-T reaction is tritium. Tritium undergoes beta decay with a half life of 12.5 years and thus is not available naturally, but can be produced artificially from lithium [2-4]. Fortunately, ${}^{6}_{3}\mathrm{Li}$ is an abundant isotope, consisting 7.5% of the naturally occurring lithium. The nuclear reactions for tritium production are [2]:

$$\mathrm{n} + {}^{6}_{3}\mathrm{Li} \longrightarrow \mathrm{T} + {}^{4}_{2}\mathrm{He} \quad (1.5)$$

$$\mathrm{n} + {}^{6}_{3}\mathrm{Li} \longrightarrow \mathrm{T} + {}^{4}_{2}\mathrm{He} + \mathrm{n} \quad (1.6)$$

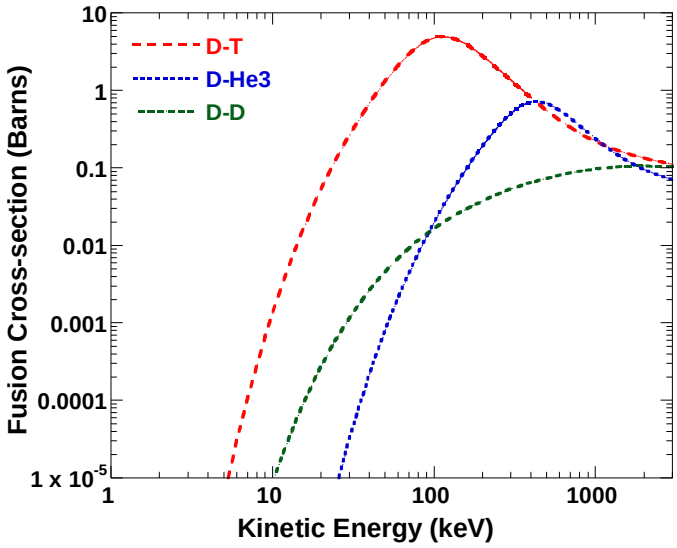

Figure 1.1: Fusion cross-section of various fusion reactions against the kinetic energy of the incident particle. Data for the D-D reaction is taken from ENDF database [5], whereas D-T and D-He cross-sections are calculated using NRL plasma formulary [6].

In order to induce the fusion reaction, the two nuclei must have enough kinetic energy to overcome the strong electrostatic repulsive force acting between them and must approach each other close enough that the short range strong nuclear force becomes dominant. The probability of collision between two particles is usually described in terms of the reaction cross-section (σ). The collision cross-section curves for the most common fusion reactions are plotted in Figure 1.1, which shows that the D-T reaction has the largest cross-section at around 100keV; much higher than the peak cross-sections of the other reactions. This means that for a significant fusion rate, the D-T fuel must be heated to very high temperatures of the order of 100 million degree C. At such high temperatures, the gas consists in the form of ions and free electrons, which is known as plasma. Thus, heating the plasma to very high temperatures and confining it for a sufficiently long time, are the two major scientific challenges in achieving continuously stable fusion energy [2-4].

1.1.2. Confinement of Fusion Plasma

In case of sun, the plasma is dense enough to provide the required gravitational force for confinement. However, this method of plasma confinement is not appropriate in fusion reactors on earth, where the gravitational force is much weaker. Therefore, to confine the hot plasma for fusion energy, new ways had to be explored. At present, mainly two experimental approaches are being studied for building a fusion reactor: inertial and magnetic confinement.

In inertial confinement, a small pellet containing fusion fuel is compressed and heated by the high power lasers or particle beams so quickly that it reaches the conditions required for the fusion reaction. The inertia of the fuel is responsible for the confinement; hence it is named the inertial confinement fusion (ICF). The fusion reactor based on inertial confinement would work in pulsed manner. However, this method still needs more efforts to make the fusion power commercially available.

In magnetic confinement, strong magnetic fields are used to confine the hot plasma. Basically, this utilizes the ability of a steady magnetic field to allow the motion of charged particles in plasma along the magnetic lines of force and restricts their motion in the transverse direction. Hence, in magnetized plasma the charged particles would follow the magnetic field lines and gyrate around them. A lot of progress has been made in the area of magnetically confined fusion. The most successful device for confining the fusion plasma has been developed by the magnetic confinement fusion based on the concept of Tokamak.

1.1.3. The Tokamak Concept

Tokamak is considered as the most successful device of present days for harnessing the fusion power. The schematic diagram of a tokamak configuration is shown in Figure 1.2. The outer ring-like coils, arranged in the form of a torus, produces the toroidal magnetic field, B_T. This toroidal field confines the plasma in torus shape. However, additional field is required in the poloidal direction, to eliminate the charge separation due to the particle drifts. Such a poloidal magnetic field B_P is produced by a central solenoid. Actually, the solenoid induces plasma current along the torus through transformer action, which then

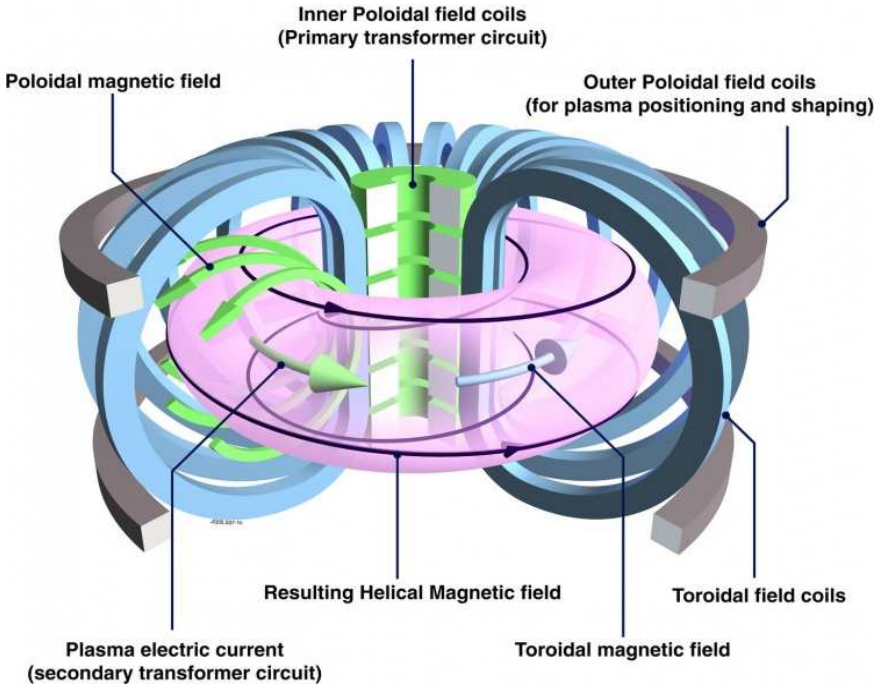

Figure 1.2: Schematic of a tokamak. Figure from Eurofusion website [7].

gives rise to the poloidal magnetic field. The combination of the toroidal and poloidal magnetic fields results in a net helical magnetic field, which confines the hot plasma. In addition to the toroidal field coils and solenoid, equilibrium field coils are also needed to provide a radially inward force on the plasma to balance the hoop force. At higher temperatures the ohmic heating becomes less effective and is limited up to 1keV [2]. Thus additional heating sources such as ion cyclotron resonance heating (ICRH), electron cyclotron resonance heating (ECRH) and neutral beam injection (NBI) are required to raise the plasma temperatures to fusion relevant temperatures.

In order to commercialize the fusion reactor, it is essential to achieve a net positive energy balance, that is described in terms of the fusion energy gain factor Q, defined by the ratio of fusion power to input power, i.e. $Q = P_f/P_{in}$, where the condition $Q = 1$ is known as breakeven. In 1991, the joint European torus (JET) situated in Unite Kingdom, achieved the world's first release of the controlled fusion energy. Currently, it is the only tokamak in

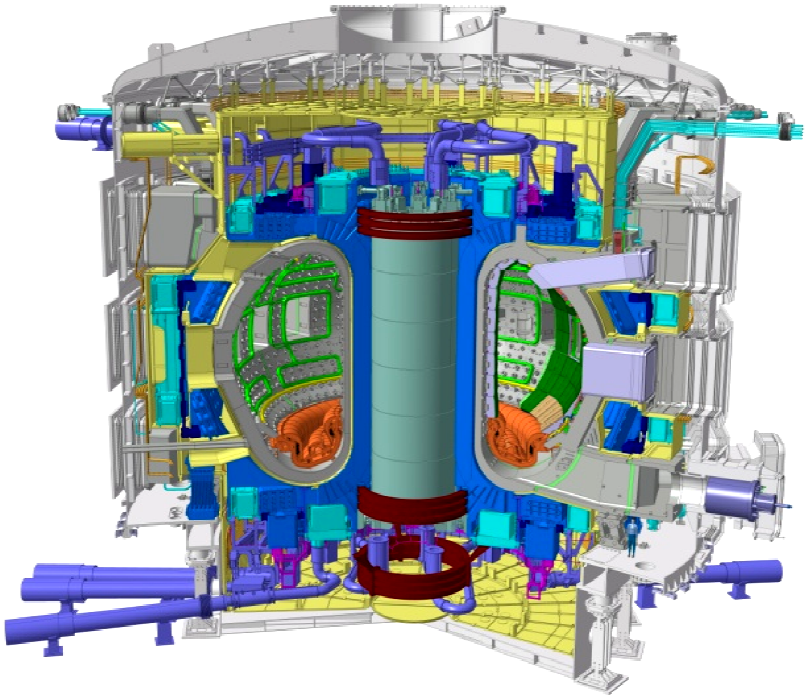

Figure 1.3: Schematic of ITER tokamak. The figure is taken from ITER organization website [8].

the world, using the D-T fuel. In 1997, JET achieved $Q = 0.65$ with an output power of 16MW [9]. Soon after, in 1998, JT-60U in Japan, achieved $Q = 1.25$ [10]. The next generation tokamak, ITER, is designed to achieve $Q = 10$ with a power of 500 MW. ITER is a large scale scientific project that involves international collaboration among China, the EU, Japan, India, Korea, Russia and the United States. In June 2005, the seven ITER Members decided to build the next generation reactor at Cadarche, France. The schematic of ITER tokamak is shown in Figure 1.3. ITER is not the end; the next generation commercial reactor, DEMO is in the conceptual phase and is expected to become operational in 2030's [8].

Although the tokamak configuration is promising for harnessing the fusion power, the stable confinement of hot plasma is still an unresolved issue. Magnetic reconnection changes the magnetic field topology; resulting in the formation of magnetic islands, which can significantly degrade the plasma confinement by increasing the transport of heat and

particles across the radial direction. Tearing mode and sawtooth crashes are the classic examples of magnetic reconnection in fusion devices [11]. Understanding the complex dynamics of resistive instabilities in plasma confinement devices is of utmost importance for the efficient and stable operation of the next generation large scale fusion reactors such as ITER. The remaining part of this chapter is devoted to an overview of the magnetic reconnection problem, focusing on the resistive tearing mode dynamics.

1.2. Magnetic Reconnection

Magnetic fields are observed in almost every plasma at all scales in the universe, from the magnetosphere to the interstellar medium and distant galaxy clusters. The existence of these fields in dynamic plasmas leads to the process of magnetic reconnection, which causes rearrangement of the topological structure of the magnetic field lines. During this process, magnetic energy is converted to kinetic and thermal energies of the charged particles. Magnetic reconnection is the key mechanism behind many astrophysical events such as the solar flares, coronal mass ejection and magnetospheric substorms. The aurorae are also believed to be related to the magnetic reconnection in the Earth's magnetosphere [12-15].

Magnetic reconnection is considered to be responsible for the occurrence of sawtooth crashes in tokamaks [16-18]. Moreover, it occurs in relaxation processes in reverse field pinch (RFP) and spheromak plasmas [19, 20]. The concept of magnetic reconnection was first proposed by Giovanelli in 1946 [21], to explain the mechanism for the abundant release of magnetic energy in the solar flares. Since then, magnetic reconnection has been recognized as one of the fundamental processes in the magnetized plasmas and has attracted extensive research efforts.

1.2.1. When does the Magnetic Reconnection Occur?

To understand the basic concept of the magnetic reconnection, let us first explicate the magnetic flux freezing constraint. In the case of highly conducting plasma (i.e. ideal MHD), the magnetic field lines are frozen to the plasma in which it is embedded. It means that as the plasma moves, the field lines follow it and the topology of the magnetic field

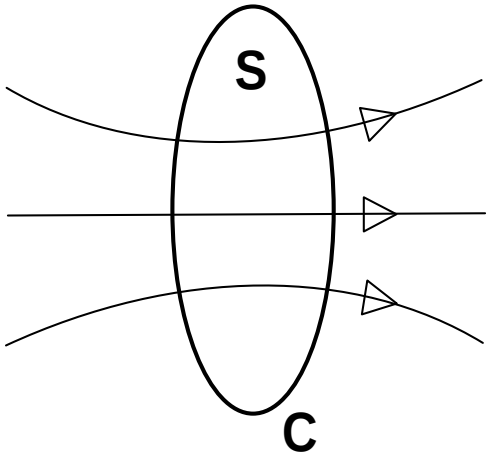

Figure1.4: The magnetic field lines configuration in a plasma tube.

remain invariant: this phenomenon is known as the flux freezing. In order to prove the validity of flux freezing condition, we consider the time behavior of the magnetic flux Φ_m, through an open surface S bounded by a curve *C* as shown in Figure 1.4. The magnetic flux though surface *S* is defined as [13-14]:

$$\Phi_m = \int_S B \cdot dA \tag{1.7}$$

The rate of change of this magnetic flux depends on the time variation of the magnetic field itself and the change of the curve *C* due to the plasma motion v; i.e.,

$$\frac{d\Phi_m}{dt} = \int_S \frac{\partial B}{\partial t} \cdot dA - \int_C \boldsymbol{v} \times B \cdot d\boldsymbol{l} \tag{1.8}$$

Using the Stokes' theorem, the above equation can be rewritten as:

$$\frac{d\Phi_m}{dt} = \int_S \frac{\partial B}{\partial t} \cdot dA - \int_S \nabla \times (\boldsymbol{v} \times B) \cdot dA$$

$$= \int_S \left(\frac{\partial B}{\partial t} - \nabla \times (\boldsymbol{v} \times B) \right) \cdot dA \tag{1.9}$$

According to the ideal MHD description of plasma, the Ohm's law is given by:

$$\mathbf{E} + \boldsymbol{v} \times \mathbf{B} = 0. \tag{1.10}$$

The Faraday's law is written as:

$$\boldsymbol{\nabla} \times \mathbf{E} = -\frac{\partial \mathbf{B}}{\partial t}, \tag{1.11}$$

Taking the curl of Ohm's law and combining with Faraday's law results in the well known induction equation of magnetic field:

$$\frac{\partial \mathbf{B}}{\partial t} - \boldsymbol{\nabla} \times (\boldsymbol{v} \times \mathbf{B}) = 0. \tag{1.12}$$

Combining equation (1.9) with equation (1.12), gives us:

$$\frac{\mathrm{d}\Phi_{\mathrm{m}}}{\mathrm{dt}} = \int_S \left(\frac{\partial \mathrm{B}}{\partial t} - \nabla \times (\boldsymbol{v} \times \mathrm{B})\right) \cdot d\mathrm{A} \; = 0. \tag{1.13}$$

This implies that the magnetic flux through a closed fluid element remains constant as it moves with the plasma. Therefore, the magnetic fields are said to be "frozen in" to the plasma. This implies that the field lines can't come together and touch at a single point. Thus, in ideal MHD, there is no possibility for the magnetic reconnection to happen. Hence, the breaking and reconnecting of the filed lines at some point can happen only if the "frozen in" condition is violated [13-14].

In this study we are mostly concerned with how magnetic topology can change, but equation (1.13) shows that the field line topology remains invariant. Basically, this result is a consequence of the ideal Ohm's law, however, in some situation, it is necessary to consider non-ideal effects such as resistivity and viscosity. Further details of different types of non-ideal effects will be discussed in the description of generalized Ohm's law in the next chapter. In the presence of such non-ideal effects, it is possible for the magnetic field lines to come together and reconnect, thus violating the "frozen in" condition. Although, the non-ideal effects are significant in small region around the magnetic null point, however, the effects of reconnection are global via changing the overall configuration of the field lines.

The basic process of magnetic reconnection, causing the rearrangement of the field lines configuration is illustrated in Figure 1.5. The non-ideal effects come into play in the small area, called the diffusion region (marked orange), where the pair of field lines

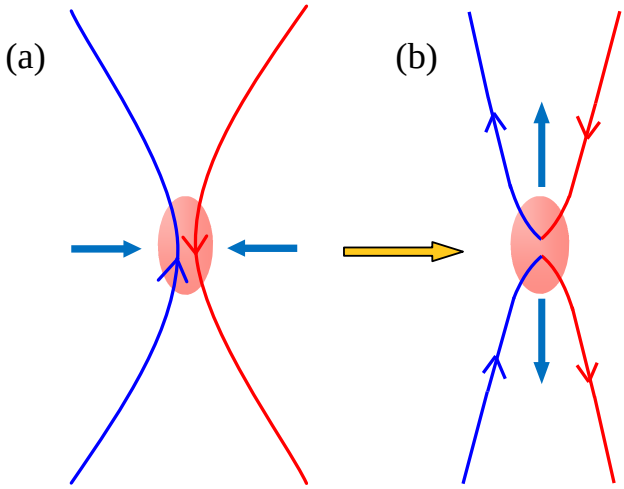

Figure 1.5: Schematic view of magnetic reconnection process. (a) Before the reconnection, two oppositely directed field lines approach each other. The non-ideal effects into play in the diffusion region (marked by pink color). (b) after reconnection the field lines are pulled away from the diffusion region. As a result magnetic energy is converted to particle energy.

approaching each other break and reconnect. As the newly reconnected field lines with higher magnetic tension, move out of the diffusion region, they release the magnetic energy into kinetic energy of the charged particles by accelerating them. Thus, reconnection can spontaneously increase the radial transport of particles and energy, which can degrade the plasma confinement in case of magnetic fusion plasmas.

To summarize the overall picture of magnetic reconnection, we can say that it is a global process which involves the topological rearrangement of the magnetic field lines, releasing magnetic energy into a large scale volume of plasma. It is noteworthy that the field lines connectivity is modified locally, due to the non-ideal effects. The fact that global properties of the plasma are strongly dependent on the local conditions makes the magnetic reconnection event even more perplexing. Answering to the question that how local changes (for example the occurrence of X-point collapse) can modify the global behavior (for example the magnetic island width or reconnection rate) of magnetic reconnection is one of the prime objectives of this research.

1.2.2. Magnetic Reconnection in Nature

In order to have an overview of the historical development of the theory of magnetic reconnection, it's essential to examine the reconnection events occurring in nature. In this section, we will cover only a few key examples of reconnection in nature. Further detailed reviews on the topic can be found in the book "Magnetic Reconnection" by Biskamp [13]; the 2009 review paper by Zweibel and Yamada ("Magnetic Reconnection in Astrophysical and Laboratory Plasmas") [22], and the 2010 review paper by Yamada *et al.* ("Magnetic Reconnection") [23].

1.2.2.1. Magnetic Reconnection in Solar Flares

Solar flares exhibit the clearest visual display of magnetic reconnection in nature and have been intensively investigated during the 20th century. Historically, they are defined as a sudden, rapid and intense variation in the brightness observed over the Sun's surface. It is now widely accepted that solar flares result from a rapid release of magnetic energy stored in solar magnetic field through the process of magnetic reconnection. As the magnetic energy being released, particles are heated and accelerated in the solar atmosphere (solar corona). The Sun's image during the solar storm on May 12, 2013, is shown in Figure 1.6. This is actually a multi-wavelength (131 angstroms and 171 angstroms) snapshot in the extreme ultraviolet (EUV) radiation zone, classified as the X-1.7 class solar flare (Solar flares are classified as A, B, C, M and X, where X-class represents the biggest and strongest solar flares). The first solar flare was reported independently by Carrington and Hodgson in 1859 [24, 25]. Since then many theories and models have been developed to understand the basic physical mechanism for such explosive events.

There are different types of eruptions observed in the solar atmosphere, such as the coronal mass ejections (CMEs), eruptive flares and prominence eruptions. The coronal mass ejections involve large scale ejections of mass and magnetic flux into the interplanetary space. During the active period of Sun, one CME is observed per day; carrying 10^{15} Wb of flux and 10^{13} Kg of plasma mass into the space [23]. Different theories have been adopted to explain the fundamental mechanisms of CMEs. However, the most standard model has been proposed by Carmichael-Sturrock-Hirayama-Kopp-

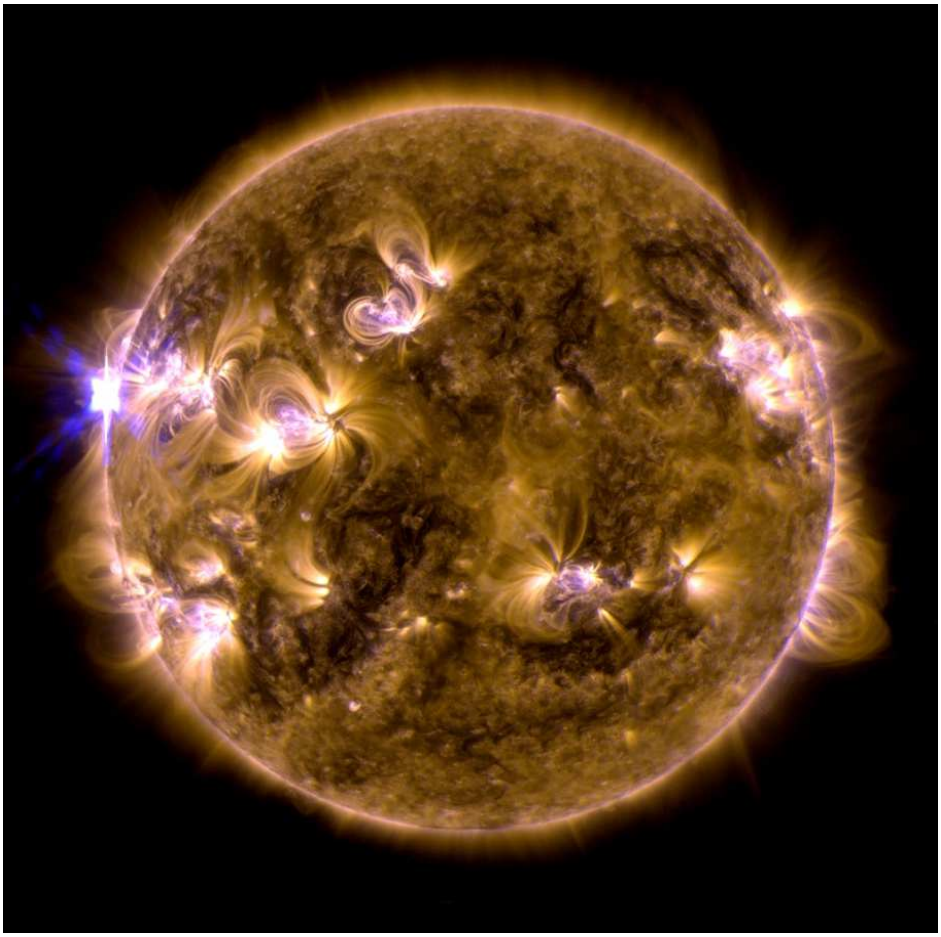

Figure 1.6: Multi-wavelength (171 and 131 Angstroms) image of the Sun's solar flare from NASA's Solar Dynamics Observatory (SDO). The Sun erupted with an X1.7-class solar flare, recorded on May 12, 2013.
Figure Credit: NASA/SDO/AIA (www.nasa.gov)

Pneuman, known as CSHKP model [26-29]. The CME shows a clear demonstration of the reconnection event, where the magnetic field lines are pulled out as the mass is ejected from the solar surface. The field lines reconnect at the X-point, directing the field lines downward and the associated plasma particles emit radiation on hitting the solar surface.

In short, solar flares exhibit many of the characteristics of the magnetic reconnection such as, fast particles, topological rearrangement of the magnetic field lines and sudden release of magnetic energy. Thus, understanding the flare physics is very useful in

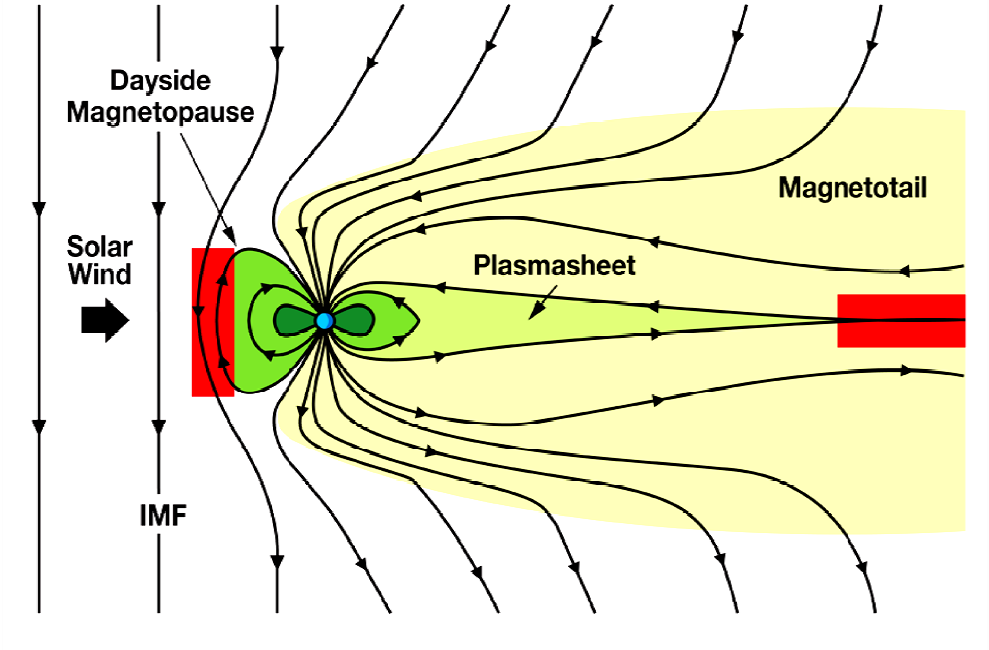

Figure 1.7: A sketch of the Earth's magnetosphere, interacting with the solar wind, coming from the left side. Magnetic reconnection takes place at the magnetopause and the magnetotail. Figure from; http://mms.gsfc.nasa.gov/science.

exploring the mysteries of magnetic reconnection. To achieve this goal, detailed observation of solar activity has been started by modern satellites such as Yohkoh (Sunbeam in Japanese), SOHO (Solar and Heliospheric Observatory), Hinode (Sunrise in Japanese) and TRACE (Transition Region and Coronal Explorer) [23]. However, many issues still remains unresolved, such as the mechanism for the onset of the explosive phase of the solar flare and population of the energetic particles during the impulsive flares.

1.2.2.2. Magnetic Reconnection in the Earth's Magnetosphere

The magnetosphere of Earth is the region of space where the Earth geomagnetic field is dominant. Its shape is determined by the geomagnetic field, the interplanetary magnetic field (IMF) and the solar wind. The interaction of solar wind leads to the compression of geomagnetic field lines on the day side, resulting in a supersonic shock wave, also known

Figure 1.8: This is an amazing picture of auroras observed across the sky near the town of Yellowknife in northern Canada. These auroras are produced due to solar winds and blasts of charged particles from the Sun during Dec 2013.
Image Credit: Courtesy of Kwon, O Chul (TWAN).

as the bow shock. Whereas on the night side, the field lines are stretched, forming a long tail, called the magnetotail. This situation is illustrated in Figure 1.7, where the solar wind from the left side, interacts with the Earth's magnetic field. The dynamic interaction between the solar wind and geomagnetic field is governed by the magnetic reconnection. The reconnection occurs both on the day side (magnetopause) and night side as originally suggested by Dungey [30]. At the magnetopause, the reconnection results in the transfer of magnetic flux and particle energy into the tail. This energy is stored in the magnetic field of the magnetotail. Reconnection also takes place at the magnetotail, where the magnetic flux and plasma is released into the inner magnetosphere. Such intermittent release of plasma and flux, results in the onset of geomagnetic substorms. It is believed that during the substorms, energy is released into the magnetosphere which is then emitted from it

though the magnetic reconnection. The geomagnetic substorms lead to the formation of the spectacular aurorae in the high latitude of the sky as shown in Figure 1.8.

The first concrete morphological study of aurora was done by Loomis in 1860 [31]. Since then a lot of research efforts have been done in this area. The modern morphology of auroral substorm was described by Akasofu in 1964 [32]. It is now believed that, the auroral substrom consists of three phases, the growth, expansion and recovery phase. The sudden brightening of the equatorward arc at the midnight is considered as the signature of the aurora onset. Although many aspects of the auroral substrom have been intensively investigated, still there are several open questions for example the ten questions asked by Akasofu [33].

1.2.2.3. Sawtooth Reconnection in Tokamaks

Sawtooth oscillations are a typical example of a global magnetic reconnection in fusion plasmas. They were discovered by Goeler *et al.* in 1974 [34] during the tokamak discharges. The sawtooth oscillation can be characterized as a periodic repetition of the peaking and flattening of the electron temperature profile [16, 17]. The name sawtooth comes from the fact that usually they are measured through soft x-ray diagnostics in plasmas and the observed X-ray have the shape of sawtooth as depicted in Figure 1.9. In general, the complete cycle of sawtooth oscillations can be divided into three phases: the ramp phase, during which the plasma density and temperature rises almost linearly in time; the second phase is called the precursor oscillation phase, which consists of sinusoidal oscillation imposed on the sawtooth structure; finally, the collapse phase, during this phase the plasma temperature and density abruptly decreases. The collapse occurs much faster (~100μs) than the ramp phase (~100ms), as illustrated in Figure 1.9 (a). The two dimensional electron temperature profiles during the above mentioned three phases of the sawtooth cycle are shown in Figure 1.9 (b).

In 1975, Kadomtsev [16] suggested an excellent explanation for the sawtooth oscillation. According to his theory, the first phase of the sawtooth oscillation (ramp-up phase) is continued until the value of safety factor $q = rB_T/R_0B_P$ becomes less than unity. Note that here B_T and B_P are the toroidal and poloidal magnetic fields; r and R_0 are the minor and major radii, respectively. Actually at the plasma center, the temperature

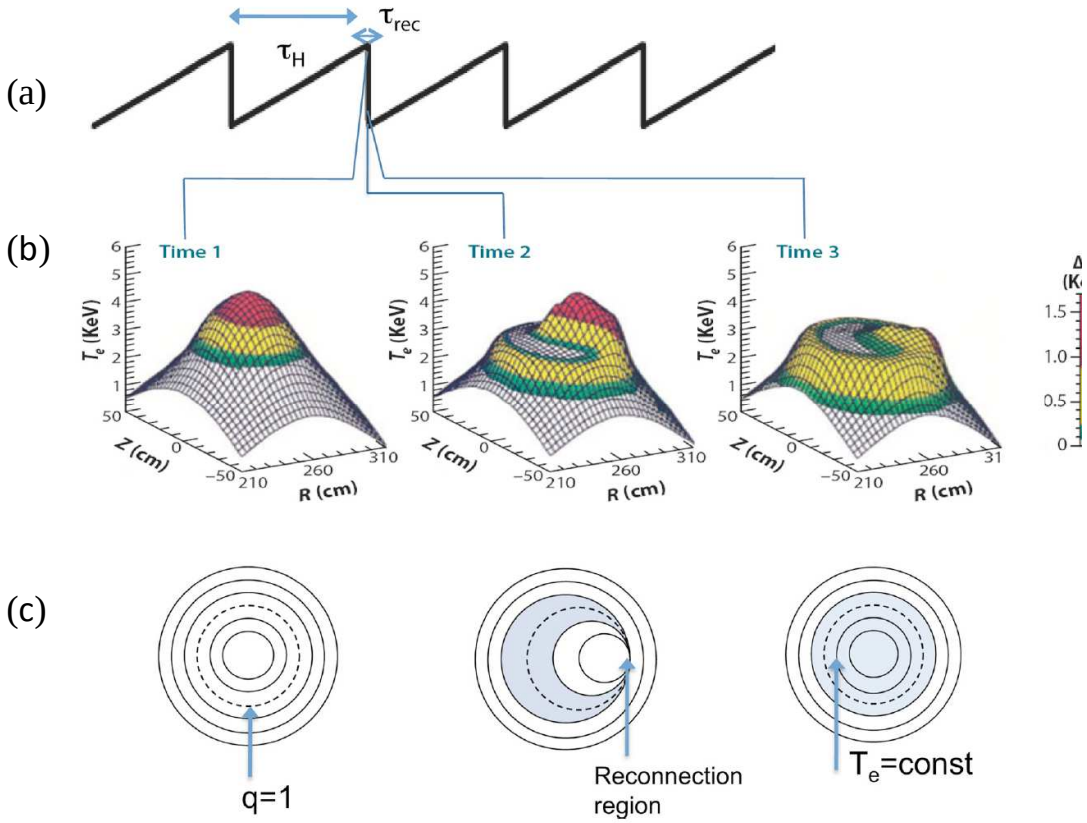

Fig. 1.9: Sawtooth oscillation measured in fusion plasma. (a) A longer build-up phase is followed by a short crash phase (b) The 2D electron temperature profile during the crash. (c) Magnetic reconnection during the sawtooth oscillation at the resonant surface of q = 1. Figure is taken from Yamada, 2011 [35].

increases due to ohmic heating, causing the resistivity to fall. For the resistivity to decrease, the current has to increase, so that the external electric field is maintained constant. Consequently, the poloidal magnetic field increases, which causes the safety factor value to drop below unity. This instigates an internal MHD kink mode in the plasma, which drives the magnetic reconnection at $q = 1$ resonant surface. This leads to flattening of the temperature profile at the plasma center, since the q value is now raised above unity. The reconnection process continues until q exceeds above unity everywhere. This process is repeated again and again because of the continuous ohmic heating. Although this explanation was initially widely accepted however, later the experimental results showed

disagreement with the theory. First of all, the Kadomtsev predicted collapse time, based on the Sweet Parker model [36, 37], is much longer than that observed in the tokamak experiments [18, 38]. This signifies the importance of the speed up reconnection in case of sawtooth oscillations, for which the mechanism is yet unknown. Secondly, the experimental measurement of the safety factor shows that its value remains below unity after the crash, which means the reconnection is incomplete. Finally, the transition from slow build up phase to the fast collapse phase can't be justified by the classical tearing mode theory. Sawtooth oscillations are a good example of the fast reconnection event, where the reconnection evolves slowly for a long time and then suddenly collapses in a very short period of time due to fast reconnection. Understanding the physical trigger mechanism for such a fast reconnection is a hot issue in the present plasma research. In this thesis, we will explore the trigger mechanism for a similar kind of fast reconnection event in 2D plasmas.

1.2.3. Magnetic Reconnection Models

1.2.3.1. Current Sheet Formation

Neutral points are defined as the locations of space where the magnetic field is zero and also called the null points. Such points results due to the simultaneous coexistence of several sources of magnetic fields. On the other hand, the current sheets appear in a conducting medium like plasma and are defined as a boundary between two plasmas, where the magnetic field is tangential on either side of the boundary and involves a change in the magnetic field direction. The current sheets can be generated in a number of ways, such as follows; (I) the region near the X-type neutral point can collapse, leading to the current sheet. (II) A current sheet is formed when two magnetic fields with different field lines topologies are pushed together. (III) Current sheet occurs when there is no magnetic equilibrium or become unstable either due to ideal or resistive MHD equilibrium instabilities [13-14].

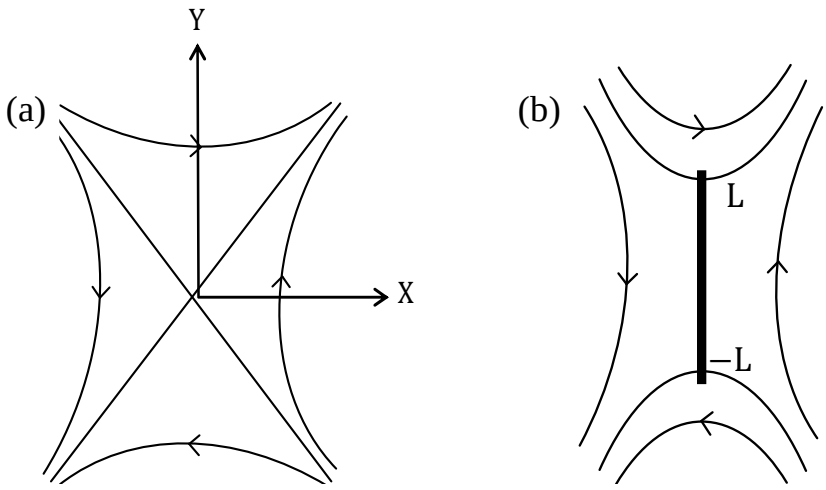

Figure 1.10: The field line topolody (a) with an X-point at the center and, (b) narrow current sheet, replacing the X-point geometry.

The current sheet formed due to the collapse of X-point involves a complex analytical theory. Let consider a 2D field line topology with an X-point as shown in Figure 1.10(a), where the magnetic field is expressed as $z = B_y + iB_x$. If the equilibrium is disturbed, the field line will move to a new configuration with a magnetic field $B_y + iB_x = (z^2 + L^2)^{1/2}$, where the current sheet exist between $z = -iL$ to $z = iL$ as shown in Figure 1.10 (b), suggested by Green 1965 [39]. In 1976, Syrovatskii and Somov [40] presented a more general solution for the X-point collapse, $B_y + iB_x = (z^2 + a^2)/(z^2 + L^2)^{1/2}$. The conditions for the X-point collapse will be rigorously investigated in our nonlinear numerical analyses, because of its global impact on the plasma dynamics. Some of the major properties of the current sheet are [13-14]:

- In the absence of flow, a current sheet of width l will diffuse at a speed η/l. The magnetic field is annihilated and the magnetic energy is converted into heat energy.
- The magnetic field is effectively frozen to the plasma outside the current sheet. The plasma and magnetic flux can be brought towards the current sheet at speed v_i. The current will expand if $v_i < \eta/l$ and the sheet becomes thinner, if $v_i > \eta/l$. For the condition $v_i = \eta/l$, a steady state is maintained.

- At the centre of the sheet, the higher pressure causes the plasma particles to be ejected from the current sheet at the Alfvén speed, depending on the external magnetic field. Magnetic flux is ejected along the plasma, and hence one of the effects is to reconnect the field. In 2D, the centre of the sheet refers to the X-point.

The free energy associated with these current sheets can lead to the magnetic reconnection. Such a reconnection process evolves either in a slow steady manner or impulsively. Though a general consensus on reconnection classification is not possible; however, the following reconnection categorization is quite common in practice.

- Steady State vs. Impulsive:

In steady state reconnection, the magnetic energy is released at almost constant rate. The magnetic reconnection on the dayside magnetopause as explained by Dungey [30] is an example of steady release of solar energy into the magnetosphere. On the contrary, in impulsive magnetic reconnection the long and slow build up phase is followed by an abrupt growth of reconnection. The tearing mode and the sawtooth crashes in tokamaks are the examples of the impulsive reconnection in fusion plasmas. The solar flares and CMEs are the examples of this kind of reconnection in astrophysical plasmas. Actually, the impulsive tearing mode reconnection, with emphasis on its trigger mechanism, will be rigorously investigated in this thesis.

- 2-D vs. 3-D Reconnection:

Most of the previous analytical and numerical reconnection analyses have been limited to the simplified 2-D plasma geometries. At present, one of the big questions in reconnection studies is how to convert the existing 2-D models into 3-D. Also, it is believed that 3-D reconnection may be different than the 2-D reconnection [41]. For example, the secondary islands formed during the tearing mode reconnection becomes flux ropes in 3-D, which interact with each other in ways impossible in 2-D. In addition to the formation of the flux ropes (magnetic island), there are many other 3D processes, which can potentially modify the behavior of magnetic reconnection e.g. streaming instability, low-hybrid drift instability and kinetic instabilities [42-45]. The 3-D analysis of magnetic reconnection is considered important for understanding the complex geometries such as

solar flares. However, the importance of 2-D reconnection cannot be reputed since it plays the pivoting role in improving our insight of the basic reconnection processes.

1.2.3.2. Sweet Parker Model

The simplest and oldest model of the steady state magnetic reconnection was proposed by Sweet [36] and Parker [37] to explain the solar flare process. They introduced the concept of current sheet of much smaller width δ than the system size L. The model assumes the steady state condition and a simplified geometry as depicted in Figure 1.11, where the plasma is ejected out of the sheet due to the excess of the magnetic pressure. Here $v_{in}(x)$ and $v_{out}(y)$ denote the mean inflow and outflow. In the same fashion, the magnetic field is expressed as $B_{\perp} = (B_{in}(x), B_{out}(y))$. The conservation of mass implies that the plasma mass entering the sheet must be equal to that ejected, which can be written as follows:

$$\frac{v_{in}}{\delta} = \frac{v_{out}}{L_{CS}}, \tag{1.14}$$

where, δ and L_{CS} are the current sheet width and length respectively. From the induction equation (1.12), we obtain:

$$\frac{v_{in}B_{in}}{\delta} \approx \frac{v_{out}B_{in}}{\delta^2}, \tag{1.15}$$

This gives, $v_{in} \approx \eta/\delta$, which means the plasma is carrying as much magnetic field as being diffused. Combining this relation with (1.14), we get:

$$\delta = \left(\frac{\eta L_{CS}}{v_{out}}\right)^{1/2}. \tag{1.16}$$

The Lorentz force accelerates the plasma along the current sheet to the outflow velocity v_{out}. It's reasonable to assume $v_{in} \ll v_{out}$, since the flows are zero at the X-point and the outflow is of the order of Alfvénic speed. Thus inertia can be neglected in x-component of the momentum equation. Hence, from $\partial(p + B_{in}^2/2\mu_0) = 0$, we get:

$$\frac{B_{in}^2}{2\mu_0} = P_m - P_{in}, \tag{1.17}$$

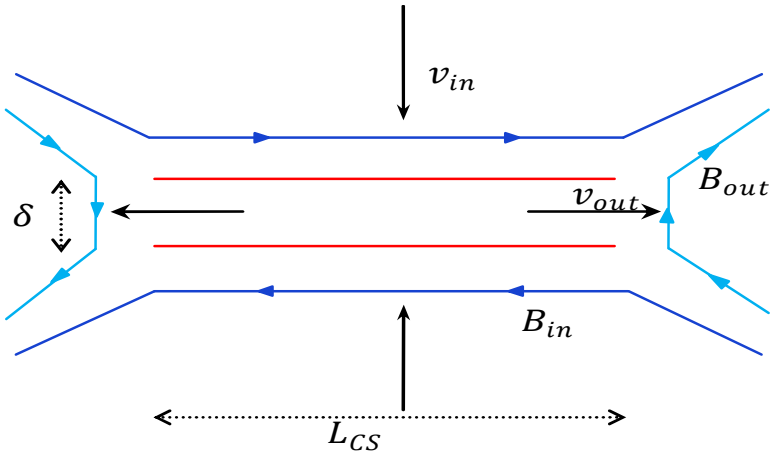

Figure 1.11: The magnetic field geometry in the Sweet Parker model, where opposite magnetic field lines reconnect in the narrow (red) diffusion region.

where, P_m is the maximum pressure at the centre of the sheet and P_{in} is the pressure at the inflow. Consider the force balance along the midplane of the current sheet. The magnetic force vanishes, since B_x is negligible. Thus the only force present along y-axis is the pressure force, which accelerates the plasma, i.e. $\rho_0 v_y \partial v_y = -\partial_y p$; integrating this relation along the current sheet, we get:

$$v_{out}^2 = \frac{2}{\rho_0}(P_m - P_{out}). \tag{1.18}$$

Combining the last equation with (1.17), we get:

$$v_{out}^2 = \frac{2}{\rho_0}\left(\frac{B_{in}^2}{2\mu_0} + P_{in} - P_{out}\right).$$

$$\Rightarrow\ v_{out}^2 \sim v_{Ai}^2 \qquad (\because P_{in} \approx P_{out}) \tag{1.19}$$

This means that flows are accelerated to Alfvénic speeds by the pressure gradient force along the current sheets. The outflow magnetic field can also be estimated; $B_{out} = B_{in}S^{-1/2}$. The ratio of the current sheet width to length which is also known as the aspect ratio of the current sheet is obtained from equation (1.16) as follows:

$$\delta = \left(\frac{\eta L_{CS}}{v_{Ai}}\right)^{\frac{1}{2}} = \frac{L_{CS}}{\left(\frac{v_A L_{CS}}{\eta}\right)^{1/2}} \Rightarrow \frac{\delta}{L_{CS}} = A^{-1} = S^{-1/2}, \quad (1.20)$$

where, S is Lundquist number of the current sheet (not global) and A is known as the aspect ratio of the current sheet. If $B_{in}$and L are of the order of global scale, then, S is the global Lundquist number. The relation $\delta/L_{CS} = S^{-1/2}$ is very important in steady state plasma analysis and is known as the Sweet-Parker (SP) scaling of reconnection. The reconnection time of the SP model can now be expressed as $\tau_{SP} = L_{CS}/v_{in}$. Using the relations (1.15) and (1.16), we get another important result; $\tau_{SP} = \sqrt{\tau_\eta \tau_A}$, where τ_η and τ_A are the resistive and Alfvén times. Thus, the time scale of the Sweet Parker reconnection is faster than resistive but slower than Alfvénic times.

Although the Sweet Parker model explains the steady state reconnection, however, in case of fast reconnection (for example in solar flares or substorms), the reconnection is very fast and it fails to justify the higher reconnection rates. For example, in solar corona the Lundquist number can easily be of the order of $S \sim 10^{14}$, the corresponding reconnection rate is of the order of 10^{-7} (reconnection rate$\sim S^{-1/2}$). However, observations of solar flares suggest the reconnection rates in the range $0.001 - 0.1$. One of the reasons for this failure may be the Spitzer resistivity used in the model, which is not quite realistic in solar systems. The introduction of anomalous resistivity might improve the validity of SP model. In short, the Sweet Parker model is a quite simple reconnection model, which can describe the slowly evolving reconnection phenomenon and gives a good general understanding of the fundamental reconnection process.

1.2.3.3. Petscheck Model

In 1964, Petscheck [46] introduced another reconnection model to justify the fast release of energy. The model is known as Petscheck model and is illustrated in Figure 1.12. The discrepancy of the SP model seemed to be resolved in this model by allowing the faster reconnection. The central idea of the Petscheck model is the introduction of slow mode shocks into the outflow regions as depicted in Figure 1.12. The double Y-shaped diffusion region is replaced by an X-shaped region, prompting the faster reconnection. Petscheck

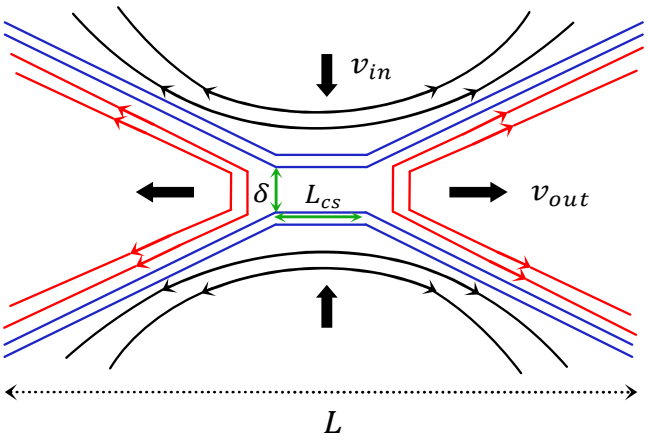

Figure 1.12:Magentic field geometry for Petschek's model. The diffusion layer is very short compared to that of SP model.

assumed that the resistivity is important in a narrow region around the magnetic null. Thus, the new diffusion region is much smaller than the global scale length, i.e. $L_{CS} \ll L$.

According to the Petscheck model, the maximum achievable reconnection rate is of the order of $(lnS)^{-1}$, that shows a very week dependence on resistivity. However, simulation studies invalidated the Petscheck model of reconnection [13]. The smallness of the diffusion in the Petschek's model suggests that it may stimulate the non-MHD effects in such small diffusion region. It has been shown that when the classical resistivity is replaced by the anomalous resistivity, it leads to the Petscheck's like X-point reconnection. However, the source for triggering such anomalous resistivity is not clearly understood.

From analytical point of view, the critical deficiency of this model is the inappropriate treatment of the diffusion region. A correct theory requires the boundary layer solution by matching the inner resistive solutions to the external ideal solutions. Therefore, in limit of small resistivity or high Lundquist number, Petscheck's model is not a self-consistent reconnection model.

1.3. Background and Motivation

1.3.1. The Trigger Problem

In laboratory, space and astrophysical plasmas there are numerous examples of magnetic reconnection phenomena where the magnetic configuration evolves slowly for a long period of time and followed by a sudden change in a very short time. This is often referred to as the trigger-problem. The reconnection processes involved are categorized as bursty or explosive. In such scenarios, the steady state models of Sweet Parker and Petscheck can't justify the abrupt growths of reconnection rates. Solar flares, CMEs, substorms and sawtooth activity are the typical examples of explosive reconnection. Tearing mode reconnection is another well known example of bursty magnetic reconnection in fusion and astrophysical plasmas.

In order to have an explosive growth of the reconnection, there must be a trigger which abruptly starts the faster reconnection and also there must be a free energy source to maintain the faster reconnection. This poses some challenging questions for the theoretical modeling. For example, what restricts the reconnection process to evolve slowly without triggering the onset of faster reconnection? What is the trigger mechanism of the fast reconnection? This thesis study is mainly devoted to answer these challenging questions and also identify the critical conditions necessary for the onset of the fast reconnection. In this section we briefly review the previous results related to the trigger problem of the nonlinear resistive tearing mode.

1.3.2. Explosive Growths in Double Tearing Mode (DTM)

Explosive nonlinear growth of the magnetic flux and plasma flow perturbations occurs more conspicuously for the resistive double tearing mode (DTM). In cylindrical plasmas, Ishii *et al.*, [47] reported that instead of nonlinear saturation in the intermediate regime, the DTM can evolve explosively with much weaker dependence on resistivity. Further, Ishii *et al.* [48] proposed that the triangularity of magnetic islands and the strong current point formation are responsible for the explosive growths of the DTM. The contour plots of the magnetic flux, showing the current point formation during the nonlinear DTM evolution,

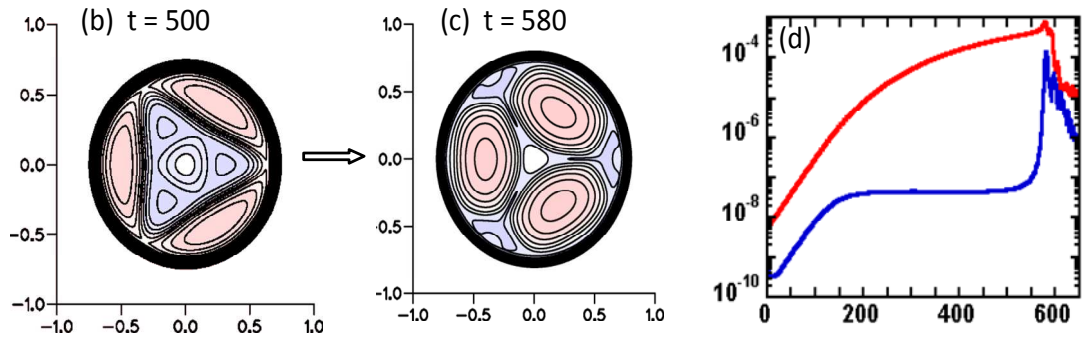

Figure 1.13: Example of Double Tearing Mode in poloidal plane of 3D-plasma. Figure is adapted from ishii *et al*, 2000 [47].

are depicted in Figure 1.13. In another attempt, the intrinsic localized shear flows in slab geometry due to magnetic island deformation were suggested to be the reason of the fast reconnection event [49]. Moreover, a secondary structure-driven instability due to the triangular deformation of the magnetic islands in slab configuration was also proposed to explain the explosive nonlinear growth of the magnetic islands [50, 51]. In the last mentioned analysis of the explosive DTM, the 1-D initial equilibrium is modified quasilinearly into 2-D structure by the slowly growing magnetic island in the Rutherford regime, probably leading to a secondary instability with the same DTM parity. Such a nonlinear feedback of the secondary instability with an exponential of exponential growth was considered to trigger the explosive reconnection in case of DTM [50, 51]. Figure 1.14 shows the triangularity of the magnetic island during the nonlinear evolution of DTM.

1.3.3. Impulsive Reconnection in Nonlinear Resistive Tearing Mode

1.3.3.1. Brief History of the Resistive Tearing Mode Instability

Tearing mode instability is one of the main mechanisms behind the magnetic reconnection both at small scales such as tokamak and at large scales such as space plasmas. The tearing mode instability was first analyzed by Furth, Killeen and Rosenbluth (FKR), using 2D reduced-MHD (RMHD) in slab geometry [52]. They established the linear tearing mode theory and defined the instability criterion $\Delta' > 0$. Rutherford [53] developed a theory of

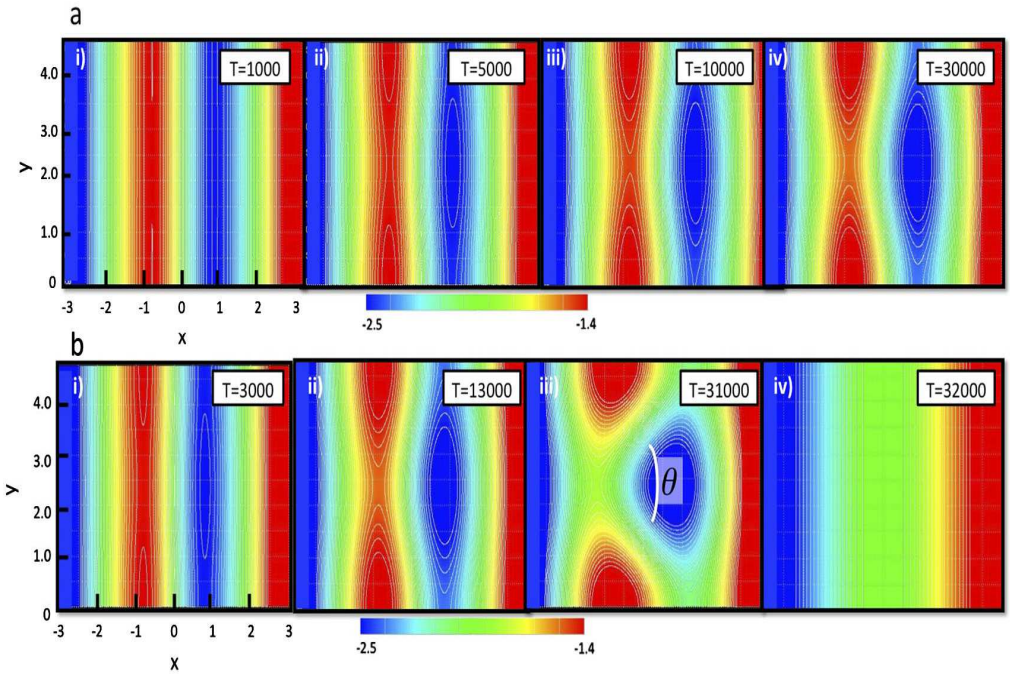

Figure 1.14: Flux contours at different times during the nonlinear evolution for the cases of (a) $L_y = 0.75$ and, (b) $L_y = 0.76$, where strong triangularization is observed. Figure is taken from Miho *et al.*, 2011 [51].

the nonlinear evolution and showed that the exponential growth of the mode in the linear stage is replaced by a slowly evolving phase where the island width grows according to the simple equation $dw/dt = 1.22\eta\Delta'$. White *et al.* [54] developed the saturation theory of the magnetic island by extending the Rutherford theory. In both of these nonlinear theories, the constant-ψ approximation is the basic assumption, which is valid only for very thin islands ($\Delta' w \ll 1$). Militello and Porcelli [55] claimed more exact expression for the saturation island width for the symmetric case and their results does not rely on the quasi-linear approximation. According to [55, 56], in the limit of thin island and low Δ', the saturation island width (w_s) is given by $w_s = 2.44 b^2 \Delta'$, where b is the characteristic current gradient length $b = \sqrt{-J_0(0)/J_0''(0)}$ and this formula of the saturation island width is also known as POEM formula (named after the four authors).

The earliest numerical studies of the tearing mode include the work by Biskamp and Welter [57], White *et al.* [58] and, Steinolfson and Van Hoven [59]. All these authors

obtained a general agreement with FKR and Rutherford theory. A rather rigorous review of numerical verification of the Rutherford nonlinear slow growth and nonlinear saturation of the magnetic island has been reported by Biskamp in his book ("Nonlinear Magnetohydrodynamics") [60].

1.3.3.2. Scaling of the Magnetic Island in the Limit of Large Δ'

In general, the theoretical study of tearing mode has been restricted to low Δ'. However, kinetic effects can increase the instability criterion to $\Delta' > \Delta'_c$ [61], highlighting the relevance of large Δ' tearing modes. Another argument in favor of the physical relevance of large but finite Δ' tearing mode is that during the nonlinear evolution of tearing mode, narrow current sheets can form which can be unstable to tearing modes. Thus, the stabilizing influence of flows along the current sheet may change the instability criterion $\Delta' > 0$ [62]. In the limit of large Δ', the constant-ψ approximation is no more valid and the Rutherford theory breaks down. Waelbroeck [63] predicted that for large Δ', the magnetic island undergoes an X-point collapse instead of saturation, leading to a current sheet formation. The X-point collapse happens when the island width is larger than a critical value, namely, $w > w_c \approx 25/\Delta'$. Actually, the X-point collapse triggers the onset of the abrupt reconnection phase and that's why it has been the focus of several reconnection studies. The theoretical predictions of Waelbroeck [63, 64] were numerically testified by Jemella *et al.*, [65, 66]. Through numerical simulations in slab geometry, they analyzed the magnetic island width dependence on the instability parameter Δ'. For small Δ', the results were in agreement with the Rutherford nonlinear theory, however, for large values of Δ' the current sheets were observed that triggered the faster growth of magnetic island. Furthermore, it was found that the dominance of the Sweet-Parker reconnection in resistive MHD simulation is due to the singular nature of the underlying ideal reconnected state [65, 66], which is consistent with the equilibrium theory of Waelbroeck [63, 64].

Louriero *et al.* [67] formulated the transition criteria from the algebraic slow growth phase to the faster Sweet Parker phase, in terms of the critical island width w_c with a scaling $\Delta' w_c \approx 8.2 + f(\Delta')\eta$. They found that after island width exceeds the critical width, the X-point collapse occurs and the current sheet is developed which is unstable to plasmoid instability, followed by island coellease and finally saturation. The narrow

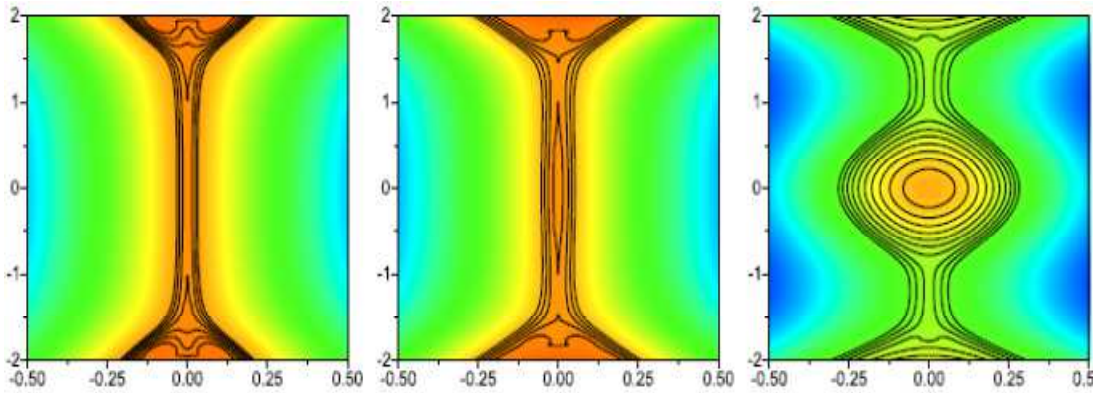

Figure 1.15: Flux contours of magnetic flux, showing the current sheet instability, resulting in secondary island formation. Figure is taken from Loureiro *et al.*,2005 [67].

current sheet after the X-point collapse and secondary island (plasmoid) formation are depicted in Figure 1.15. However, in such studies the effect of viscosity or external flows were not considered, which can significantly modify the critical condition of X-point collapse and the reconnection rate in the abrupt nonlinear growth phase.

1.3.3.3. Effects of Viscosity on the Abrupt Growth Dynamics of Tearing Mode

The critical island width for the X-point collapse is a signature for the onset of the abrupt reconnection stage, which has been shown to depend on the resistivity and the instability parameter Δ' [67]. How the viscosity can affect the critical island width, is still an open question. Generally, the viscosity plays a dissipation role in the MHD fluctuations while the resistivity determines the singular layer dynamics of the tearing mode. It is not always weak as compared to the resistivity in laboratory and astrophysical plasmas because micro-scale turbulence can enhance the viscosity [68-70]. The turbulent viscosity is usually larger than the collisional value and is given by $\mu_{turb} = 10T^{3/2}/B^2\ [m^2 s^{-1}]$, where T is the temperature in keV and B is the magnetic field in Tesla [71]. However, the collisional resistivity is given by the well-known Spitzer resistivity [72], $\eta = 0.05T^{-3/2}[m^2 s^{-1}]$, by assuming weak dependence on turbulence. Hence, the magnetic Prandtl number $P_r = \mu/\eta$ is of the order of $P_r = 200T^3/B^2$, which shows a strong dependence of temperature. For typical magnetic fusion plasma with $B = 1Tesla$ and $T = 1keV$, P_r is of the order of 200.

Porcelli [73] emphasized the role of the viscosity by performing a comprehensive linear analysis of tearing mode. It has been shown that in the limit of low Δ', the usual tearing scaling of the growth rate $\gamma \sim \eta^{3/5}$ gets modified in the case of finite viscosity and scales as $\gamma \sim \eta^{2/3} P_r{}^{-1/6}$, which was termed as the visco-tearing mode. In the limit of $\Delta' \rightarrow \infty$, the growth rate scales as $\gamma \sim \eta^{1/3} P_r{}^{-1/3}$ and is known as the visco-resistive kink mode. These scalings were numerically confirmed in different regimes [71]. Grasso *et al.* [74] showed that for moderate values of η and $P_r \sim O(1)$, there exists a critical Δ'_c for the linear tearing mode. Militello *et al.* [75] developed the visco-asymmetric tearing mode, which signifies that the critical stability threshold is pushed to much higher value for asymmetric equilibrium in visco-resistive regime. Furthermore, viscous effects are very essential in tearing mode with shear flows [76, 77]. Therefore, viscosity may significantly affect the evolution of resistive tearing mode instability.

In the limit of high Lundquist number S, it is found that the Sweet parker current sheet is replaced with multiple islands (plasmoids) along the current sheet and the corresponding instability is called the plasmoid instability [78-85]. The plasmoid instability leads to higher reconnection rates than the SP rates. Therefore, it's important to briefly introduce the underlying mechanism of the plasmoid instability in the resistive tearing mode.

1.3.3.4. The Plasmoid Instability

Recently, there has been a renewal of interest in the reconnection of Sweet-Parker current sheet in the limit of high Lundquist number $S \geq 10^4$, where a much faster reconnection has been reported [78-85]. The continuous formation and ejection of the plasmoids observed in these studies, has been identified as the key mechanism responsible for the faster growth of the reconnection rates. This means that the SP scaling of the reconnection rate $S^{-1/2}$, is no longer valid at high Lundquist numbers and the reconnection progresses at much higher rate, almost independent of the plasma resistivity. The linear theory of plasmoid instability was proposed by Loureiro *et al.* [84], predicting the maximum growth rate scaling of $S^{1/4}$ and the number of plasmoids as $S^{3/8}$, with a current sheet width scaling as $S^{1/8}$. This theory was later extended with a more generalized case, including the viscosity effects [85].

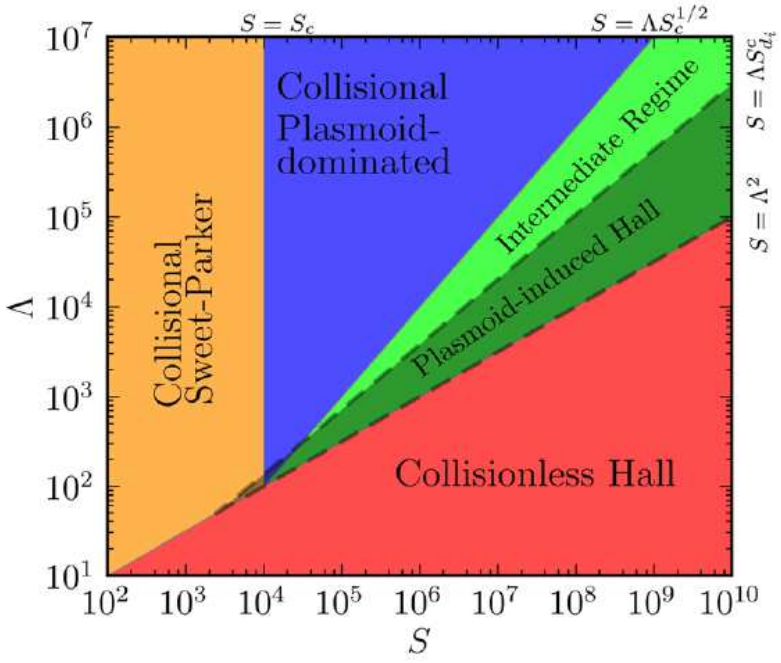

Figure 1.16: Phase diagram of magnetic reconnection showing five phases in the parameter space of S and $\Lambda = L/d_i$, where d_i is the ion inertial length .
Figure is taken from Huang *et al.*, 2013 [86].

Depending on the parameter regime, the plasmoid once formed in the original collisional secondary current sheet, may lead to a transition to the fast collisionless reconnection (Hall). The transition from collisional to kinetic regime occurs when the current sheet width approach the ion kinetic scale, i.e. $\delta_{SP} \leq d_i$, where d_i is the ion inertial length [87]. On the other hand, if the plasma remains in the collisional regime, then long chain of plasmoids form along the narrow current sheet. In a recent study [86], the phase diagram of the various possible reconnection phases has been reported in parameter space and is shown in Figure 1.16. The phase diagram depicts the five distinct phases of reconnection, namely, the collisional Sweet-Parker, collisional plasmoid dominated, collisionless Hall, plasmoid induced Hall and intermediate regime. Despite all this progress, there are still some unresolved issues even in the limit of moderate S. For example, what triggers the onset of X-point collapse and the formation of narrow current

sheet? What are the effects of viscosity on such abrupt nonlinear processes? How the small scale turbulence might affect the reconnection rates? These questions provide us the main inspiration for carrying out this study.

Magnetic reconnection usually occurs in turbulent environment, which can modify the reconnection behavior through direct nonlinear interaction with the magnetic island. The turbulence can be a driven turbulence or spontaneous. Since the turbulence is known to influence many processes, then it is natural to ask the question to what extent the background turbulence can affect the magnetic reconnection process. Therefore, it is essential to discuss the recent progress regarding the turbulent magnetic reconnection.

1.3.4. Turbulent Reconnection

For weakly collisional plasmas, the Lundquist number S is usually very large, (e.g. $S{\sim}10^{12}{-}10^{14}$ in the solar corona and $S{\sim}10^{8}$ in tokamaks). The observed reconnection rates in these environments are much faster than those predicted by the classical SP model. Thus, the prime challenge of the present-day reconnection research is to identify the key physical mechanism that can justify the observed fast reconnection rates. From several theoretical and numerical studies, it is now evident that non-classical effects such as the Hall MHD involving two fluid effects in laminar flows [87-93] and anomalous resistivity due to micro-turbulence [94-98], result in Petscheck-like [46] fast collisionless reconnection. However, the Petschek's mechanism fails in limits of resistive MHD [99-102]. For the fast collisionless reconnection to take place, the resistive width of the reconnection layer is small compared to the relevant kinetic scale. However, in most of the situations, this condition is not satisfied. This means that neither the Sweet-Parker nor the Petschek models present a universally acceptable reconnection mechanism. Small scale turbulence is one of the possible candidates to trigger the fast reconnection rates and hence fill the gap between the theory and observations.

Significant progress has already been made regarding the theory and simulations of turbulent reconnection [103-111]. The pioneering numerical study of magnetic reconnection in the presence of turbulence was performed by Matthaeus & Lamkin [103]. Lazarian and Vishniac [104] proposed the first analytical model of turbulent reconnection,

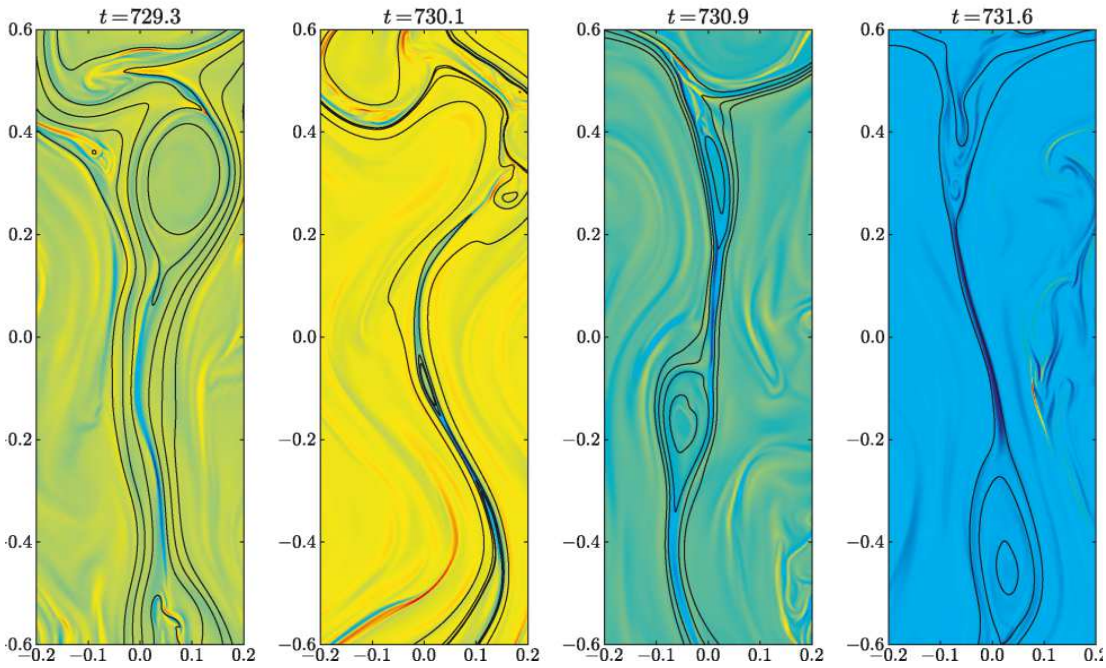

Figure 1.17: Contour plots of the current density at different times of the turbulent reconnection phase. Figure is taken from Loureiro *et al.*, 2009 [107].

suggesting that turbulence can significantly enhance the reconnection rate by exciting multiple reconnection sites along the current sheet. In 2D simulations, the enhancement of reconnection rates in the presence of background turbulence was numerically confirmed by Loureiro *et al.* in (2009) [107]. The contour plots of current density in presence of turbulence obtained by them are shown in Figure. 1.17. Actually, in presence of turbulence the plasmoid instability can occur even at higher values of resistivity $\eta \sim 10^{-3}$, compared to the critical resistivity $\eta \leq 10^{-4}$ in the case of without turbulence [78-85]. This implies that turbulence may act as a trigger for the onset of impulsive fast reconnection.

Instead of applying the external turbulence forcing in the form of random noise, it may be interesting to consider a finite frequency dynamic turbulent flow, similar to ion temperature gradient (ITG) driven small scale turbulence, in the tearing mode reconnection [112]. Actually, the coexistence of MHD activities including the tearing mode and ion temperature gradient (ITG) driven drift wave have been reported to occur commonly in magnetic fusion plasmas [113-115]. The nonlinear interaction mechanism

and the exchange of kinetic and magnetic energies in such a mixed MHD and micro-scale turbulence lead to very complex nonlinear dynamics. One of the main objectives of this study is to investigate the effects of background turbulent dynamic flow on the magnetic reconnection behavior of resistive tearing mode. For this purpose, we suggest a dynamic flow with finite frequency and wave number k_y which may modify the reconnection properties most probably through direct nonlinear interactions with the magnetic island. Further details will be discussed in the later part of this thesis.

1.4. Dissertation Objectives

This thesis is devoted to the study of the resistive tearing mode in the framework of two dimensional, resistive RMHD. The key objectives are:

1. To explore the basic mechanism responsible for the onset the X-point collapse, leading to the abrupt nonlinear growth dynamics of the resistive tearing mode.
2. To investigate the effects of viscosity on the trigger mechanism of such abrupt nonlinear processes.
3. To estimate the effects of the self-generated zonal field and zonal current on the nonlinear bursty reconnection.
4. To determine how a background dynamic turbulent flow will affect the reconnection behavior?
5. To analyze the dependence of impulsive bursty reconnection on the dynamic flow properties, such as radial-parity, amplitude and frequency.

1.5. Summary and Outline

This dissertation provides a detailed study of the nonlinear behavior of the resistive tearing mode, particularly in strongly driven regime, identified by $\Delta' W \sim 1$. Actually, the nonlinear dynamics of the resistive tearing mode is significantly modified for large values of the instability parameter Δ', where the usual X-point geometry collapses to a narrow current sheet. The critical island width for the X-point collapse is a signature for the onset of abrupt reconnection stage. The trigger mechanism of the X-point collapse as well as the dependence of the critical conditions for the collapse on the plasma properties, are still poorly understood issues.

The self-generated zonal currents during the nonlinear evolution of the tearing mode modify the equilibrium current profile, where the local current peaking is speculated to be responsible for the onset of the abrupt growth phase. In order to testify such an idea, a secondary instability analysis is proposed in this study, in which the zonal current quasilinearly modifies the equilibrium current profile. Note that here the eigen mode characteristics of the secondary instability are the same as those of the primary tearing mode due to the same type of drive force (current gradient). Such coincidence of the fluctuations can directly enhance the nonlinear tearing mode to trigger the X-point collapse and then give rise to a current sheet formation through positive feedback of the zonal current. This kind of secondary instability may be considered as a special case of general ones, which are usually different from the primary one. The local current peaking effect due to the zonal current provides a positive feedback to increase the tearing mode fluctuations, signifying a probable mechanism for the onset of X-point collapse and explosive nonlinear growth. Furthermore, a systematic study of the viscosity effects on the nonlinear dynamics of the tearing mode is performed with a focus on the P_r dependence of the critical island width $\Delta' w_c$ for the X-point collapse and the abrupt growth of the reconnected flux in the SP regime. It is found that the presence of finite viscosity modifies the scaling of critical island width. A prominent transition is observed at $P_r = 1$ for the onset of the X-point collapse. The growth rate of the reconnected flux in the speed-up stage remains unaffected until $P_r > 1$ after which it decreases with viscosity, in accordance with the existing theory.

In the above mentioned analyses, we assumed laminar reconnection; however, magnetic reconnection usually occurs in turbulent environment, which can probably modify the tearing mode reconnection through direct nonlinear interaction with the magnetic island. How the background small scale turbulence affects the reconnection behavior in resistive tearing mode is one of the key objectives of this study. An independently evolving dynamic turbulent flow is coupled with the RMHD equations through Poisson brackets. A two phase reconnection is observed by including the dynamic flow. A relatively slowly evolving SP current sheet is generated in the first phase and plasmoid instability is triggered in the second phase, where multiple plasmoids are continuously generated and ejected along the current sheet, leading to bursty impulsive reconnection. The onset and evolution of the plasmoid instability are strongly modified by the frequency and radial parity of the flow. In particular, the scaling of reconnection rates is found to be independent of resistivity, confirming that plasmoid dominated reconnection is truly fast reconnection.

This dissertation consists of six main chapters and three appendixes, which are outlined as follows:

Chapter 1: The basics of nuclear fusion and the magnetic confinement in fusion devices are briefly introduced. The fundamental concept of magnetic reconnection phenomenon as well as its examples in the universe is elaborated. The important steady state reconnection models are discussed in detail. An overview of the existing theories as well as simulation studies of the resistive tearing mode is presented, focusing on the trigger problem in the limit large instability parameter Δ'. The relevance of large viscosity in fusion and astrophysical plasmas, and its impact on the magnetic island evolution is explicated. The problem of plasmoid-dominated impulsive fast reconnection in the presence of preexisting turbulence is reviewed. Finally, the key objectives and summary of this dissertation are presented.

Chapter 2: Here, we derive and study the physical simulation model used in this thesis. The magnetohydrodynamics (MHD) equation system is introduced both for ideal and resistive cases. The generalized Ohm's law is then discussed briefly to notify the physical significance of each term, in particular the terms missing from the resistive MHD

description of the Ohm's law. Then, the MHD equations are reduced to the incompressible two-field resistive RMHD equations by the ordering method. Finally, the RMHD equations are normalized.

Chapter 3: This chapter presents a comprehensive linear analysis of the resistive tearing instability. The classical linear theory (i.e. Furth-Killeen-Rosenbluth (FKR) theory) of the resistive tearing mode is detailed for the constant-ψ case. The linearized RMHD equations are solved by dividing the plasma into inner and outer regimes and the solutions are compared at the boundary of the resistive layer. The validity of FKR theory is discussed for different possible situations. In particular, the linear analysis is repeated for the non-constant-ψ case. Then, the initial equilibrium profiles and the Δ' calculations are detailed. The simulation model and the numerical schemes used in this thesis are described. Finally, the simulation code is benchmarked for the typical linear growth rate scaling of the resistive tearing mode with η, Δ' and k_y.

Chapter 4: Here, we discuss the probable physical trigger mechanism responsible for the abrupt growth dynamics of the resistive tearing instability in the strongly driven regime (i.e. large Δ'). First, we introduce a typical nonlinear simulation case, where the abrupt growth dynamics of the perturbation quantities is illustrated. Second, we propose a secondary instability analysis based on the quasilinearly modification of the equilibrium current profile by the zonal perturbation current. The results suggest that the current peaking effect due to the zonal current results in a nonlinear positive feedback to enhance the tearing mode fluctuations and can be a probable mechanism for the onset of X-point collapse, leading to the explosive growth dynamics. A similar tendency is observed by including a finite viscosity. For $\mathrm{P_r} > 1$, the secondary growth rates are reduced with the viscosity, showing a transition in the tendency at $\mathrm{P_r} \approx 1$. On the other hand, effect of viscosity on the onset of the X-point collapse and the abrupt nonlinear reconnection is investigated directly through linear and nonlinear simulations. The linear growth rate dependence on viscosity is analyzed, showing a transition at $P_r = 1$. Then, a systematic investigation of the viscosity dependence of the critical island width $\Delta' w_c$ for the X-point collapse is performed. A new transition criterion is proposed for the critical island width scaling by including the viscosity dependence. The value of the critical island width in the

limit of zero resistivity is modified due to finite viscosity. Most importantly, a transition behavior is observed for the critical island width scaling with the viscosity at magnetic Prandtl number P_r =1. The reconnection rate in the abrupt growth phase is significantly reduced with the viscosity in the regime of $P_r > 1$.

Chapter 5: In this chapter, we analyze the reconnection behavior of the resistive tearing mode in the presence of preexisting dynamic flow. The independently evolving dynamic flow is coupled with the RMHD equations through the Poisson brackets. Linear stability properties of the tearing mode are found to be fairly modified with the dynamic flow, depending on the features of the dynamic flow. Specifically, the linear stabilization effect is evidently weakened by the finite frequency. The nonlinear analysis of the resistive tearing mode with dynamic flow reveals two phase reconnection. A current sheet is formed in the first phase and is followed by the plasmoid instability in the second phase, where multiple plasmoids are continuously generated and ejected. The onset time of the plasmoid-dominate impulsive reconnection is strongly modified with the flow frequency and amplitude. By including the dynamic flow, the effective reconnection rate is considerably enhanced in the regime of low resistivity as compared to the case of slower SP reconnection. Scaling of the effective reconnection rate is found to be independent of resistivity.

Chapter 6: This chapter summarizes the key problems addressed in this PhD study and reports the new findings suggested in this research. The significance of the key findings of the study in fusion plasmas is discussed. Finally, we discuss about the different possible ways to extend this research in future.

Appendix A: The normalization of the two field RMHD equations is detailed.

Appendix B: Full length calculations of the instability parameter Δ' are detailed in this appendix. The instability parameter Δ' is calculated for the two most commonly used equilibrium profiles, namely the Harris equilibrium and $1/\cosh^2(ax)$ equilibrium.

Appendix C: Finally, the scientific contributions during this PhD study are presented.

Chapter 2

The 2D Reduced MHD Model

2.1. Introduction

Controlling the MHD instabilities in the magnetic fusion devices (such as tokamaks) is the one of the prime objectives of the current fusion research. A physical model is essential to investigate the dynamics of any plasma instability. Depending on the particular plasma and the specific phenomena under consideration, various types of models are adopted to describe the fundamental physical dynamics. In this thesis, we study the abrupt nonlinear dynamics of the resistive tearing modes using the reduced MHD (RMHD) model. The model is named as RMHD because of the fact that it involves fewer fields than the full MHD equations.

In this chapter, we first derive the RMHD equations, starting from the single fluid MHD description of plasma. Finally, we describe the normalization of the equation system. In deriving the RMHD equations, we mostly follow the work of Strauss [116]. For further reading we recommend the books of Friedberg (“Ideal MHD”) [117], Hazeltine and Meiss (“Plasma Confinement”) [118] and Biskamp (“Nonlinear Magnetohydrodynamics”) [60].

2.2. The MHD Equations

The idea of magneto-hydro-dynamics or MHD is that magnetic fields can induce currents in a moving conducting fluid, which in turn exert forces on the fluid itself. Thus we can say that MHD is a model that describes the macroscopic behavior of the plasma. Actually, the plasma is composed of a very large number of ions and electrons, and to estimate the plasma properties we have to follow these individual particles, which is the basic principal of the kinetic approach. However, in MHD description the plasma is considered as a single

fluid that is controlled by electromagnetic forces and hence it is possible to describe macroscopic behavior of the plasma without having to know the position and the velocity of individual particles. The MHD model consists of Maxwell equations and the conservation equations of mass, momentum, and energy of the plasma. Under certain conditions, the fully ionized plasma can be considered as a single fluid described by the following ideal MHD equations [60, 116-118]:

Conservation of mass:

$$\frac{\partial \rho}{\partial t} + \boldsymbol{\nabla}.(\rho \mathbf{v}) = 0, \tag{2.1}$$

where ρ and $\boldsymbol{v}$ represent the mass density and velocity of the plasma, respectively.

Conservation of momentum:

$$\rho \frac{d\mathbf{v}}{dt} = \mathbf{J} \times \mathbf{B} - \boldsymbol{\nabla} p, \tag{2.2}$$

where ***J*** is the current density and ***B,*** the magnetic field, and p is the plasma pressure. Note that the symbol, $d/dt = \partial/\partial t + \mathbf{v}\,.\,\boldsymbol{\nabla}$ denote the total time derivative.

Conservation of Energy: In the adiabatic limits, the energy equation reduces to;

$$\frac{d}{dt}\left(\frac{p}{\rho^{\gamma}}\right) = 0, \tag{2.3}$$

where, γ represents the ratio of the specific heats.

Ohm's Law: In the ideal limit the Ohm's law is given as follows;

$$\mathbf{E} + \mathbf{v} \times \mathbf{B} = 0, \tag{2.4}$$

where, ***E*** is the electric field. Note that in the above equation, the displacement current is neglected because the plasma speed is much lesser than the speed of light.

Faraday's Law:

$$\boldsymbol{\nabla} \times \mathbf{E} = -\frac{\partial \mathbf{B}}{\partial t}, \tag{2.5}$$

Ampere's Law:

$$\boldsymbol{\nabla} \times \mathbf{B} = \mu_0 \mathbf{J}, \tag{2.6}$$

Finally, the divergence of the magnetic field is zero; i. e. magnetic monopoles don't exist:

$$\nabla \cdot \mathbf{B} = 0. \tag{2.7}$$

The ideal Ohm's law (equation (2.4)), is sometimes named as perfect conductivity equation and sometimes referred to as the flux freezing equation. The ideal Ohm's law implies that in the conducting plasma the electric field is zero in the reference frame moving with the plasma. The electric field can arise only from the Lorentz transformation. This means that the magnetic field is frozen in to the plasma, and hence the magnetic flux moves with plasma and remain unchanged. Thus in ideal MHD approximation, the magnetic flux can't break or reconnect; means no reconnection. The fact that magnetic flux remains conserved in ideal MHD limit is straight forward and is detailed in first chapter. On the other hand, if we consider a finite plasma resistivity, the ideal Ohm's law gets modified as follows:

$$\mathbf{E} + \mathbf{v} \times \mathbf{B} = \eta \mathbf{J} \tag{2.8}$$

where η is the plasma resistivity. This equation is simply called the Ohm's law, which allows the magnetic field diffusion and magnetic reconnection; violating the frozen-in flux condition. For example in the presence of the current sheet, strong electric field exists and hence the ideal MHD approximation is not valid any more. Under such circumstances, we need to take resistivity into account, leading to the resistive MHD description. Now, let take curl of equation (2.8), we obtain:

$$\nabla \times \mathbf{E} + \nabla \times (\mathbf{v} \times \mathbf{B}) = \eta (\nabla \times \mathbf{J}) \tag{2.9}$$

Now let combine this equation with Faraday's and Ampere's law, we get the induction equation;

$$\frac{\partial \mathbf{B}}{\partial t} = \nabla \times (\mathbf{v} \times \mathbf{B}) + \frac{\eta}{\mu_0} \nabla^2 \mathbf{B}. \tag{2.10}$$

The first term on the right hand side of the above equation represents the advection of the magnetic field while the second term is the diffusion or resistive term. The ratio of the advective and diffusive terms is called the magnetic Reynolds number defined as:

$$R = \frac{L_c v_c}{\eta}, \tag{2.11}$$

where, L_c and v_c are the characteristic scale length and characteristic velocity of the plasma flow.

2.3. Generalized Ohm's Law

In the previous section, we reported the Ohm's law both for the ideal and resistive MHD cases (equations (2.4) and (2.8) respectively). However, because of the central role of Ohm's law in magnetic reconnection, it is essential to mention the neglected terms with relevant simplification assumptions. Basically, the generalized Ohm's law is obtained from the momentum equations of electron and ion based on the two fluid MHD description of plasma. Thus, with the sole assumption of non-relativistic limit (neglecting the displacement current), the generalized Ohm's law takes the form [117,119]:

$$\mathbf{E} + \mathbf{v} \times \mathbf{B} = \eta \mathbf{J} + \frac{\mathbf{J} \times \mathbf{B}}{en} - \frac{\nabla p_e}{en} + \frac{m_e}{e} \frac{\mathrm{d}\mathbf{v_e}}{\mathrm{dt}} - \nabla . \Pi_e \qquad (2.12)$$

where p_e is the electron pressure and Π_e is the electron viscosity tensor. The significant of each term on the right hand side of equation (2.12) is explicated as follows:

- The first term on the right hand side of equation (2.12) appears due to the plasma resistivity. In case of ideal MHD this term becomes zero but is vital for the resistive MHD description.
- The second and third term on the right hand side of equation (2.12) represent the Hall MHD and electron pressure gradient respectively. These two terms can be ignored only if we assume the low frequency MHD approximation.
- The fourth term on the right hand side of equation (2.12) is due to the electron inertia, which can be neglected.
- The last term presents the electron viscosity contribution. To neglect this term we have to make the assumption that the plasma particles undergo sufficient collisions to make the distribution nearly Maxwellian; also the macroscopic lengths are assumed to be much longer than the mean free path. Under such assumptions, the high order moments can be expressed in terms of low-order moments and measured by transport coefficients [120].

2.4. Reduced MHD

The MHD equations discussed in the previous section can be further simplified by assuming that the plasma is immersed in a strong, almost constant magnetic field in the axial direction. Here, by strong magnetic field we mean that both the kinetic and internal energy densities are much smaller than the magnetic energy, i.e.,

$$\rho v^2 \sim p \ll \frac{\mathrm{B}^2}{\mu_0} \tag{2.13}$$

This equation also implies that the value of beta (β) is much smaller than unity, i.e.;

$$\beta = p/(B^2/\mu_0) \ll 1) \tag{2.14}$$

Under such conditions, we will derive the simplified version of the MHD model that describes the plasma dynamics in the plane perpendicular to the strong guide magnetic field. The resulting simplified model is called reduced MHD. In this derivation, we mostly follow the work of Strauss [116].

2.4.1. Ordering

The variables in the MHD equations are ordered to some power of the small parameter ϵ. Only the terms with small power of ϵ are retained. Since we have assumed that the axial component of the magnetic field, $\mathbf{B}_{z0}$ is much larger than the other components, thus we can write;

$$\frac{B_\perp}{B_{z0}} \ll 1, \tag{2.15}$$

where $\mathbf{B}_\perp$ represents the components of the magnetic field perpendicular to the strong axial field. In the present coordinate system, these are the x and y components. Following the equation (2.14), we can get;

$$B_\perp \sim \epsilon, \;\; B_{z0} \sim 1. \tag{2.16}$$

To remove the fastest time scales, we assume the ordering $\partial/\partial t \sim \epsilon$. The other necessary ordering is as follows:

$$\nabla_{\perp} \sim 1,\ \partial_z \sim \epsilon,\ \tilde{B}_z \sim \epsilon^2,\ p \sim \epsilon^2,\ v \sim \epsilon,\ \eta \sim \epsilon,$$

where $\tilde{B}_z$ denotes the small changes in the magnetic field along the z-axis. Note that $\nabla_{\perp}$and ∂_z represent the derivative in the perpendicular and parallel direction of the strong guide field. Moreover, the flow is assumed to be incompressible which leads to the equipartitioning of the energy, i.e. $\rho v^{\,2} \sim p \sim B^2\,/\mu_0 \sim \epsilon$. The incompressibility of the flow allows us to presume the plasma density as constant ($\rho = \text{constant} = 1$).

The total magnetic field can be expressed as the summation of the parallel and perpendicular components, i.e. $\mathbf{B} = \mathbf{B_{\perp}} + B_z \mathbf{e}_z$. In general the magnetic field can be written in the form of vector potential **A**, so that;

$$\mathrm{B} = \nabla \times \mathrm{A} \sim \nabla_{\perp} \times A_{||} \mathrm{e_z} + \nabla_{\perp} \times \mathrm{A}_{\perp}$$

This implies that the parallel and perpendicular components of the magnetic field can be written by; $\mathbf{B}_{\perp} = \boldsymbol{\nabla}_{\perp} \times A_{||} \mathbf{e}_z$ and $B_z \mathbf{e}_z = \boldsymbol{\nabla}_{\perp} \times \mathbf{A}_{\perp}$.

We now define a magnetic flux function, $A_{||} = -\psi$ and express the total magnetic field in terms of it;

$$\mathbf{B} \ = \ B_z \mathbf{e}_z + \mathbf{e}_z \times (\boldsymbol{\nabla}_{\perp} \psi) \tag{2.17}$$

Note that the magnetic field in this form still satisfies the zero divergence condition, i.e.

$$\boldsymbol{\nabla} \,.\, \mathbf{B} = \epsilon^3 \partial_z \tilde{B}_z \sim 0. \tag{2.18}$$

Next, we derive the ordering of the current density using the ampere's law as follows:

$$\mu_0 \mathbf{J} = \boldsymbol{\nabla} \times \mathbf{B}$$

$$\Rightarrow \ \mu_0 (\mathrm{J_z} \mathbf{e}_z + \mathbf{J}_{\perp}) = \left(\boldsymbol{\nabla}_{\perp} + \boldsymbol{\nabla}_{||}\right) \times (\mathbf{B}_{\perp} + \mathbf{B}_{||})$$

$$\Rightarrow \ \mu_0 \mathrm{J_z} \mathbf{e}_z = \boldsymbol{\nabla}_{\perp} \times \mathbf{B}_{\perp}$$

$$= \epsilon \, \nabla_{\perp} \times (\mathrm{e_z} \times \nabla_{\perp} \psi)$$

$$= \epsilon \, \nabla_{\perp}^2 \psi \, \mathrm{e_z}\,, \ \Rightarrow \mathrm{J_z} \sim \ \epsilon$$

Also;

$$\mu_0 \mathbf{J}_{\perp} = \boldsymbol{\nabla}_{\perp} \times B_z \mathbf{e}_z + \partial_z \mathbf{e}_z \times \mathbf{B}_{\perp}$$

$$= \epsilon^2 \boldsymbol{\nabla}_{\perp} \times \tilde{B}_z \mathbf{e}_z + \epsilon^2 \partial_z \mathbf{e}_z \times \mathbf{B}_{\perp}$$

$$\Rightarrow \mathbf{J}_{\perp} \sim \epsilon^2$$

The incompressibility of the velocity field allows us to define a stream function ϕ:

$$\mathbf{v}_{\perp} = \mathbf{e}_z \times (\boldsymbol{\nabla}_{\perp}\phi) \tag{2.19}$$

Another convenient form of the perpendicular velocity can be expressed as;

$$\begin{pmatrix} v_x \\ v_y \end{pmatrix} = \begin{pmatrix} -\partial_y \phi \\ \partial_x \phi \end{pmatrix}$$

From the above definition, it's straight forward to prove that the flow is incompressible in perpendicular plane;

$$\boldsymbol{\nabla}_{\perp}.\mathbf{v}_{\perp} = \boldsymbol{\nabla}_{\perp}.\ (\mathbf{e}_{\mathrm{z}} \times \boldsymbol{\nabla}_{\perp}\phi) = 0. \tag{2.20}$$

2.4.2. Derivation of the incompressible two field equations

2.4.2.1. Ohm's law

In order to derive the Ohm's law, we start from the Faraday's law:

$$\boldsymbol{\nabla} \times \mathbf{E} = -\frac{\partial \mathbf{B}}{\partial t} = -\frac{\partial \mathbf{B}_{\perp}}{\partial t} - \frac{\partial \tilde{B}_{\mathrm{z}}\, \mathbf{e}_{\mathrm{z}}}{\partial t}$$

$$= -\frac{\partial}{\partial t}(\mathbf{e}_{\mathrm{z}} \times \boldsymbol{\nabla}_{\perp}\psi) - \frac{\partial \tilde{B}_{\mathrm{z}}\, \mathbf{e}_{\mathrm{z}}}{\partial t}$$

$$= \boldsymbol{\nabla} \times \left(\frac{\partial \psi\, \mathbf{e}_{\mathrm{z}}}{\partial t}\right) - \boldsymbol{\nabla} \times \mathbf{E}_{\perp}$$

$$\Rightarrow \mathbf{E} = \frac{\partial \psi\, \mathbf{e}_{\mathrm{z}}}{\partial t} + \mathbf{E}_{\perp} \tag{2.21}$$

Let insert equation (2.21) into equation (2.8), we get;

$$\frac{\partial \psi\, \mathbf{e}_{\mathrm{z}}}{\partial t} + \mathbf{E}_{\perp} = -\mathbf{v} \times \mathbf{B} + \eta \mathbf{J} \tag{2.22}$$

The ordering of the above equation is given as follows:

$$\epsilon^2 \frac{\partial \psi\, \mathbf{e}_{\mathrm{z}}}{\partial t} + \epsilon^3 \mathbf{E}_{\perp} = -\epsilon \mathbf{v}_{\perp} \times \mathrm{B}_{z0}\mathbf{e}_{\mathrm{z}} - \epsilon^2 \mathbf{v}_{\perp} \times \mathbf{B}_{\perp} - \epsilon^3 \mathbf{v}_{\perp} \times \tilde{B}_z \mathbf{e}_{\mathrm{z}}$$

$$-\epsilon^2 v_z \mathbf{e}_{\mathrm{z}} \times \mathbf{B}_{\perp} + \epsilon^3 \eta \mathbf{J}_{\perp} + \epsilon^2 \eta \mathrm{J}_{\mathrm{z}} \mathbf{e}_{\mathrm{z}}$$

Considering the second order terms $O\ (\epsilon^2)$:

$$\frac{\partial \psi\ \mathbf{e}_z}{\partial t} = -\epsilon^2 \mathbf{v}_\perp \times \mathbf{B}_\perp - \epsilon^2 v_z \mathbf{e}_z \times \mathbf{B}_\perp + \epsilon^2 \eta \mathrm{J}_z \mathbf{e}_z \tag{2.23}$$

The parallel component of equation (2.23) is given as follows:

$$\frac{\partial \psi}{\partial t} = -\mathbf{v}_\perp \times \mathbf{B}_\perp - v_z \mathbf{e}_z \times \mathbf{B}_\perp + \eta \mathrm{J}_z \mathbf{e}_z \tag{2.24}$$

Using the fact that, $\mu_0 \mathrm{J}_z = \boldsymbol{\nabla}_\perp^2 \psi$ and $\mathbf{B}_\perp = \mathbf{e}_z \times \boldsymbol{\nabla}_\perp \psi$, the above equation can be reformulated to get the Ohm's law:

$$\frac{\partial \psi}{\partial t} = -\mathbf{v}_\perp \times (\mathbf{e}_z \times \boldsymbol{\nabla}_\perp \psi) - v_z \mathbf{e}_z \times (\mathbf{e}_z \times \boldsymbol{\nabla}_\perp \psi) + \frac{\eta}{\mu_0}\ \boldsymbol{\nabla}_\perp^2 \psi\ \mathbf{e}_z \tag{2.25}$$

$$\Rightarrow\ \frac{\partial \psi}{\partial t} = -(\mathbf{v}_\perp \cdot \boldsymbol{\nabla})\psi + \frac{\eta}{\mu_0}\ \boldsymbol{\nabla}_\perp^2 \psi \tag{2.26}$$

The first term on the right hand of the above equation can be expressed in the form of Poisson bracket using the property;

$$(\mathrm{v}_\perp \cdot \nabla)\mathrm{A} = ((\mathrm{e}_z \times \nabla\phi) \cdot \nabla)\mathrm{A} = [\phi, \mathrm{A}],$$

where, the Poisson bracket is defined as $[A,\ B] = \partial_x A \partial_y B - \partial_y A \partial_x B$.

Finally, the Ohm's is written as follows:

$$\frac{\partial \psi}{\partial t} = -[\phi, \psi] + \frac{\eta}{\mu_0} \boldsymbol{\nabla}_\perp^2 \psi. \tag{2.27}$$

This equation basically determines the evolution of the magnetic flux ψ. In order to solve this equation, we also need the kinetic flow ϕ, which is discussed next.

2.4.2.2. Derivation of the equation of motion

We start from the equation of motion (2.2):

$$\frac{d\mathbf{v}}{dt} = \mathbf{J} \times \mathbf{B} - \boldsymbol{\nabla} p,$$

where we have applied the constant density assumption, i.e. $\rho = \text{constant} = 1$. Using the ampere's law $\boldsymbol{\nabla} \times \mathbf{B} = \mu_0 \mathbf{J}$ and the identity:

$$(\boldsymbol{\nabla}\times\mathbf{B})\times\mathbf{B}=(\mathbf{B}\cdot\boldsymbol{\nabla})\mathbf{B}-\frac{1}{2\mu_0}\boldsymbol{\nabla}B^2,$$

The equation of motion can be rewritten as:

$$\frac{\partial\mathbf{v}}{\partial t}+(\mathbf{v}\,.\,\boldsymbol{\nabla})\mathbf{v}=(\mathbf{B}\cdot\boldsymbol{\nabla})\mathbf{B}-\frac{1}{2\mu_0}\boldsymbol{\nabla}B^2-\boldsymbol{\nabla}p. \tag{2.28}$$

Expressing each term in ϵ orders; the second order ($O\,\epsilon^2$) in the perpendicular direction gives:

$$\frac{\partial\mathbf{v}_\perp}{\partial t}+(\mathbf{v}_\perp\,.\,\boldsymbol{\nabla}_\perp)\mathbf{v}_\perp$$

$$=\frac{1}{\mu_0}(\mathbf{B}_\perp\cdot\boldsymbol{\nabla}_\perp)\mathbf{B}_\perp+\frac{1}{\mu_0}\mathrm{B_{z0}}\left(\partial_z\mathbf{B}_\perp-\boldsymbol{\nabla}_\perp\tilde{B}_\mathrm{z}\right)-\frac{1}{2\mu_0}\boldsymbol{\nabla}_\perp\mathrm{B_\perp}^2-\boldsymbol{\nabla}_\perp p. \tag{2.29}$$

From the fourth order ($O\,\epsilon^4$) of equation (2.28) results in $\partial_z\mathbf{B}_\perp=\boldsymbol{\nabla}_\perp\tilde{B}_\mathrm{z}$; equation (2.29) is rearranged using this property:

$$\frac{\partial\mathbf{v}_\perp}{\partial t}+(\mathbf{v}_\perp\,.\,\boldsymbol{\nabla}_\perp)\mathbf{v}_\perp=\frac{1}{\mu_0}(\mathbf{B}_\perp\cdot\boldsymbol{\nabla}_\perp)\mathbf{B}_\perp-\frac{1}{2\mu_0}\boldsymbol{\nabla}_\perp\mathrm{B_\perp}^2-\boldsymbol{\nabla}_\perp p. \tag{2.30}$$

The above equation is operated by "$\mathbf{e}_z\cdot\boldsymbol{\nabla}\times$"on both sides, so that the unnecessary terms of hydromagnetic and magnetic pressure are eliminated:

$$\mathrm{e}_z\cdot\nabla_\perp\times\frac{\partial\mathrm{v}_\perp}{\partial t}+\mathrm{e}_z\cdot(\nabla_\perp\times(\mathrm{v}_\perp\,.\,\nabla_\perp)\mathrm{v}_\perp)=\frac{1}{\mu_0}(\mathrm{e}_z\cdot\nabla_\perp\times(\mathrm{B}_\perp\cdot\nabla_\perp)\mathrm{B}_\perp) \tag{2.30}$$

Each term of this equation is simplified separately as follows:

First term on right hand side of equation (2.30) is:

$$\mathrm{e}_z\cdot\nabla_\perp\times\frac{\partial\mathrm{v}_\perp}{\partial t}=\mathrm{e}_z\cdot\frac{\partial}{\partial t}(\nabla_\perp\times\mathrm{v}_\perp),$$

$$=\mathrm{e}_z\cdot\frac{\partial}{\partial t}(\nabla_\perp\times\ (\mathrm{e}_\mathrm{z}\times\nabla_\perp\phi)),$$

$$=\frac{\partial}{\partial t}\left(\nabla_\perp^2\phi\right),$$

where the term in parenthesis is defined as the parallel component of the vorticity, i.e.;

$$\omega = \mathbf{e}_z \cdot (\boldsymbol{\nabla}_\perp \times \mathbf{v}_\perp) = \boldsymbol{\nabla}_\perp^2 \phi. \tag{2.31}$$

Second term on right hand side of equation (2.30):

$$\begin{aligned} \mathrm{e}_z \cdot (\nabla_\perp \times (\mathrm{v}_\perp . \nabla_\perp)\mathrm{v}_\perp) &= \mathrm{e}_z \cdot \left(\nabla_\perp \times (\mathrm{e}_z \times \nabla_\perp \phi . \nabla_\perp)\ (\mathrm{e}_z \times \nabla_\perp \phi)\right) \\ &= \mathrm{e}_z \cdot \left((\nabla_\perp \times\ (\mathrm{e}_z \times \nabla_\perp \phi))(\mathrm{e}_z \times \nabla_\perp \phi . \nabla_\perp)\right) \\ &= \left(\mathrm{e}_z \cdot (\nabla_\perp^2 \phi\ \mathrm{e}_z)\right)(\mathrm{e}_z \times \nabla_\perp \phi . \nabla_\perp) \\ &= (\mathbf{e}_z \times \boldsymbol{\nabla}_\perp \phi . \boldsymbol{\nabla}_\perp)\boldsymbol{\nabla}_\perp^2 \phi \end{aligned}$$

The term on left hand side of equation (2.30):

$$\begin{aligned} \frac{1}{\mu_0}(\mathrm{e}_z \cdot \nabla_\perp \times (\mathrm{B}_\perp \cdot \nabla_\perp)\mathrm{B}_\perp) &= \frac{1}{\mu_0}\left(\mathrm{e}_z \cdot \left(\nabla_\perp \times ((\mathrm{e}_z \times \nabla_\perp \psi) \cdot \nabla_\perp)(\mathrm{e}_z \times \nabla_\perp \psi)\right)\right) \\ &= \frac{1}{\mu_0}\left(\mathbf{e}_z \cdot (\boldsymbol{\nabla}_\perp \times (\mathbf{e}_z \times \boldsymbol{\nabla}_\perp \psi))(\mathbf{e}_z \times \boldsymbol{\nabla}_\perp \psi \cdot \boldsymbol{\nabla}_\perp)\right) \\ &= \frac{1}{\mu_0}\left(\mathbf{e}_z \cdot \boldsymbol{\nabla}_\perp^2 \psi \mathbf{e}_z\right)(\mathbf{e}_z \times \boldsymbol{\nabla}_\perp \psi\ \ \cdot \boldsymbol{\nabla}_\perp) \\ &= \frac{1}{\mu_0}\ (\mathbf{e}_z \times \boldsymbol{\nabla}_\perp \psi \cdot \boldsymbol{\nabla}_\perp)\boldsymbol{\nabla}_\perp^2 \psi \end{aligned}$$

Applying these simplifications into equation (2.30), we obtain:

$$\frac{\partial}{\partial t}\left(\boldsymbol{\nabla}_\perp^2 \phi\right) + (\mathbf{e}_\mathrm{z} \times \boldsymbol{\nabla}_\perp \phi . \boldsymbol{\nabla}_\perp)\boldsymbol{\nabla}_\perp^2 \phi = \frac{1}{\mu_0}\ (\mathbf{e}_z \times \boldsymbol{\nabla}_\perp \psi \cdot \boldsymbol{\nabla}_\perp)\boldsymbol{\nabla}_\perp^2 \psi. \tag{2.32}$$

Introducing the Poisson brackets and adding the viscosity term:

$$\frac{\partial(\nabla^2 \phi)}{\partial t} = -[\phi, \nabla^2 \phi] + \frac{1}{\mu_0}[\psi, \nabla^2 \psi] + \mu \nabla^2 (\nabla^2 \phi) \tag{2.37}$$

This equation gives the evolution of the plasma flow, which can also be expressed in terms of parallel component of the plasma vorticity:

$$\frac{\partial \omega}{\partial t} = -[\phi, \omega] + \frac{1}{\mu_0}[\psi, \mathrm{J_z}] + \mu \nabla^2 \omega \tag{2.38}$$

Thus the reduced MHD equations (2.27) and (2.38) are solved simultaneously to find out the evolution of the magnetic flux and plasma vorticity.

2.5. Normalizations

The two field reduced MHD equations obtained in the previous section are normalized with the following considerations:

- Lengths are normalized to some characteristic length a (layer width of the current carrying region near the singular surface).
- Time is normalized to the Alfvén time, $\tau_A = a \,/\, v_A$, where v_A is Alfvén velocity defined by $v_A = B_0/\sqrt{\mu_0\rho_0} = B_0/\sqrt{\mu_0}$ (assuming that $\rho_0 = 1$) .
- The magnetic field is normalized to the in-plane guide magnetic field B_0.

With these normalizations, the fields are represented as follows:

$$\hat{\psi} = \frac{\psi}{aB_0}, \qquad \hat{\phi} = \frac{\phi}{av_A},$$

$$\hat{k}_y = ak_y, \qquad \hat{B}_{0y}(x) = \frac{\mathrm{B}_{0y(x)}}{B_0}.$$

Implementing the above normalization (see Appendix A), the RMHD equations are:

$$\partial_{\hat{t}}\hat{\psi} = -\left[\hat{\phi}, \hat{\psi}\right] + \hat{\eta}\hat{\nabla}^2\hat{\psi}, \tag{2.39}$$

$$\partial_{\hat{t}}\left(\hat{\nabla}^2\phi\right) = -\left[\hat{\phi}, \hat{\nabla}^2\hat{\phi}\right] + \left[\hat{\psi}, \hat{\nabla}^2\hat{\psi}\right] + \mu\hat{\nabla}^2\left(\hat{\nabla}^2\hat{\phi}\right), \tag{2.40}$$

where, $\hat{\eta} = \eta/\mu_0 a v_A = 1 \,/\, S$, ($S$ represents the Lundquist number and is also defined as the ratio of the resistive to Alfvén times). In addition, the diffusion of the equilibrium magnetic field in the Ohm's is prevented by adding an externally applied electric field $E_0 = -\eta\nabla^2\psi_0$ to the right-hand side of equation (3). Thus, dropping the hats, the final form of the normalized RMHD equations is given as follows:

$$\partial_t\psi = -[\phi, \psi] + \eta\nabla^2(\psi - \psi_0), \tag{2.41}$$

$$\partial_t(\nabla^2\phi) = -[\phi, \nabla^2\phi] + [\psi, \nabla^2\psi] + \mu\nabla^2(\nabla^2\phi). \tag{2.42}$$

The above two equations are actually solved in our simulation studies to analyze the evolution of the perturbed flux and plasma flow.

2.6. Summary

In this chapter, we derived the reduced MHD equations, starting from the full length MHD equation system. Before, presenting the rigorous derivation details of the reduced MHD equations, we present the comparison of the simplified Ohm's law and its generalized form. The terms which are missing from the simplified Ohm's law are described one by one. The significance of each term and the corresponding assumptions for their omission are detailed. The variables in the MHD equations are then ordered to some power of the small parameter ϵ. A strong axial component of the magnetic field, $\mathbf{B}_{z0}$ is assumed in the system. In deriving the reduced MHD equations, i.e. the Ohm's law and equation of motion, we introduce the stream function ϕ and the magnetic flux function ψ. After deriving the two field RMHD equations, the variables are normalized to the system physical parameters. Finally, we obtain the normalized RMHD equations, which can be solved through simulations to find out the time evolution of the plasma vorticity and magnetic flux instantaneously.

Chapter 3

Resistive Tearing Mode Instability

3.1. Introduction

According to the classical tearing mode theory, the tearing mode evolution consists of three distinct stages: first is the linear stage, described by the well known Furth-Killeen-Rosenbluth (FKR) theory [52]. During this phase, the reconnection grows exponentially and the magnetic island width W also grows at the same rate. When the island width is comparable to resistive layer width, nonlinear effects comes into play and the FKR theory is no more valid. In this stage of evolution, the magnetic island grows linearly in time, i.e. $dW/dt \sim \eta\Delta'$, where η is the plasma resistivity and Δ' is the instability parameter. This second slow phase of the tearing mode growth is known as Rutherford regime [53]. Finally, the magnetic island growth gets saturated as most of the available magnetic flux is reconnected. This phase of evolution is called the saturation stage.

In this chapter, we analyze the standard linear theory of the resistive tearing mode. The validity of the FKR model is discussed under various conditions. Then, we derive the instability parameter for different equilibrium profiles. After the analytical description, we introduce the simulation model for solving the RMHD system and elaborate the relevant numerical schemes. Finally, a comparison of the simulation results with theory is presented for the linear tearing mode evolution.

3.2. Linear Tearing Mode Theory

This analysis is based on the original work of Furth *et al.* [52] and we reproduce their final results following the style of [121]. We start our analysis from the RMHD equations (2.27)

and (2.38), derived in the previous chapter. These two equations are linearized by splitting the magnetic flux ψ and plasma flow ϕ into the equilibrium and perturbation parts, i.e.

$$\psi(x,t) = \psi_0(x,t) + \psi_1(x,t), \tag{3.1}$$

$$\phi(x,t) = \phi_0(x,t) + \phi_1(x,t). \tag{3.2}$$

The initial equilibrium of plasma is, $\boldsymbol{B}_{0y} = (\partial\psi_0/\partial x)\boldsymbol{e}_y = \bar{B}_0\, f(x)\boldsymbol{e}_y$ and $\phi_0 = 0$, which means that plasma is considered to be stationary (equilibrium flows are zero).Note that $f(x)$ is chosen to be odd function i.e. $f(-x) = -f(x)$. Suppose that all perturbations are expressed as, $A(x,t) = A(x)e^{ik_y y+\gamma t}$, then the flux and flow can be expressed as follows:

$$\psi(x,y,t) = \psi_0(x) + \psi_1(x)e^{ik_y y+\gamma t}, \tag{3.3}$$

$$\phi(x,y,t) = \phi_1(x)e^{ik_y y+\gamma t}, \tag{3.4}$$

where γ is the linear growth rate of the tearing instability. With these expressions of the magnetic flux and plasma flow, the ohm's law (equation (2.27)) is rewritten as:

$$\frac{\partial\psi}{\partial t} + \frac{\partial\phi}{\partial x}\frac{\partial\psi}{\partial y} - \frac{\partial\phi}{\partial y}\frac{\partial\psi}{\partial x} = \frac{\eta}{\mu_0}\left(\frac{\partial^2(\psi-\psi_0)}{\partial x^2} + \frac{\partial^2\psi}{\partial y^2}\right) \tag{3.5}$$

$$\Rightarrow \partial_t(\psi_0 + \psi_1 e^{ik_y y+\gamma t}) + \partial_x(\phi_1 e^{ik_y y+\gamma t}).\,\partial_y(\psi_0 + \psi_1 e^{ik_y y+\gamma t}) - \partial_y(\phi_1 e^{ik_y y+\gamma t})$$

$$\partial_x(\psi_0 + \psi_1 e^{ik_y y+\gamma t}) = \frac{\eta}{\mu_0}\left(\partial_x^2 + \partial_y^2\right)(\psi_0 + \psi_1 e^{ik_y y+\gamma t}) - \eta\partial_x^2\psi_0$$

$$\Rightarrow \gamma\,\psi_1 e^{ik_y y+\gamma t} + (\phi_1' e^{ik_y y+\gamma t})\left(ik_y\,\psi_1 e^{ik_y y+\gamma t}\right) - (ik_y\phi_1 e^{ik_y y+\gamma t})(\psi_0' + \psi_1')e^{ik_y y+\gamma t}$$

$$= \frac{\eta}{\mu_0}\left(\psi_1'' e^{ik_y y+\gamma t} - k_y^2\,\psi_1 e^{ik_y y+\gamma t}\right)$$

Note that here, the prime represents derivative along *x*. By taking the first order of the above equation, we obtain:

$$\gamma\,\psi_1 e^{ik_y y+\gamma t} - (ik_y\phi_1 e^{ik_y y+\gamma t})\psi_0' = \frac{\eta}{\mu_0}\left(\psi_1'' e^{ik_y y+\gamma t} - k_y^2\,\psi_1 e^{ik_y y+\gamma t}\right)$$

$$\Rightarrow \gamma\,\psi_1 - ik_y\phi_1\,\psi_0' = \frac{\eta}{\mu_0}\left(\psi_1'' - k_y^2\,\psi_1\right)$$

$$\Rightarrow \gamma\,\psi_1 - ik_y\phi_1\,\bar{B}_0\,f(x) = \frac{\eta}{\mu_0}\left(\partial_x^2 - k_y^2\right)\psi_1 \tag{3.6}$$

Next, we linearize the equation of motion in the same manner:

$$\partial_t(\nabla^2\phi) + \partial_x\phi.\partial_y\nabla^2\phi - \partial_y\phi.\partial_x\nabla^2\phi = \partial_x\psi.\partial_y\nabla^2\psi - \partial_y\psi.\partial_x\nabla^2\psi$$

$$\Rightarrow (\gamma\phi_1'' - k_y^2\phi_1)e^{ik_y y+\gamma t} = ik_y\psi_0'(\psi_1'' - k_y^2\,\psi_1)e^{ik_y y+\gamma t} - ik_y\psi_0'''\,\psi_1\,e^{ik_y y+\gamma t}$$

$$\Rightarrow \gamma(\partial_x^2 - k_y^2)\phi_1 = ik_y\psi_0'(\psi_1'' - k_y^2\,\psi_1) - ik_y\psi_0'''\,\psi_1$$

$$\Rightarrow \gamma(\partial_x^2 - k_y^2)\phi_1 = ik_y\bar{B}_0\,f(x)(\partial_x^2 - k_y^2)\,\psi_1 - ik_y\bar{B}_0\,f''(x)\,\psi_1,$$

where, we have used the definitions, $\psi_0' = \bar{B}_0\,f(x)$ and $\psi_0''' = \bar{B}_0\,f''(x)$.

$$\Rightarrow \gamma(\partial_x^2 - k_y^2)\left(\frac{\phi_1}{ik_y\bar{B}_0}\right) = f(x)(\partial_x^2 - k_y^2)\,\psi_1 - f''(x)\,\psi_1$$

$$\Rightarrow \gamma^2 a(\partial_x^2 - k_y^2)\left(\frac{i\phi_1}{\gamma}\right)\left(\frac{1}{ak_y\bar{B}_0}\right) = f''(x)\,\psi_1 - f(x)(\partial_x^2 - k_y^2)\,\psi_1 \qquad (3.7)$$

Let introduce the hydromagnetic and resistive times: $\tau_H = 1/(ak_y\bar{B}_0)$ and $\tau_\eta = \mu_0 a^2/\eta$ into the equations (3.6) and (3.7) along with the simplification, $i\phi_1/\gamma\tau_H = \phi_1$, we finally get:

$$\gamma^2\tau_H^2 a(\partial_x^2 - k_y^2)\phi_1 = f''(x)\,\psi_1 - f(x)(\partial_x^2 - k_y^2)\,\psi_1 \qquad (3.8)$$

$$\psi_1 - \frac{f(x)}{a}\phi_1 = \frac{a^2}{\gamma\tau_\eta}(\partial_x^2 - k_y^2)\,\psi_1 \qquad (3.9)$$

Thus, the linearized RMHD equations (3.8) and (3.9) are solved to calculate the Eigen functions ψ_1 and ϕ_1 corresponding to Eigen-value γ. However, before proceeding further, it is important to consider some assumptions:

The tearing mode grows on a hybrid time scales, which is much small than τ_η but much greater than τ_H, i.e. $1/\tau_H \ll \gamma \ll 1/\tau_\eta$. Note that the plasma resistivity is important only in a small region of width $\delta \ll a$, near the $x = 0$. Thus the plasma can be divided into two regions: outer region and inner region.

3.2.1. Outer Region

The whole plasma domain outside the thin resistive layer is called the outer region, i.e. $|x| \gg \delta$. In this region, the contribution of plasma resistivity and inertia can be ignored. Thus, neglecting the plasma inertia (left-hand side of equation (3.8)) and plasma resistivity (right-hand side of equation (3.9)), these two equations are reduced to the following form:

$$f''(x)\,\psi_1 - f(x)\left(\partial_x^2 - k_y^2\right)\psi_1 = 0 \tag{3.10}$$

$$\phi_1 = \frac{\psi_1}{f(x)/a} \tag{3.11}$$

Let simplify Equation (3.10) further, we obtain:

$$f''(x)\,\psi_1 = f(x)\left(\partial_x^2 - k_y^2\right)\psi_1$$

$$\Rightarrow\ f''(x)\,\psi_1 = f(x)\psi_1'' - f(x)k_y^2\,\psi_1$$

$$\Rightarrow\ \psi_1'' = \frac{f''(x)}{f(x)}\,\psi_1 + k_y^2\,\psi_1$$

$$\Rightarrow\ \psi_1'' = \left(k_y^2 + \frac{\mathrm{J}_0'}{\mathrm{B}_{0y}}\right)\psi_1 \tag{3.12}$$

Equation (3.12) describes the flux freezing condition, where the plasma is bound to the magnetic field lines. Actually, this equation is the linearized form of the static force balance criteria, i.e. $\nabla \times (\mathrm{J} \times \mathrm{B}) = 0$. Note that equations (3.11) and (3.12) are the ideal MHD equations and valid in most region of the plasma, except in the vicinity of $f(x) = 0$, i.e., where the magnetic field reverses direction as shown in Figure. (3.1). Thus there is a thin layer in the vicinity of $x = 0$, where the plasma inertia and resistivity becomes important and can't be neglected.

3.2.2. Inner Region

In the inner thin region $|x| \ll 1$, the plasma inertia and resistivity can no longer be neglected. Thus we have to solve the full version of the linearized RMHD equations (3.8) and (3.9). The inner region solution is then matched at the boundary layer to the outer

solution of equations (3.11) and (3.12). Making use of the fact that $d/dx \gg k$ and $f(x) \approx x$, the linearized equations in the inner thin layer reduces to:

$$\psi_1 - \frac{x}{a}\phi_1 = \frac{a^2}{\gamma\tau_\eta}\psi_1'' \tag{3.13}$$

$$\gamma^2\tau_H^2\phi_1'' = -\frac{x}{a}\psi_1'' \tag{3.14}$$

Let us consider the solution of ideal MHD equation (3.12) at large positive x, which satisfies the physical boundary conditions as $x \to 0$ and integrate this solution to the inner layer boundary at $x = 0_+$. In the same way, we could consider the solution at large negative x and integrate this solution to $x = 0_-$. Now, we have to multiply some factors to make sure that the magnetic flux matches on both sides of the thin layer. Thus, the problem becomes very simple, just finding these constant numerical factors. Note that the flux derivate ψ_1' is discontinuous at the two sides of the resistive layer. This jump in the logarithmic derivative of the flux ψ_1 to the left and right of the layer is expressed by the parameter Δ' as follows:

$$\Delta' = \left[\frac{d}{dx}\ln\psi_1\right]_{x=0_-}^{x=0_+} \tag{3.15}$$

The parameter Δ' is known as the plasma instability parameter, which only depends on the plasma equilibrium and the wave number. This is a fundamental quantity in tearing mode theory. It has been shown by Furth *et al.* [52] that the linear tearing mode is unstable only and only if $\Delta' > 0$.

- Constant-ψ approximation:

The flux variation inside the resistive tearing layer is given by:

$$\frac{\delta\psi_1}{\psi_1} \sim \frac{\psi_1'}{\psi_1}\delta \sim \Delta'\delta$$

For small enough Δ', the $\Delta'\delta \ll 1$ can be assumed to be approximately constant in the tearing layer. The assumption that the magnetic flux inside the resistive layer is constant is known as the constant-ψ approximation. The validity of this approximation will be

discussed later in this chapter. With the constant-ψ approximation, equation (3.13) takes the following form:

$$\psi_1(0) - \frac{x}{a}\phi_1 = \frac{a^2}{\gamma\tau_\eta}\psi_1'' \tag{3.16}$$

A matching condition for the exterior and interior solutions can be obtained by integrating equation (3.14) over the inner region

$$-\gamma^2\tau_H^2 \int_{-x}^{+x} \frac{\phi_1''}{x/a} dx = \int_{-x}^{+x} \psi_1'' dx. \tag{3.17}$$

Let note that the right hand side integral can be simplified further as:

$$\int_{-x}^{+x} \psi_1'' dx = \psi_1'|_x - \psi_1'|_{-x} = \psi_1(0)\Delta' \tag{3.18}$$

Using this relation in equation (3.17), we get:

$$-\frac{\gamma^2\tau_H^2}{\psi_1(0)} \int_{-x}^{+x} \frac{\phi_1''}{x/a} dx = \Delta' \tag{3.19}$$

Let combine equations (3.13) and (3.16) to get an expression for ϕ_1:

$$\frac{\gamma\tau_H^2}{\tau_\eta}\phi_1'' = -\frac{x}{a}\left[\psi_1(0) - \frac{x}{a}\phi_1\right] \tag{3.20}$$

To simplify the above expression we introduce the following transformation of variables:

$$\frac{x}{a} = \left(\frac{\gamma\tau_H^2}{\tau_\eta}\right)^{1/4} w \tag{3.21}$$

$$\phi_1 = \left(\frac{\gamma\tau_H^2}{\tau_\eta}\right)^{-1/4} \psi_1(0)\chi \tag{3.22}$$

With the above transformation, equation (3.20) can be reduced to the following simple form:

$$\chi'' - w^2\chi = w \tag{3.23}$$

The solution of the above equation was given in Ref [122].

$$\chi(w) = -\frac{w}{2}\int_0^{\pi/2} sin^{1/2}\theta \; exp\left(-\frac{w^2 cos\theta}{2}\right) d\theta \tag{3.24}$$

In terms of the new variables, the matching condition, equation (3.19) is rewritten as:

$$\gamma^{5/4}\tau_H^{1/2}\tau_\eta^{3/4}\int_{-\infty}^{\infty}\frac{dw}{w}\chi'' = \Delta' a \tag{3.25}$$

Note that in deriving the above expression we have used the fact that the limits of equation (3.19) can be extended to infinity with a minimum error. Now the term $\chi''(w)/w$ can be truncated at $w = 2$ with a minimum error. Hence, the tearing layer width can be expressed as:

$$\frac{\delta}{a} = 2\left(\frac{\gamma\tau_H^2}{\tau_\eta}\right)^{1/4} \tag{3.26}$$

When the range of integration is truncated at $w = 2$, the integral in equation (3.25) can be approximated by:

$$\int_{-\infty}^{\infty}\frac{dw}{w}\chi'' = \frac{4}{3}\sqrt{2}\,\Gamma(3/4)\Gamma(7/4) \sim 2.1 \tag{3.27}$$

Inserting this into equation (3.25), after simplification we finally obtain the scaling of the growth rate and resistive layer width:

$$\gamma \approx 0.55\,\tau_\eta^{-3/5}\,\tau_H^{-2/5}\,(\Delta' a)^{4/5} \tag{3.28}$$

$$\frac{\delta}{a} \approx 1.72\,\tau_\eta^{-2/5}\,\tau_H^{2/5}\,(\Delta' a)^{1/5} \tag{3.29}$$

Alternatively these scalings can be written as:

$$\gamma \approx 0.55\,\eta^{3/5}\,(k\bar{B}_0)^{2/5}\,\Delta'^{4/5} \tag{3.30}$$

$$\delta \approx 1.72\,\eta^{2/5}\,(k\bar{B}_0)^{-2/5}\,\Delta'^{1/5} \tag{3.31}$$

Note that for the case of our chosen equilibrium $\bar{B}_0 = 2\bar{\psi}_0 = 2, \quad (\because \bar{\psi}_0 = 1)$. The validity of the constant-ψ approximation can now be assessed. As defined earlier, for the constant-ψ approximation to hold it has to satisfy the condition, $\Delta'\delta \ll 1$. This means that the resistive diffusion time across the tearing layer must be shorter than the instability growth time:

$$\tau_{\eta\delta} = \frac{\mu_0 \delta^2}{\eta} \ll \frac{1}{\gamma} \tag{3.32}$$

Using expressions (3.30) and (3.31), we finally obtain:

$$\eta \ll \frac{1}{(k\bar{B}_0)^{-1}\Delta'^3} \tag{3.33}$$

In the same the regime of validity of the FRK linear theory can be estimated using expressions (3.38) and (3.29), which results in:

$$\eta \ll \frac{a^{3/2}}{\tau_H \, \Delta'^{1/2}} \tag{3.34}$$

3.3. Non- constant-ψ Case

The constant-ψ approximation cannot be used if the condition (3.33) is not valid. The inner region problem has to be solved now without the constant-ψ approximation. The procedure we adopt to solve the non-constant-ψ case is almost the same as given by Coppi *et al.* [123], except that the matching condition is different for the internal kink mode. We start from the same equations as the previous case of constant-ψ, repeated here:

$$\psi_1 - \frac{x}{a}\phi_1 = \frac{a^2}{\gamma \tau_\eta} \psi_1'' \tag{3.35}$$

$$\gamma^2 \tau_H^2 \phi_1'' = -\frac{x}{a}\psi_1'' \tag{3.36}$$

Let introduce an auxiliary function defined as:

$$\chi(x) = x\psi_1'(x) - \psi_1(x) \tag{3.37}$$

Differentiating the above equation and combining with equation (3.36), we get:

$$\chi'(x) = x\psi_1''(x) \tag{3.38}$$

$$\chi'(x) = -a\gamma^2\tau_H^2\phi_1'' \tag{3.39}$$

Integrating the above equation with respect to x, we obtain:

$$\chi(x) = -a\gamma^2\tau_H^2\phi_1'(x) + \chi_\infty \tag{3.40}$$

where χ_∞ is an integration constant. An expression for $\psi_1'(x)$ can be obtained from equation (3.38):

$$\psi_1'(x) = \int_0^x \frac{\chi'}{x}\, dx \tag{3.41}$$

Integrating it once more with respect to x, we get:

$$\psi_1(x) = x\int_0^x \frac{\chi'}{x}\, dx - \chi(x) \tag{3.42}$$

Inserting the $\psi_1''(x)$ and $\psi_1(x)$ into equation (3.35) and divide it by x, we obtain:

$$\int_0^x \frac{\chi'}{{}^{x}/_{a}}\, dx - \frac{\chi}{{}^{x}/_{a}} - \phi_1 = \frac{a}{\gamma\tau_\eta}\frac{\chi'}{({}^{x}/_{a})^2} \tag{3.43}$$

Differentiating the above equation with respect to x, we get:

$$\frac{\gamma\tau_H^2}{\tau_\eta}\left(a\chi'' - 2a\,\frac{\chi}{{}^{x}/_{a}}\right) - [({}^{x}/_{a})^2 + \gamma^2\tau_H^2]\chi = -\chi_\infty({}^{x}/_{a})^2 \tag{3.44}$$

Applying the same transformation (equations (3.21) and (3.22)), we obtain:

$$\chi''(w) - \frac{2}{w}\chi'(w) - (w^2 + \lambda^{3/2})\chi = -\chi_\infty w^2 \tag{3.45}$$

Where, $\lambda = \gamma\tau_H^{2/3}\tau_\eta^{1/3}$.

The solution of the above equation can be expressed in integral form as follows:

$$\frac{\chi(w)}{\chi_\infty} = 1 - \frac{\lambda^{3/2}}{2}\int_0^1 (1-t)^{\frac{\lambda^{3/2}-5}{4}}(1+t)^{-\frac{\lambda^{3/2}+5}{4}} e^{-tw^2/2}\, dt \tag{3.46}$$

We now match the inner and the outer solution. For large enough value of x, equation (3.42) can be rewritten as:

$$\psi_1(x) = x\int_0^\infty \frac{\chi'}{x}\,dx - \chi_\infty - x\int_x^\infty \frac{\chi'}{x}\,dx \tag{3.42}$$

The third term on the RHS of this equation can be neglected, resulting in:

$$\psi_1(x) = x\int_0^\infty \frac{\chi'}{x}\,dx - \chi_\infty \tag{3.42}$$

In the overlap region, we can use $f(x) \approx x$ and simplifying equation (3.12) yields:

$$\psi_1(z) = \bar{\psi}_1 + \frac{x}{a}\bar{\bar{\psi}}_1 \tag{3.43}$$

$$\phi_1(z) = \frac{\psi_1}{x/a} \tag{3.44}$$

Using the definition of instability parameter Δ', we easily obtain:

$$\Delta' = \frac{2}{a}\frac{\bar{\bar{\psi}}_1}{\bar{\psi}_1} \tag{3.45}$$

Comparison of equation (3.42) and (3.43) result in the following correspondence:

$$\bar{\psi}_1 \to -\chi_\infty \tag{3.46}$$

$$\bar{\bar{\psi}}_1 \to \int_0^\infty \frac{\chi'}{x/a}\,dx \tag{3.47}$$

Thus using the above relations, the matching condition (equation (3.45)) becomes:

$$\Delta' a = -\frac{2}{\chi_\infty}\int_0^\infty \frac{\chi'}{x/a}\,dx \tag{3.48}$$

In terms of w, this can be written as:

$$\Delta' = -\frac{2}{\chi_\infty}\left(\frac{\gamma\tau_H^2}{\tau_\eta}\right)^{-1/4}\int_0^\infty \frac{\chi'(w)}{w}\,dw \tag{3.49}$$

Evaluating the integral, finally we obtain:

$$\Delta' a = -\frac{\pi}{8}\gamma^{5/4}\tau_H^{1/2}\tau_\eta^{3/4}\frac{\Gamma\left[\left(\lambda^{3/2}-1\right)/4\right]}{\Gamma[(\lambda^{3/2}+5)/4]} \quad (3.50)$$

The FKR scaling is recovered for $\lambda \ll 1$:

$$\gamma = 0.55\,\tau_\eta^{-3/5}\tau_H^{-2/5}\,(\Delta' a)^{4/5} \quad (3.51)$$

Next consider the limiting case $\lambda \to 1^-$:

From the series expansion of the gamma function, we know that $\Gamma(z) \approx 1/z$. Therefore, for small argument value, we can write;

$$\Gamma[\left(\lambda^{\frac{3}{2}}-1\right)/4] \approx \frac{4}{\left(\lambda^{\frac{3}{2}}-1\right)} \quad (3.52)$$

Equation (3.50) can now be rewritten as:

$$\Delta' a = -\frac{\pi}{8}\gamma^{5/4}\tau_H^{1/2}\tau_\eta^{3/4}\frac{4}{\Gamma(3/2)\left(\lambda^{\frac{3}{2}}-1\right)} \quad (3.53)$$

$$\Rightarrow -\frac{2}{\pi}\Gamma(3/2)\,\Delta' a\gamma^{-5/4}\tau_H^{-1/2}\tau_\eta^{-3/4} = \frac{1}{\left(\lambda^{\frac{3}{2}}-1\right)} \quad (3.54)$$

Using the definition $\lambda = \gamma\tau_H^{2/3}\tau_\eta^{1/3}$ the above equation is further simplified as follows:

$$\Rightarrow -\frac{2}{\pi}\Gamma(3/2)\,\Delta' a(\lambda^{-5/4}/\tau_H^{-5/6}\tau_\eta^{-5/12})\tau_H^{-1/2}\tau_\eta^{-3/4} = \frac{1}{\left(\lambda^{\frac{3}{2}}-1\right)} \quad (3.55)$$

$$\Rightarrow -\frac{2}{\pi}\,\Gamma(3/2)\Delta' a\tau_H^{1/3}\tau_\eta^{-1/3} = \frac{\lambda^{5/4}}{\left(\lambda^{\frac{3}{2}}-1\right)} \quad (3.56)$$

Let consider $\lambda = 1-\varepsilon$, this gives:

$$\frac{\lambda^{\frac{5}{4}}}{\left(\lambda^{\frac{3}{2}}-1\right)} = -(1-\varepsilon)^{\frac{5}{4}}\left(1-(1-\varepsilon)^{\frac{3}{2}}\right)^{-1} \sim -\,(1-5\varepsilon/4)(3\varepsilon/2)^{-1}$$

$$= -\frac{(5\lambda - 1)}{4}\frac{2}{3(1-\lambda)} = -\frac{2}{3(1-\lambda)}$$

Hence, equation (3.56) can now be written as:

$$\Rightarrow -\frac{2}{\pi}\,\Gamma(3/2)\Delta' a \tau_H^{1/3}\tau_\eta^{-1/3} = -\frac{2}{3(1-\lambda)} \qquad (3.57)$$

By solving for γ after some simple manipulation, we finally obtain:

$$\gamma = \tau_H^{-2/3}\tau_\eta^{-1/3} - \quad 1.18(\Delta' a)^{-1}\,\tau_H^{-1} \qquad (3.58)$$

For $\Delta' \gg 1$, the second term can be neglected and we recover the well known scaling for the resistive kink mode, originally derived in Ref [123].

$$\gamma = \tau_H^{-2/3}\tau_\eta^{-1/3} \qquad (3.59)$$

Finally, the $\lambda \gg 1$ case corresponds to negative values of Δ', for which the tearing mode instability does not happen.

3.4. Initial Equilibrium Profiles and Δ' Calculations

The initial equilibrium that we have selected to study is defined as follows:

$$\psi_0(x) = \frac{1}{\cosh^2(x)} \qquad (3.60)$$

$$\phi_0(x) = 0 \qquad (3.61)$$

This means that the plasma is considered to have no initial flow. The analytical expressions for the corresponding magnetic field and current density are listed below.

$$B_{0y}(x) = \left(\frac{\partial \psi_0}{\partial x}\right) = -2\,\mathrm{sech}^2(x)\,\tanh(\mathrm{x}) \qquad (3.62)$$

$$\mathrm{J}_{0z}(x) = \left(\frac{\partial^2 \psi_0}{\partial x^2}\right) = 2\,\mathrm{sech}^4(x)\,[\cosh(2x) - 2] \qquad (3.63)$$

The equilibrium profiles of $\psi_0(x)$, $B_{0y}(x)$ and $J_{0z}(x)$ are plotted in Figure 3.1. This equilibrium is unstable to tearing mode only at the resonant surface $x = 0$ and hence produces only one tearing layer inside the simulation domain.

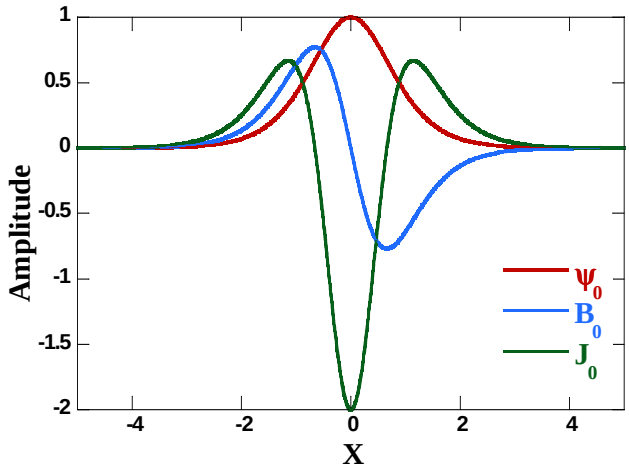

Figure 3.1: The equilibrium profiles of magnetic flux, field and electrict current.

We now calculate the instability parameter Δ' as defined by equation (3.15). For this purpose, equation (3.12) has to be solved for the perturbation flux ψ_1. Note that such analysis is basically the same as briefly reported in [121], however, we here provide more details and also discuss the case of generalized equilibrium as given in Appendix B.

For the sake of convenience, we repeat the equation (3.12):

$$\psi_1''(x) - \left(k_y^2 + \frac{\mathrm{J}_0'}{\mathrm{B}_{0y}}\right)\psi_1(x) = 0 \tag{3.64}$$

Applying the initial equilibrium (Equation (3.60)) into the above equation, we obtain:

$$\psi_1''(x) - \left(k_y^2 + \frac{8\,\mathrm{sech}^5(x)\sinh(x)[3-\cosh^3(x)]}{-2\,\mathrm{sech}^2(x)\,\tanh(x)}\right)\psi_1(x) = 0 \tag{3.65}$$

Simplifying the above equation results in:

$$\psi_1''(x) - \left(k_1^2 - \frac{12}{\cosh^2(x)}\right)\psi_1(x) = 0 \tag{3.66}$$

Here, $k_1^2 = k_y^2 + 4$, and $k_y = 2\pi m/l_y$. Note that here m represents the poloidal mode number and l_y is the length of the simulation domain in the y-axis).

Let introduce the following transformation:

$$z = \cosh^{-2}(x)$$

$$\psi_1(x) = \psi_1(z) z^{-\frac{k_1}{2}}.$$

Equation (3.66) is transformed into the Gauss' hyper-geometric equation:

$$z(1-z)\psi_1'' + \left[(1-k_1) - \left(\frac{3}{2} - k_1\right) z\right] \psi_1' - \left(\frac{k_1^2}{4} - \frac{k_1}{4} - 3\right) \psi_1 = 0 \qquad (3.67)$$

The solution of this equation can be expressed in terms of the Gauss hyper-geometric functions [124].

$$\psi_1(z) = C_1 F\left(-\frac{3}{2} - \frac{k_1}{2}, 2 - \frac{k_1}{2}, 1 - k_1, z\right)$$

$$+ C_2 z^{k_1} F\left(-\frac{3}{2} + \frac{k_1}{2}, 2 + \frac{k_1}{2}, 1 + k_1, z\right) \qquad (3.68)$$

The solution can be expressed in terms of the original variable $\psi_1(x)$ as follows:

$$\psi_1(x) = C_1 \cosh^{k_1}(x) F\left(-\frac{3}{2} - \frac{k_1}{2}, 2 - \frac{k_1}{2}, 1 - k_1, \cosh^{-2}(x)\right)$$

$$+ C_2 \cosh^{-k_1}(x) F\left(-\frac{3}{2} + \frac{k_1}{2}, 2 + \frac{k_1}{2}, 1 + k_1, \cosh^{-2}(x)\right) \qquad (3.69)$$

To get the solution for large *x*, we set $C_1 = 0$ and $C_2 = 1$, we obtain:

$$\psi_1(x) = \cosh^{-k_1}(x) F\left(-\frac{3}{2} + \frac{k_1}{2}, 2 + \frac{k_1}{2}, 1 + k_1, \cosh^{-2}(x)\right) \qquad (3.70)$$

It is now straight forward to estimate the instability parameter Δ' using its definition (equation (3.15)). Details of the complete derivation for two generalized equilibrium profiles are given in Appendix B.

$$\Delta' = \frac{\psi_1'(0+) - \psi_1'(0-)}{\psi_1(0)} = 2\frac{\psi_1'(0+)}{\psi_1(0)} \qquad (3.71)$$

Where, we have used the fact that $\psi_1(x)$ is an even function. After some manipulation, finally we obtain the relation for Δ':

$$\Delta' = 2\left[\frac{6k_1^2 - 9}{k_1(k_1^2 - 4)} - k_1\right] \tag{3.72}$$

For the tearing mode to be unstable $\Delta' > 0$, which implies that $k_1^2 \leq 9$ or $k \leq \sqrt{5}$. In the limit of $k \ll 1$, an asymptotic expression can be derived for Δ':

$$\Delta' \approx \frac{15}{k^2} \tag{3.73}$$

Let remind the reader that throughout this thesis, Δ' is modified by changing the domain size in the y-direction i.e. L_y.

3.5. Simulation Setup

We next implement the reduced magneto-hydrodynamics (RMHD) model to describe the evolution of nonlinear tearing mode in slab geometry with $\boldsymbol{B}=B_{0z}\boldsymbol{e_z}+\boldsymbol{e_z}\times\boldsymbol{\nabla}\psi_0$. Here $\boldsymbol{e_z}$ is unit vector of the strong guide magnetic field B_{0z}. The total magnetic flux function ψ and the stream function ϕ in the plane perpendicular to the guide field are given as follows:

$$\partial_t\psi = -[\phi,\psi] + \eta\nabla^2\psi\,, \tag{3.74}$$

$$\partial_t(\nabla^2\phi) = -[\phi,\nabla^2\phi] + [\psi,\nabla^2\psi] + \mu\nabla^2(\nabla^2\phi). \tag{3.75}$$

Note that here, the Poisson bracket is defined as $[A,\ B] = \partial_x A\partial_y B - \partial_y A\partial_x B$. The lengths are normalized by the scale length of the equilibrium field a and the time is normalized by the Alfvén time, $\tau_A = a\ /\ v_A$, where v_A is Alfvén velocity defined as $v_A = B_{0z}/\sqrt{4\pi\rho_0}$. The magnetic field is normalized by the guide field B_{0z}. The equilibrium configuration employed in these simulations is represented by $\psi_0\ (x) = 1/\cosh^2(x)$ and $\phi_0 = 0$.

Equations (1) and (2) are solved as an initial value problem. A spectral code using Fourier decomposition along *y* direction with simulation domain $[0, 2\pi L_y\ ]$ is applied, namely,

$$\tilde{f}(x,y,t) \sim \frac{1}{2}\left\{\tilde{f}(x,y)exp\left(imy/L_y\right) + c.c\right\}, \tag{3.76}$$

where, *m* is the mode number in *y* direction and *c.c* stands for the complex conjugate of the corresponding field. In this study, we usually fix the mode numbers of the order $m\sim50$. However, we also confirm the numerical resolution of the simulations even with higher

number of poloidal modes. Here the wave number is defined as $k_y = m/L_y$. A second order finite difference method is employed in the *x* direction with a box size of $[-5, 5]$ and mesh number of 2048. A semi-implicit Crank-Nicolson numerical scheme is implemented to solve the equations in the radial direction. Note that the control parameters in simulations are the instability parameter Δ', the plasma resistivity η and the viscosity μ. Note that the value of Δ' is varied by changing the wave number k_y using the equation (3.72).

3.6. Linear Simulation Results

In this section, we report the linear analysis of the resistive tearing mode via computer simulation of the two field resistive RMHD equations (3.74) and (3.75). Although, the main focus of this thesis is the investigation of nonlinear evolution phase of the tearing mode, however, it may useful to first benchmark our code by validating the FKR theory. The key parameters in the simulation are Δ' and η. The effect of finitely large viscosity is not considered here and will be included in the coming chapters.

Before starting the linear analysis of the tearing mode, it is important to define the linear growth rate γ_{lin}. In the simulations, we calculate the mean square perturbation electrostatic potential $(E_k = \langle \tilde{\phi}^2 \rangle/2)$ and mean square perturbation magnetic potential $E_m = \langle \tilde{\psi}^2 \rangle/2$, where $\tilde{\phi}$ and $\tilde{\psi}$ are the perturbation electrostatic potential and perturbation magnetic flux respectively. Note that the symbol $\langle\ \rangle$ represents the space averaged quantities. Since the magnetic flux and kinetic flow are Fourier transformed along y-axis, therefore, more precisely we can express the mean square perturbation quantities as follows:

$$E_k = \sum_m \tilde{\phi}_m^2/2, \tag{3.77}$$

$$E_m = \sum_m \tilde{\psi}_m^2/2, \tag{3.78}$$

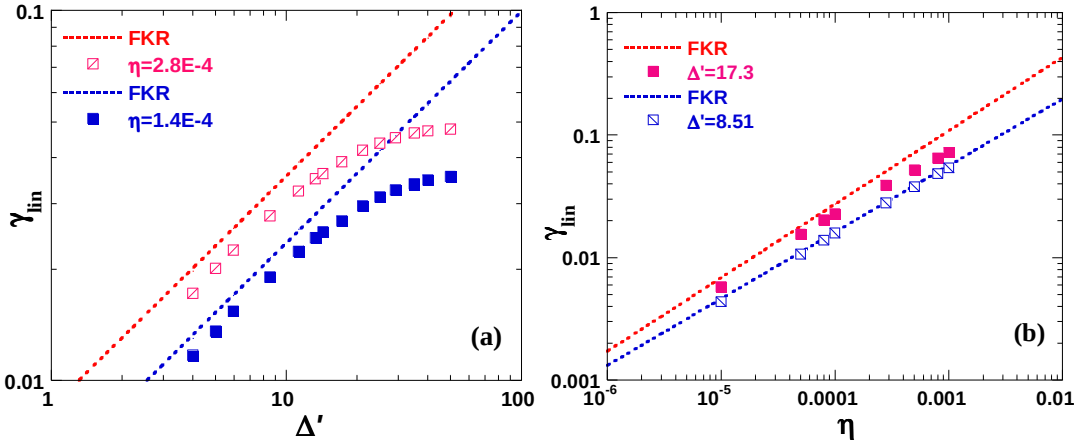

Figure 3.2: Scaling of the linear grwoth rate verses (a) instability parameter Δ' for two cases of resistivities, and verses (b) resistivity η for two fixed values of Δ'. The dashed lines, represents the theoritical scalings of the linear growth rate as predicted by FRK.

where, $\sum_m$ is the summation of the contributions from all the poloidal harmonics. In the linear regime of tearing instability, the perturbation flow and magnetic flux grow exponentially, i.e. $\tilde{\phi}, \tilde{\psi} \sim \exp(\gamma_{lin} t)$. Note that the linear growth rate of the mean square electrostatic potential and magnetic potential is two times the linear growth rate of the perturbation flow and flux. In this thesis, we will mostly plot the mean square perturbation potentials to describe the time evolution of the tearing mode. To describe the nonlinear evolution, we will later define the nonlinear instantaneous growth rate γ.

The dependence of the linear growth rates of the tearing mode on Δ' and η is depicted in Figure 3.2. In Figure 3.2(a), we plot the linear growth rate verses the Δ', for two different resistivities. The dashed lines show the FKR theoretical growth rate for each resistivity. It is evident that the simulation results are in good agreement with the FKR theory for low enough values of Δ' and not only reproduce the correct slopes but also the actual values of the growth rate predicted by the theory for small enough η. The deviation from the FKR theory is caused by large η or large Δ'. This is because at large η, the resistive layer width increases and can become comparable to the plasma scale length. In such situation, the resistive dissipation becomes important in the whole regime and thus

the assumptions, on which the theory is based, are no longer valid. Similarly, the growth rate scaling with η as shown in Figure 3.2 (b) deviates from the theory by larger extent at larger Δ'. This is because of the fact that at large enough Δ', the constant-ψ approximation is not valid.

3.7. Summary

In this chapter, we reviewed the classical resistive tearing mode theory. A systematic derivation of the FKR theory is performed both for the case of constant-ψ as well as non-constant-ψ. In both the cases, the plasma domain is divided into the inner resistive layer and outer ideal layer. The inner region solution is then matched with the outer layer solution, obtaining the FKR relation. Then, we introduce the equilibrium profiles used in this study and derive the instability parameter for it. After the analytical description, we introduce the simulation model for solving the RMHD system and elaborate the relevant numerical schemes. Finally, we present a comparison of the linear simulation results with the FKR theory to benchmark our simulation code. In particular, we illustrate the dependence of the linear growth rates of the tearing mode on the instability parameter Δ' and plasma resistivity η. The simulation results are found to be in good agreement with the theory in the regime of Δ' and small enough η. The linear growth rate scaling deviated from the theory by larger extent at larger Δ', because at large enough Δ', the constant-ψ approximation is not valid.

Chapter 4

Abrupt Growth Dynamics of Nonlinear Resistive Tearing Mode and Viscosity Effects

4.1. Introduction

The nonlinear evolution of the resistive tearing mode exhibits an abrupt growth for large enough values of the instability parameter Δ', once the magnetic island exceeds a certain critical width $\Delta' w_c$. Actually, the transition from slow growth phase to the faster phase is accompanied by change of X-point magnetic flux configuration at the rational surface into Y-type current sheet [63-67]. In this work, we investigate the underlying mechanism of the X-point collapse, which leads to the faster current sheet instability phase. To achieve this goal, we suggest a secondary instability, based on the quasilinear modification of the equilibrium current profile due to the zonal current. It is noteworthy that this analysis is similar to the secondary instability analysis in the case of DTM [51]; however, the driving force for the secondary instability is different. The zonal current is found to modify the equilibrium current profile in two ways, peaking at the rational surface and broadening in the outer region. Thus, we explore the effects of such zonal current peaking and broadening through the secondary instability analysis, separately. The secondary instability analysis is also performed for the cases of finitely large viscosity.

Another key objective of this study is to clarify the role of viscosity in the transition from the slow Rutherford regime to the abrupt reconnection phase during the non-linear evolution of the resistive tearing instability. Since critical island width is a signature for the onset of abrupt reconnection phase, therefore, it may be useful to analyze the dependence of the critical island width for the X-point collapse on the viscosity. Though, previously

the scaling of critical island width had been analyzed [67], however, the effect of finite viscosity was not included in that work. Generally, the viscosity plays a dissipation role in the MHD fluctuations while the resistivity determines the singular layer dynamics of the tearing mode. It is noteworthy that viscosity is not always weak as compared to the resistivity in laboratory and astrophysical plasmas because micro-scale turbulence can enhance the viscosity [68-70]. The turbulent viscosity is usually larger than the collisional value and depends on the temperature and magnetic field. Hence, the magnetic Prandtl number $P_r = \mu/\eta$ is of the order of $P_r = 200T^3/B^2$, which shows a strong dependence of temperature. For a typical magnetic fusion plasma with $B = 4Tesla$ and $T = 2keV$, P_r is of the order of 100. Therefore, it is worthwhile to examine the role of finitely large viscosity in the evolution of resistive tearing instability.

The content of this chapter (adopted mostly from Ref [125]) is organized as follows: First, we introduce a typical simulation result, depicting the abrupt nonlinear evolution of the resistive tearing mode. The zonal modification of the equilibrium current profile is delineated for a typical case and the basic quantities involved in the analysis are defined. The effects of current peaking at the rational surface and current broadening in the outer region are separately investigated, both for resistive and viscous cases through secondary instability analysis. After the investigation of the trigger mechanism of the X-point collapse, we analyze the effects of viscosity on the linear growths of the tearing mode in a broad viscosity range. It is followed by the scaling analysis of critical island width through nonlinear simulations, including the viscosity effects. Finally, the effects of viscosity on the abrupt reconnection are examined by measuring the reconnected flux during the abrupt reconnection phase after the X-point collapse.

4.2. Nonlinear Tearing Mode Evolution for Different Δ'

Nonlinear simulations are performed for different values of the resistivity η and the instability parameter Δ'. It is observed that for low Δ', the mean square electrostatic potential ($E_k = \langle\tilde{\phi}^2\rangle/2$) and mean square magnetic potential ($E_m = \langle\tilde{\psi}^2\rangle/2$), after the linear FKR region, grow slowly in the Rutherford's nonlinear growth phase [52, 53]. Actually, for such low values of Δ', the magnetic island finally stops growing further and

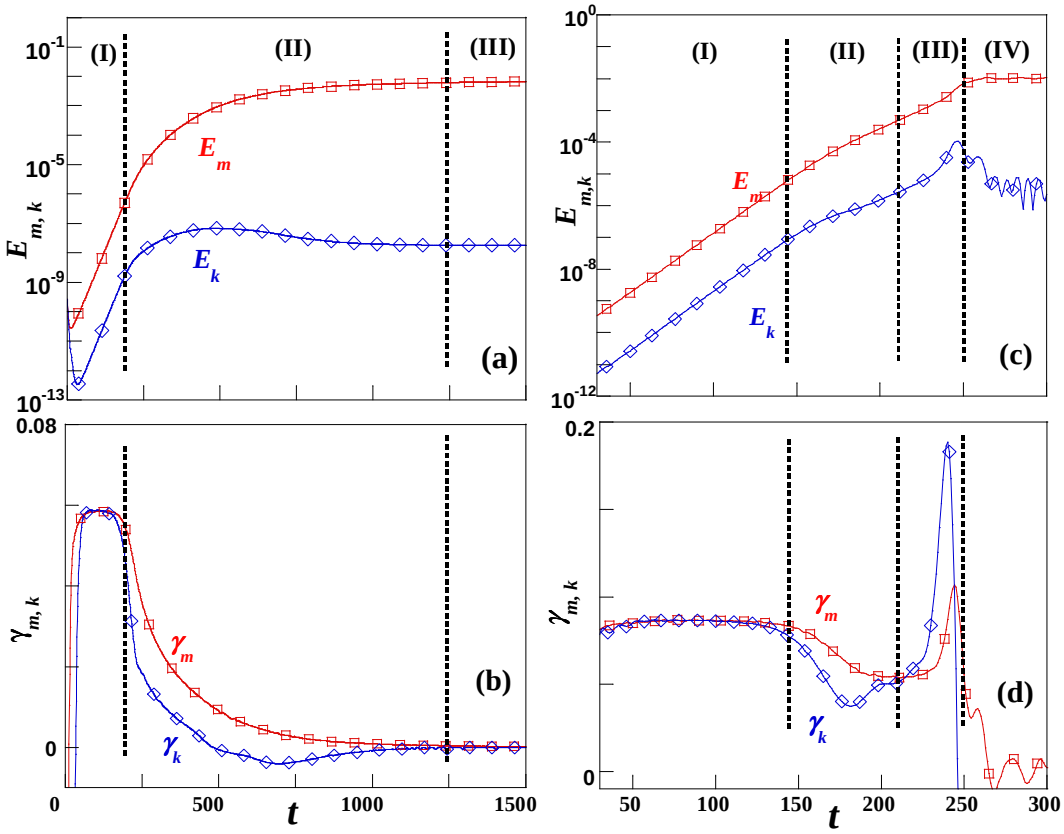

Figure 4.1: Time history of the mean square electrostatic and magnetic potential E_k and E_m (a) and their instantaneous growth rates for $\Delta' = 9.32$ (b) Time history of E_k and E_m for the case $\Delta' = 24.5$ (c) and their instantaneous growth rates (d). Other parameters are $\eta = 2.8 \times 10^{-4}$ and $\mu = 0$.

gets saturated. These different stages of the tearing mode evolution are depicted in the Figure 4.1 (a) for a case of low Δ'. After the linear stage (I), the evolution goes through the slow Rutherford stage (II) and finally the island is saturated (III). The dynamics of the perturbation quantities is more evident by plotting their instantaneous growth rates, defined by $\gamma_{k,m} = \partial_t(\ln E_{k,m})$, as shown in Figure 4.1(b). However for sufficiently large Δ', the evolution of magnetic island does not saturate and the perturbation quantities grow again after the slow Rutherford regime. This situation is shown in Figure 4.1 (c) and (d) for the case of large Δ'. The time of abrupt nonlinear destabilization is defined as the critical

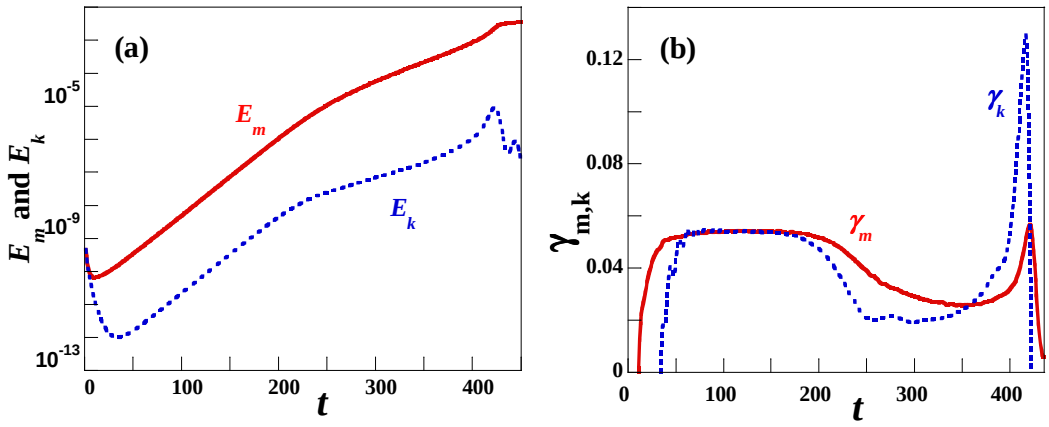

Figure 4.2: Time history of the mean square electrostatic potential E_k and mean square magnetic potentail E_m (a) and their instantaneous growth rates (b). Parameters are: $\Delta' = 17.3$, $\eta = 1.4 \times 10^{-4}$ and $\mu = 0$.

time t_{kc}, at which $\partial_t(\gamma_k) = 0$. This time actually corresponds to the point of inflection in the evolution of kinetic energy. It is noteworthy that after this critical time, the mean square perturbation potential grows again and can achieve higher growth rate than the linear growths for sufficiently low values of η, as shown in Figure 4.1(d).

4.3. The Abrupt Nonlinear Growth Phase and X-point Collapse

In order to explicate the nonlinear dynamics of the resistive tearing mode in the regime of large Δ', we consider a typical simulation case of smaller resistivity $\eta = 1.4 \times 10^{-4}$, where the instantaneous growth rate, defined as $\gamma_{k,m} = \partial_t(\ln E_{k,m})$, increases again after the slow nonlinear evolution as depicted in Figure 4.2. To further strengthen our understanding of the actual dynamics, we plot the magnetic flux contours at different times in the nonlinear evolution stage. It is observed that at the critical time t_{mc}, at which $\partial_t(\gamma_m) = 0$, the X-point configuration collapses to a current sheet as depicted in Figure 4.3. The narrow current sheet then leads to the secondary island generation at the previous X-point. This change of configuration along the rational surface, leads to a dynamical change in the magnetic reconnection process. In this chapter we only focus on such transition phase from the slow nonlinear growth (the X-point configuration) to the

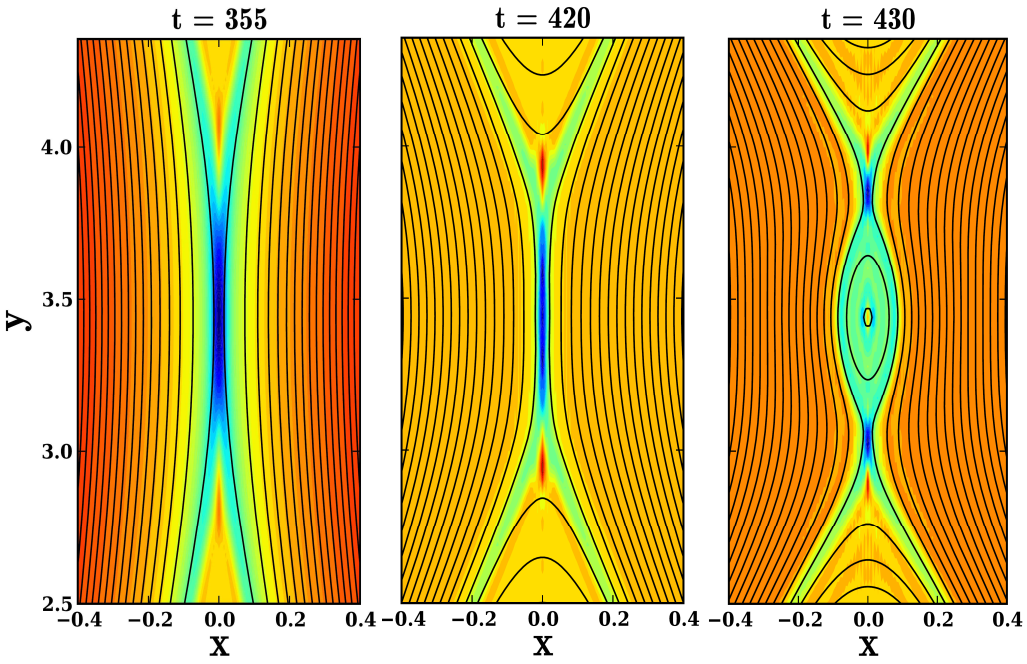

Figure 4.3: 2D contour plots of the current, merged with the magnetic flux lines, during the nonlinear evolution of Figure. 4.2.

faster reconnection (Y-type current sheet). The island width corresponding to the X-point collapse is defined as the critical island width, w_c, which is a precursor to enter the explosive nonlinear growth stage. Although, this instability has recently been rigorously investigated, however, the driving mechanism for the X-point collapse is still a less understood problem. Thus, it is worthwhile to clarify the trigger mechanism of the X-point collapse, resulting in the formation of secondary narrow current sheet which leads to the abrupt growth phase.

4.4. Secondary Instability Analysis for Inviscid Case

Although, the abrupt nonlinear growth of the mean square perturbations in both classical and double tearing modes is quite analogous to each other in feature, however the magnetic flux configuration is quite different. In the case of DTM, the formation of triangular structure of the magnetic island was identified to be responsible for triggering the explosive dynamics [50, 51]. On the other hand, the single tearing mode in the regime of

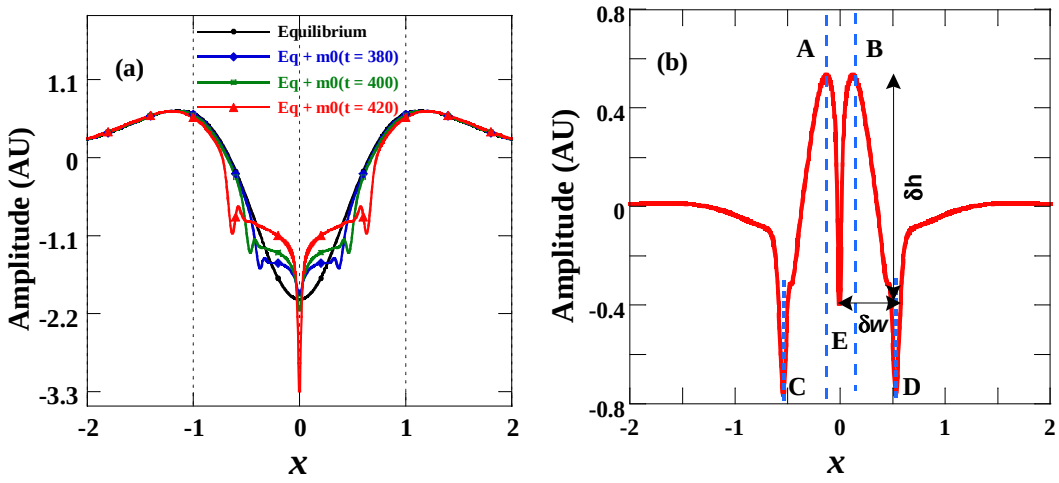

Figure 4.4: (a) Current profiles modified by the zonal current at different times during the nonlinear evolution in the simulation of Figure 4.1. (b)The structure of zonal current at time t = 410. The pairs of inner and outer dashed lines label the local peaking and global broadening regions, respectively.

large Δ', is characterized by a current sheet formation along the single resonant surface following the X-point collapse [63-67]. We here propose a secondary instability, which originates from the quasilinear modification of the equilibrium current profile by the zonal perturbation current, to analyze the X-point collapse. It's noteworthy that such zonal current perturbations results from the nonlinear coupling of the poloidal modes. We perform the secondary instability analysis for the inviscid and viscous cases separately to get clear understanding of the results.

First, we consider the case of resistive tearing mode in the inviscid limit ($\mu = 0$). In general, the equilibrium profile gets flattened in the early Rutherford's regime as depicted in Figure 4.4(a) and this actually leads to the stabilization of the growth rate. However, at the critical times $t_{kc,mc}$ (after the Rutherford regime), the equilibrium current is mainly modified in the inner region. These modifications are caused by the generation of the zonal current. The profile of zonal component of the perturbation current is plotted in Figure 4.4(b) at a given time in the evolution of Figure 4.2. The dashed lines mark the inner and

outer region corresponding to the peaking and broadening effects respectively. It is speculated that such a current modification may enhance the magnetic island width and plasma flow if it can destabilize the tearing mode. To verify such an idea, we implement a secondary instability analysis by assuming a quasi-steady equilibrium state involving the zonal current. Thus the new equilibrium is composed of two parts, the initial current at time t=0 and the zonal current at the time t=t_0 during the explosive nonlinear growth phase, which can be expressed as,

$$\psi_E(x,y,t) = \psi_0(x,t=0) + \psi_{m=0}(x,t=t_0)\,, \tag{4.1}$$

$$J_E(x,y{:}\,t) = J_0(x,t=0) + J_{m=0}(x,t=t_0)\quad . \tag{4.2}$$

The RMHD equations are modified with the new equilibrium and are rewritten here for the sake of convenience.

$$\partial_t\psi = -[\phi,\psi_E] + \eta\nabla^2\psi \tag{4.3}$$

$$\partial_t\nabla^2\phi\ = -[\psi_E,\nabla^2\psi] + [\psi,\nabla^2\psi_E]\ + \mu\nabla^2(\nabla^2\phi) \tag{4.4}$$

We perform linear simulations through the RMHD equations (4.3) and (4.4), involving the instantaneous modifications of the equilibrium profile by the zonal current at different times during the nonlinear evolution. The growth rates of the mean square linear perturbations $\gamma_s = \partial_t(\ln E_k) = \partial_t(\ln E_m)$ of the most unstable m=1 component in the secondary instability analysis are the same as the instantaneous growth rates $\gamma_{k,m}$ in the linear phase of the primary tearing mode since the zonal current is too weak as described in Figure 4.5. Note that, γ_s should be twice the linear growth rate of the perturbations in usual instability analysis, in which the latter one is defined by the perturbation itself. In the Rutherford regime, the secondary growth rate tends to decrease but be higher than $\gamma_{k,m}$, showing that except for the quasilinear stabilization due to current profile relaxation, the nonlinear mechanisms such as the mode coupling may also stabilize the primary tearing mode. However, γ_s starts to increase from the critical time t_{kc}. This increasing tendency suggests that the current modification due to the zonal current can excite a secondary instability to provide a positive destabilization feedback for the abrupt nonlinear growth. The secondary instability may trigger the X-point collapse around t_{mc} and then enhance the current sheet formation. In order to verify such a working hypothesis, we examine the effect of local and global modification due to the zonal current.

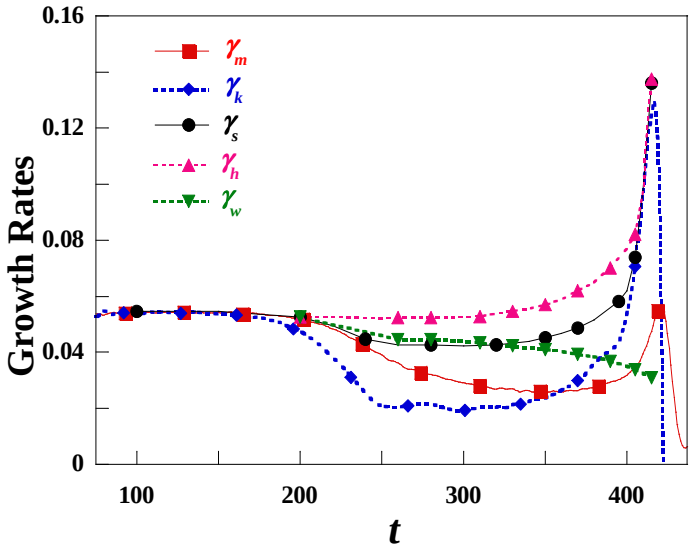

Figure 4.5: Time history of the secondary growth rates of perturbation energy due to zonal current, current peaking and current broadening (represented by γ_s, γ_h and γ_w respectively) along with the growth rates of the mean square electrostatic and magnetic potential (γ_m and γ_k). The simulatoin parameters are the same as in Figure 4.2.

4.4.1. Secondary Instability due to Current Peaking and Broadening

As shown in Figure 4.4(a), the initial equilibrium current profile is mainly modified in two ways: locally peaked near the resonant surface and globally broadened in the outer region far from the resistive layer. Both of these effects get stronger with time during the nonlinear evolution. We separately consider the effects of current peaking and broadening on the secondary instability. The peaking height δh and broadening width δw are defined through the structure of the zonal current component as the difference of the amplitude between points A and E (or B and E) and the projection in the *x* direction between points A and C (or B and D), respectively, as depicted in Figure 4.4(b). Using this methodology, we estimate the secondary growth rates γ_h and γ_w of the perturbation energy due to the zonal current peaking and broadening effects separately. The results are compared in Figure 4.5. The current peaking effect destabilizes the secondary excitation of the fluctuations, while the current broadening plays a stabilizing role. At the late stage of the explosive growing

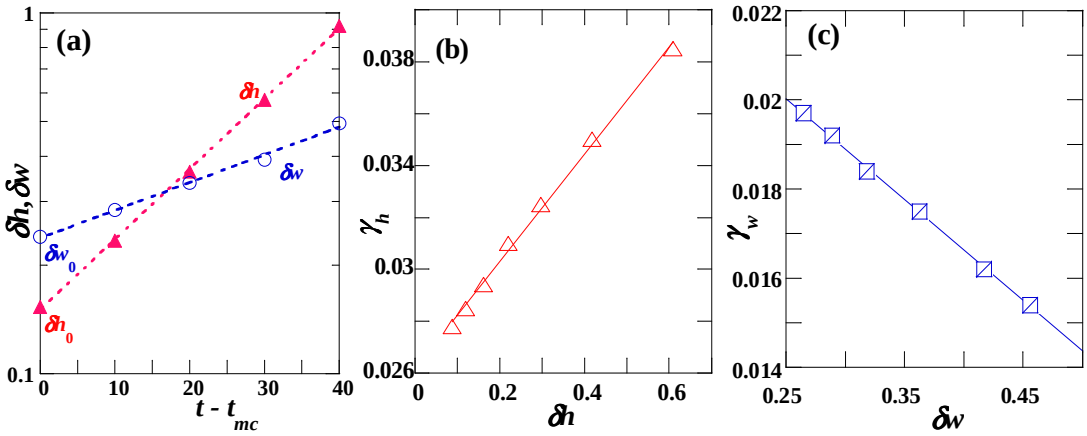

Figure 4.6: Secondary growth rates (a) due to the current peaking versus the peaking height (b) and broadening width verses the broadening width. Parameters are $\Delta' = 17.3$, $\eta = 2.8 \times 10^{-4}$ and $\mu = 0$.

phase, the secondary growth rate γ_h due to the current peaking effect tends to be compatible with γ_k, showing that the peaking effect of zonal current may be plausibly responsible for the explosive dynamics.

To further elucidate the current peaking and broadening effects, Figure 4.6(a) plots the instantaneous values of the peaking height δh and the broadening width δw of the current profile corresponding to different times in the nonlinear evolution. The fitted dashed lines indicate the exponential growth of both the current peaking height and broadening width in time, which can be expressed as:

$$\delta h \sim \exp\big(\alpha_h (t - t_{mc})\big), \tag{4.3}$$

$$\delta w \sim \exp\big(\alpha_w (t - t_{mc})\big). \tag{4.4}$$

The dependence of secondary growth rates on the peaking height δh and broadening width δw is depicted in Figure 4.6(b) and 4.6(c). A proportional relation is revealed for both current peaking height and broadening width as

$$\gamma_h \sim \beta_h \, (\delta h - \delta h_0), \tag{4.5}$$

$$\gamma_w \sim \beta_w \, (\delta \mathrm{w} - \delta \mathrm{w}_0). \tag{4.6}$$

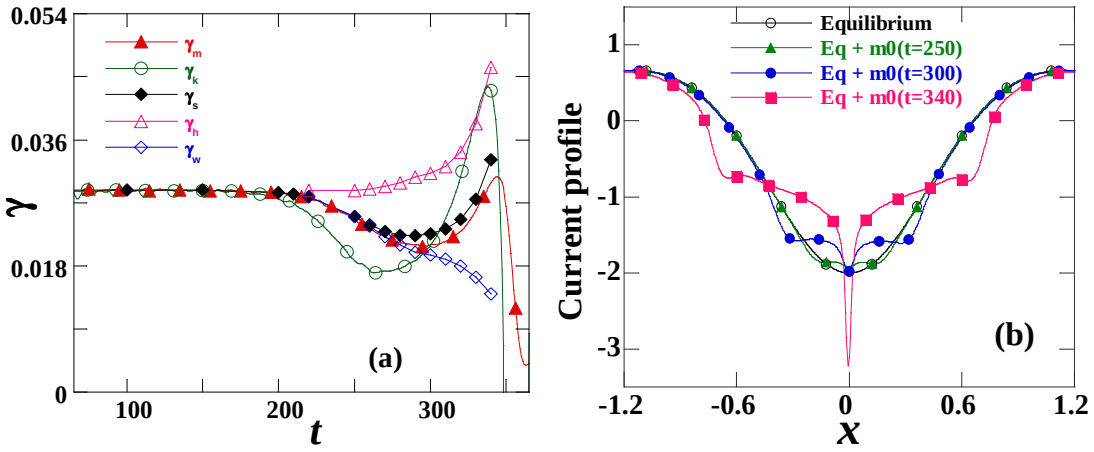

Figure 4.7: Time evolution of the (a) secondary growth rates due to the zonal current modifications and (b) the zonal current modification of the equilibium current profiles. The simulation parameters are $\Delta' = 17.3$, $\eta = \mu = 2.8 \times 10^{-4}$.

Here $\beta_h > 0$ and $\beta_w < 0$, which represent the destabilizing role of the current peaking and the stabilizing role of the current broadening effects, respectively. Here δh_0 and δw_0 correspond to the critical peaking height and broadening width at the X-point collapse, as marked in Figure 4.6(a). Hence, the secondary instability due to the current peaking effect may trigger the X-point collapse. Equations (4.3) and (4.5) combinedly exhibit a much faster growth of the tearing mode fluctuations than the exponential evolution, namely, exponential of exponential growth as follows:

$$\psi_s, \phi_s \sim \exp(\beta_h \exp(\alpha_h t)) \ . \tag{4.7}$$

This suggests that the current peaking effect may be plausibly responsible for driving the explosive dynamics of the nonlinear tearing mode by exciting a secondary instability, which may cause a fast magnetic reconnection. Note that here the secondary fluctuations are of the same mode features as the primary tearing instability due to the quasilinearly modified current peaking effect. Interestingly, the linear properties of the system can be embodied in the nonlinear dynamics through the secondary instability analysis. It is probably such secondary instability that triggers the X-point collapse and the positive feedback effect of the

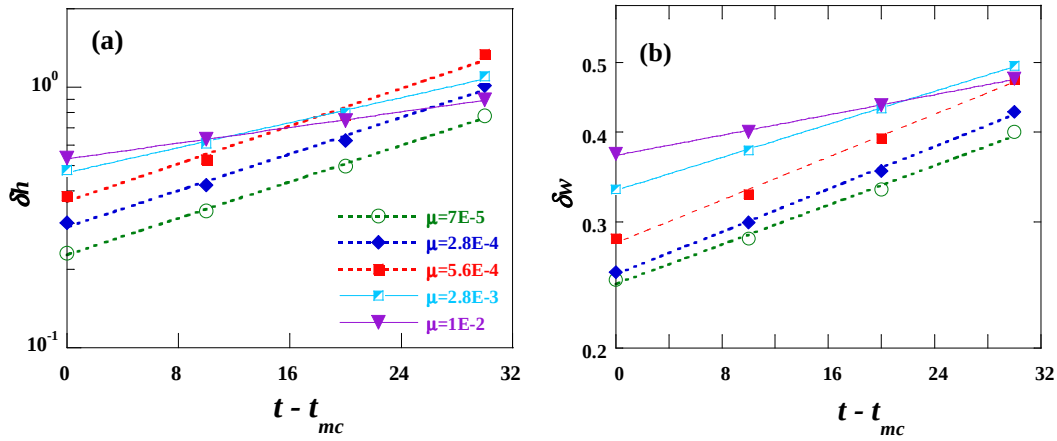

Figure 4.8: Time evolution of (a) current peaking height and (b) broadening width for different values of viscosity. $\Delta' = 17.3$, $\eta = 2.8 \times 10^{-4}$.

same secondary fluctuation that nonlinearly gives rise to a current sheet formation, namely explosive growth dynamics.

4.5. Secondary Instability Analysis for Viscous Case

Next, we perform the secondary instability analysis including the finitely large viscosity. It is important to consider the effects of viscosity on the evolution of the tearing mode instability, since viscosity is not always smaller than the resistivity. Usually, viscosity plays a stabilizing role, reducing the outflows and increasing the current sheet width of the resistive tearing mode. Thus, it may be worthwhile to consider the effects of viscosity on the X-point collapse, which triggers the faster nonlinear reconnection stage. First, we describe a typical nonlinear simulation case of $P_r = 1$, with $\eta = \mu = 4.8 \times 10^{-4}$, as depicted in Figure 4.7. The instantaneous growth rates of the mean square perturbed magnetic potential and electrostatic potential show the similar explosive nature in nonlinear growth phase as observed in the resistive case. Furthermore, the peak growth rate of the magnetic potential grows higher than the linear phase. The secondary instability analysis results are also plotted in Figure 4.7 (a). In general, the secondary instability analysis results follow the same tendency as observed in the inviscid case in Figure 4.5. In the explosive growth phase, the secondary growth rate due to the zonal current peaking

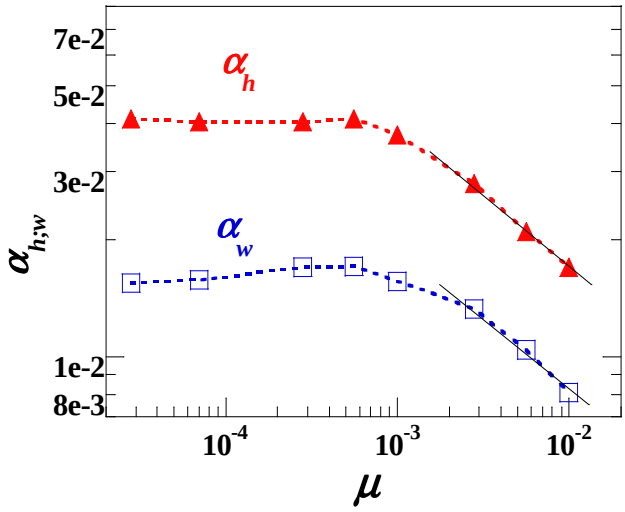

Figure 4.9: Growth rates of the peaking height and broadening width versus viscosity. The dashed and solid lines are for reference. $\Delta' = 17.3$ and $\eta = 2.8 \times 10^{-4}$.

matches the nonlinear perturbation growth rate. Thus the zonal current peaking may act as trigger for the onset of the explosive growth dynamics. The modification of the equilibrium current due to the zonal current is shown in Figure 4.7 (b) for some selected times during the nonlinear evolution and is compared with the initial equilibrium profile.

Next, we scan the zonal current modification effects in a broad range of viscosity $\mu = 0.0$ to 0.001 at fixed values of $\eta = 4.8 \times 10^{-4}$ and $\Delta' = 17.3$. The nonlinear simulation results reveal that similar to the inviscid case, the instantaneous peaking height δh and broadening width δw in the explosive growth phase grow exponentially, as shown in Figure 4.8(a) and 4.8(b). It is noticed that the current peaking height and broadening width at the time of X-point collapse, defined as δh_0 and δw_0 respectively, increase with the viscosity at the critical time t_{mc}. This tendency may result from the viscosity effect since at the onset of the X-point collapse, larger current peaking is required to compensate the viscous dissipation and then drive the secondary instability. The growth rates α_h and α_w of both δh and δw roughly remain constant for weak viscosity. However, both growth rates decrease as the viscosity increases in larger P_r region with the same scaling, as explicitly depicted in Figure 4.9 showing a transition of the viscosity dependence around $P_r \gtrsim 1$.

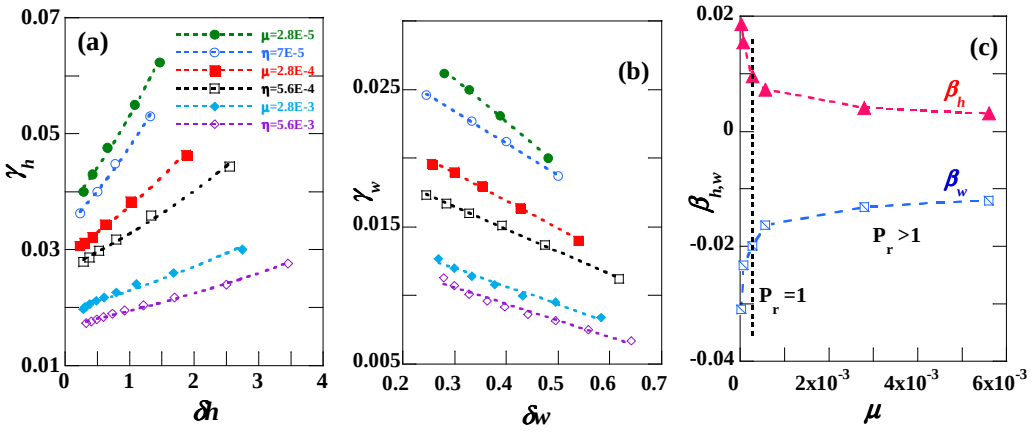

Figure 4.10: Secondary growth rate versus the peaking height(a) and the broadening width(b) for different viscosity. (c) Proportional factors of the peaking height and broadening width against viscosity. $\Delta' = 17.3$ and $\eta = 2.8 \times 10^{-4}$.

To inspect separately the effects of the local current peaking and global current broadening on the secondary instability including the viscous effects, we perform secondary instability analysis for the same simulation settings as that of Figure 4.9. The results show that local current peaking effect remarkably destabilizes the secondary tearing mode, while the global broadening effect plays a strong stabilizing role, as illustrated in Figure 4.10. It is observed that the growth rates of the secondary instability are proportional to the peaking height and inversely to broadening width. The combination of these two dependences can lead to fluctuation evolution as ψ_s, $\phi_s \sim \exp\left(\beta_{h,w} \exp\left(\alpha_{h,w} t\right)\right)$. Identical to the $P_r = 0$ case, the current peaking can possibly drive the explosive (i.e., exponential of exponential) growth of the secondary instability, which may cause the abrupt growth of the reconnection rate. However, the dependence of the secondary growth rate on both the current peaking and broadening becomes weaker as the viscosity increases. This tendency is represented by the proportional factor $\beta_{h,w}$ versus the viscosity, as shown in Figure 4.10(c), for $\Delta' = 17.3$ and $\eta = 2.8\text{E} - 4$. Remarkably, the magnitudes of $\beta_{h,w}$ decrease quickly in the region of $P_r < 1$ while they decrease slightly for $P_r > 1$, showing a transition of the viscosity dependence. Furthermore, the secondary growth rates get reduced with increasing viscosity at the same evolution phase, exhibiting a stabilizing effect of the viscosity. Comparisons

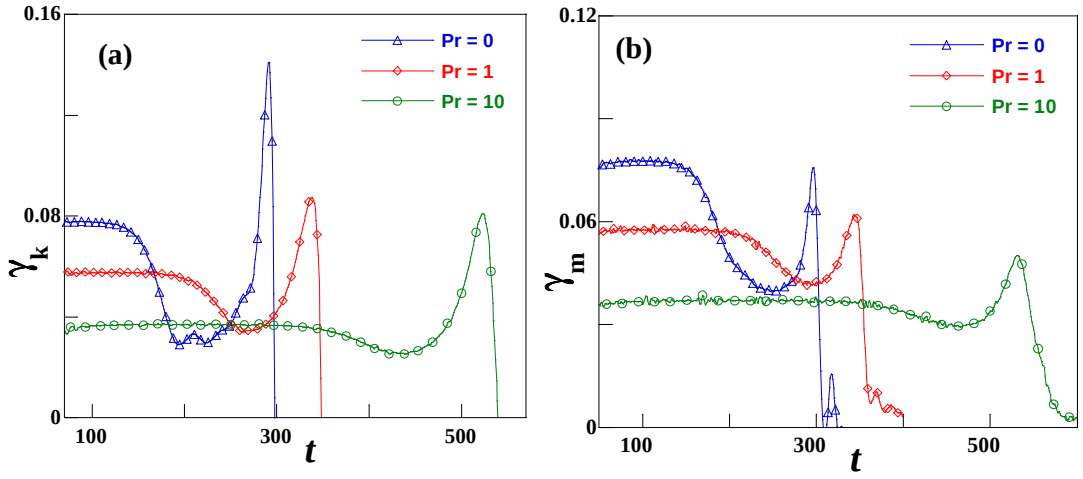

Figure 4.11: Time history of the instantaneous growth rates of (a) the mean square electrostatic potential, γ_k and (b) the mean square mangetic potentail, γ_m. The simulation parameters are: $\Delta' = 17.3$, $\eta = 2.8 \times 10^{-4}$, $\mu = 0$, 2.8×10^{-4} and 2.8×10^{-3} corresponding to $P_r = 0, 1$ and 10 respectively.

with the nonlinear growth rate of the instantaneous δh and δw (Figure 4.8) may imply that the explosive growth of the tearing mode is a purely nonlinear process in nature although the quasilinear secondary instability may provide a plausible trigger mechanism.

Next, we examine the effect of viscosity on the X-point collapse more directly through nonlinear simulations and explore the role of viscosity on the critical widths of the magnetic island for the X-point collapse.

4.6. The Effect of Viscosity on the Tearing Mode Evolution

Before scanning the parametric dependence of viscosity on the tearing mode evolution, we would like to quickly overview its effects on the stability of linear as well as nonlinear evolution of the tearing mode. Generally, the viscosity plays a dissipation role in the resistive tearing mode evolution while the resistivity determines the singular layer dynamics of the tearing mode. The magnetic Prandtl number $P_r = \mu/\eta$ can be as high as of the order of 100 for typical parameters of the fusion device due to the microturbulence

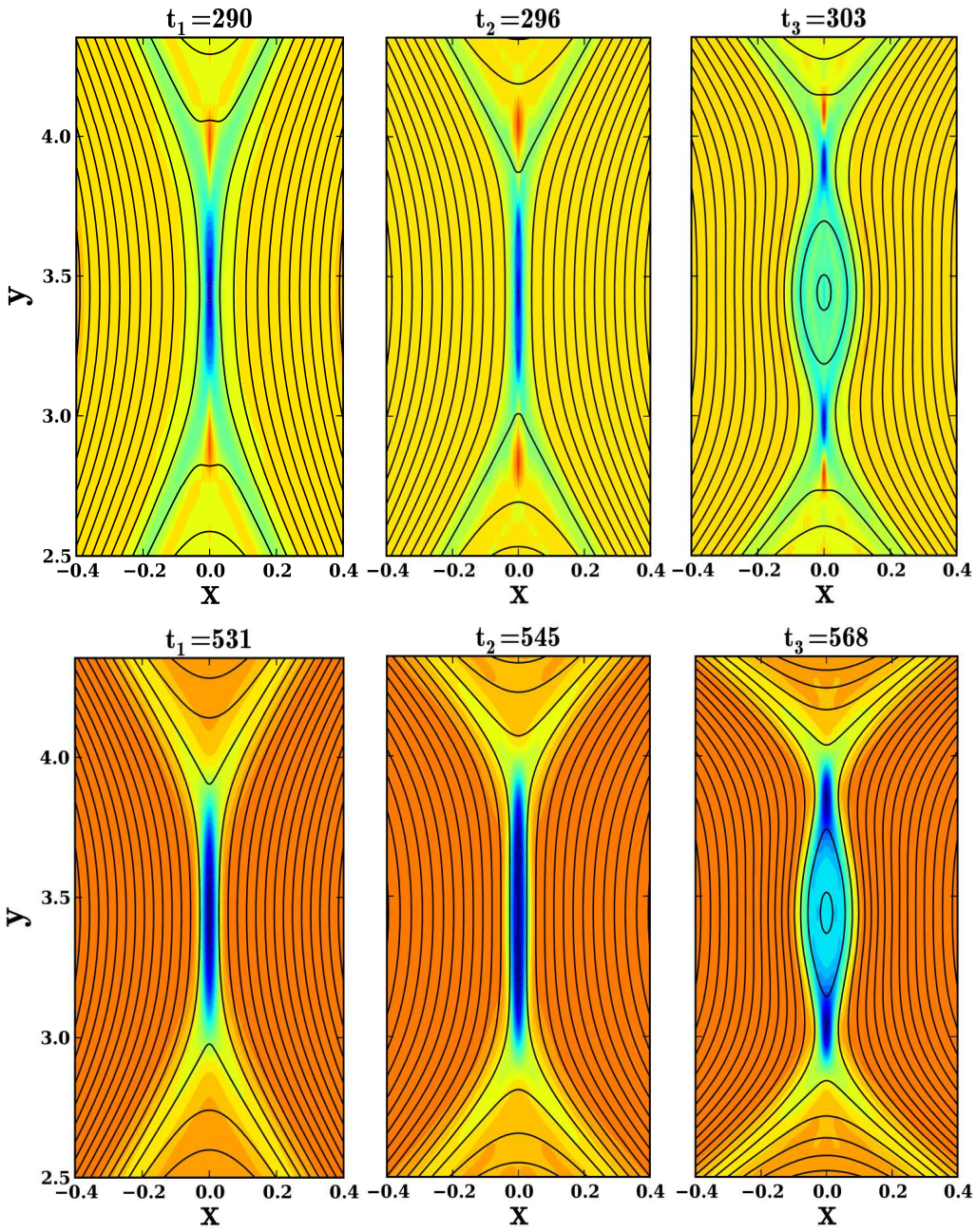

Figure 4.12: 2D contour plots of the current, merged with the magnetic flux lines, during the nonlinear evolution of Figure. 4.11. The upper panel represents the case of $P_r = 0$ and lower panel $P_r = 10$.

effects. In the limit of low Δ', the usual tearing scaling of the growth rate $\gamma \sim \eta^{3/5}$ is modified in the case of finite viscosity and scales as $\gamma \sim \eta^{2/3} P_r{}^{-1/6}$, which was termed as

the visco-tearing mode [71]. On the other hand, in the limit of $\Delta' \to \infty$, the growth rate scales as $\gamma \sim \eta^{1/3} P_r^{-1/3}$ and is known as the visco-resistive kink mode. Thus, viscosity can significantly affect the linear stability of the resistive tearing instability. However, the impact of viscosity on nonlinear dynamics of the tearing mode is still poorly understood.

To have an overview of the linear stabilization as well as nonlinear effects of finitely large values of viscosity, we perform nonlinear simulations at $\Delta' = 17.3$ and $\eta = 2.8\text{E} - 4$ for different values of viscosity, corresponding to $P_r = 0, 1$ and 10 as depicted in Figure 4.11. In the linear stage, the growth rate is significantly reduced as we increase the viscosity. This linear stabilization also delays the onset of the abrupt nonlinear growth phase after the slow Rutherford regime. This implies that viscosity may play an important role in the onset criteria for the abrupt reconnection phase, which will be discussed later in detail. Comparing the instantaneous growth rates of the perturbation potentials, it is seems that viscosity may reduce the reconnection rate in the abrupt growth phase after the X-point collapse. However, the ratio of the peak nonlinear growth rate to the linear growth rate seems to be enhanced with the viscosity.

The effect of viscosity has been investigated in a previous study in the case of slowly evolving current sheet, which concluded that it increases the current sheet width and slows the outflows [126]. This means that by including large viscosity, the current sheet will remain stable for longer time compared to the inviscid case, until it becomes thin enough to be unstable to the secondary island formation. To confirm this understanding, we plot the contours of the current sheet merged with the magnetic flux lines at different times in the nonlinear evolution of the tearing mode, as depicted in Figure 4.12. For the sake of comparison, we plot the current sheets at similar stages of the nonlinear evolution for the inviscid ($P_r = 0$) and viscous ($P_r = 10$) cases. The times t_1 represent the time at which the perturbed potential attains peak value, t_2 is the time at which the current sheet aspect ratio is maximum just before the formation of the secondary island and t_3 is the time after the secondary island formation. The comparison of the two cases, quite evidently reveals that the current sheet width is significantly increased by including large viscosity ($P_r \gg 1$). This implies that for large viscosity case, the secondary current sheet remains stable for longer time, which can be clearly observed for the viscous case (lower panel), where the

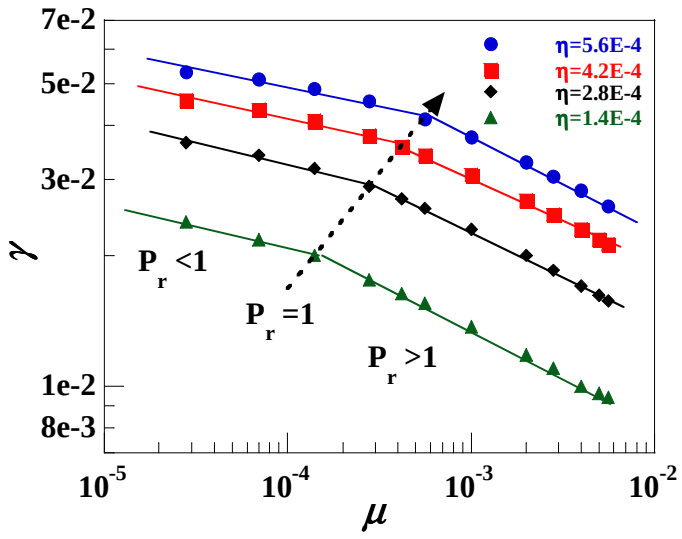

Figure 4.13: Linear growth rates versus viscosity for four different resistivity cases and $\Delta' = 17.3$. The dashed line with arrow labels the $P_r = 1$ for reference.

secondary island is generated much later after the magnetic potential peak. Meanwhile, the current sheet length is also increases sufficiently, until it reaches the maximum length so that the critical aspect ratio of the current sheet for the collapse is achieved. Thus, finitely large viscosity may not only stabilize the linear tearing mode but also affect its nonlinear dynamics.

4.7. Viscosity Dependence of the Linear Growth Rates

Before elaborating the nonlinear features, first we briefly discuss the viscosity effect on the linear growth rate by performing a parametric scan with four different resistivity η and a broad range of viscosity μ (10^{-5} to 10^{-2}) for given instability parameter $\Delta' = 17.3$. The linear growth rates versus the viscosity for different η values are plotted in Figure 4.13. It is obvious that increasing the viscosity generally reduces the linear growth rates because of the viscous dissipation, which opposes the resistive destabilization [73]. However, the trend of viscosity dependence of the linear growth rates apparently shows a slight transition at $P_r = 1$. The growth rates for $P_r > 1$ decrease with the viscosity faster than

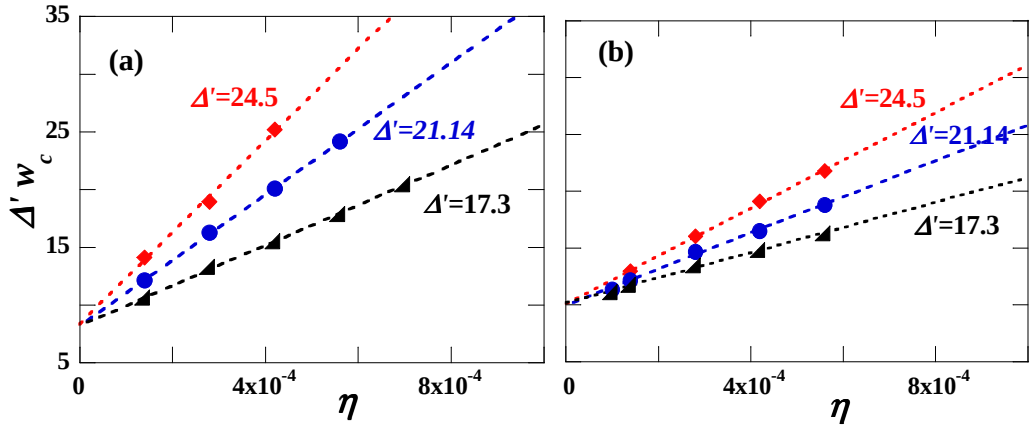

Figure 4.14: Critical island width $\Delta' w_c$ versus η, for different Δ'. (a) $\mu = 0$, (b) $\mu = 2.8 \times 10^{-3}$.

those in the region of $P_r < 1$, similar to the observation in Harris current sheet configuration [71]. Actually for $P_r > 1$, the resistive tearing mode becomes the visco-tearing mode and its growth rate scaling is estimated as $\gamma_{lin} \sim \mu^{-1/5}$, which is a bit different from the theoretical prediction of $\gamma_{lin} \sim \mu^{-1/6}$. However, the theory is valid for very small Δ' and high P_r.

4.8. Role of Viscosity in the Onset of X-Point Collapse

The critical island width for the X-point collapse is a precursor for the onset of the abrupt reconnection stage, which previously has been shown [67] to depend on the resistivity and the instability parameter Δ'. However, the effects of viscosity were not analyzed in such studies. Therefore, we comprehensively investigate the role of the viscosity in the onset of the X-point collapse and the abrupt nonlinear reconnection dynamics. As described in Sec. III (A), the X-point configuration collapses to a current sheet, which causes an abrupt increase in the growth rate of the perturbation energies when the island width exceeds a certain critical value w_c. We perform a systematic investigation of the viscosity dependence of the critical island width in terms of $\Delta' w_c$ in the limit of low η and large

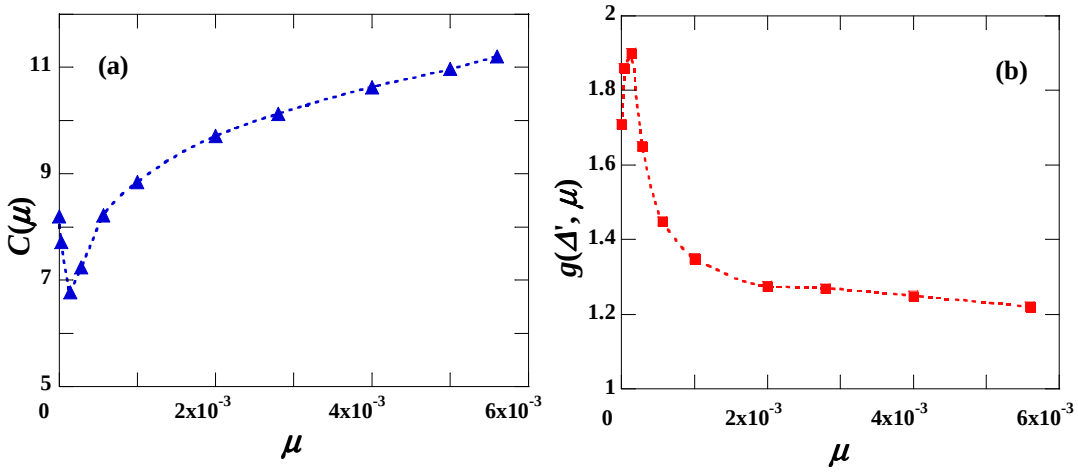

Figure 4.15: Factors $C(\mu)$ (a) and g(Δ', μ) (b) against the viscosity. $\Delta' = 17.3$.

enough $\Delta' = 17.3$. First, nonlinear simulations are performed by varying η and Δ' for the case of $P_r = 0$ to validate the previous scaling of the critical island width. The results are depicted in Figure 4.14(a), where $\Delta' w_c$ is plotted versus the resistivity for different values of Δ', showing a proportional dependence of the critical island width on the resistivity. In the limit of $\eta \to 0$, $\Delta' w_c$ converges to the same value of 8.2 for different values of Δ', thus verifying the scaling of Loureiro *et al.* [67]. Note that in this analysis, the island width is calculated numerically through the identification of the positions of X and O-points.

Next, we investigate the effect of viscosity on the critical island width $\Delta' w_c$. Nonlinear simulations are performed by including viscosity in a broad range (10^{-5} to 10^{-2}). Figure 4.14(b) depicts the scaling of critical island width $\Delta' w_c$ versus the resistivity η at constant value of viscosity $\mu = 2.8 \times 10^{-3}$ and three different values of Δ'. Comparison of Figures 4.14(a) and 4.14(b) suggests that viscosity modifies the scaling of critical island width mainly in two ways: reducing the slopes of $\Delta' w_c$ scaling and up-shifting the value of the critical island width in the limit of zero resistivity. It indicates that the viscosity plays an important role in determining the critical island width for the X-point collapse. We propose that the critical island width scaling gets modified in the presence of viscosity and can be expressed as:

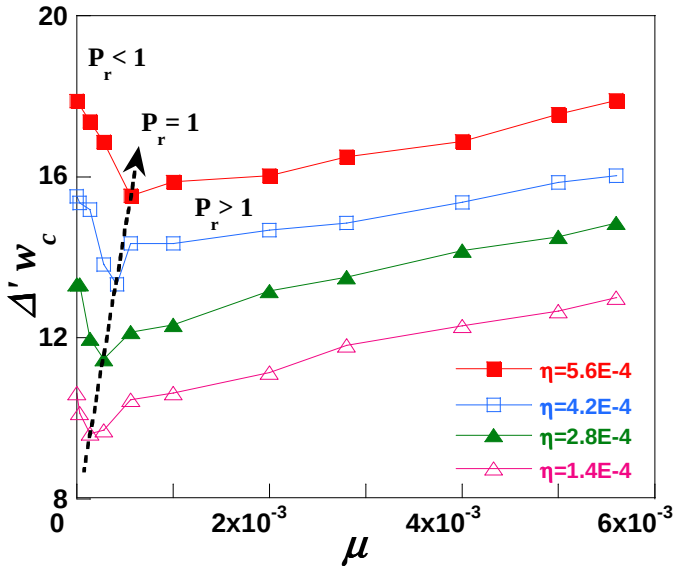

Figure 4.16: Critical island width $\Delta' w_c$ versus viscosity for four different resistivity cases. The dashed line with arrow labels $P_r = 1$ for reference. $\Delta' = 17.3$.

$$\Delta' w_c \approx C(\mu) + g(\Delta', \mu)\eta \,. \tag{4.8}$$

Here, C(μ) is the value of $\Delta' w_c$ in the limit of zero resistivity and it depends only on the viscosity. The slope of the scaling $g(\Delta', \mu)$ is not only the function of Δ' as observed previously by Loureiro *et-al*., [67] but also exhibit a strong dependence on μ. To further explain the viscosity dependence of the limiting value of critical island width $C(\mu)$ and the slope function $g(\Delta', \mu)$, we plot these two quantities against the viscosity in Figure 4.15(a) and 4.15(b). It is observed that in the limit of low viscosity, both the functions $C(\mu)$ and $g(\Delta', \mu)$ are more sensitive to the viscosity variation with a slight transition. On the other hand, C(μ) is linearly increasing but g(Δ′, μ) is slightly decreasing versus the viscosity for large enough values.

Viscosity dependence of the critical island width $\Delta' w_c$ for four cases with different resistivity and constant value of Δ' can be further exhibited in Figure 4.16. The results can be interpreted in terms of the magnetic Prandtl number P_r. We observe that $\Delta' w_c$ is inversely proportional to μ in the region of $P_r < 1$, whilst proportional for $P_r > 1$. An

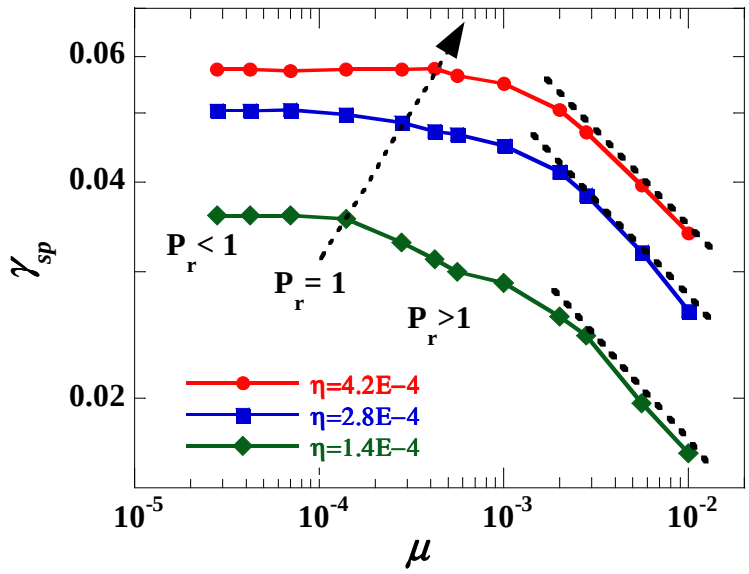

Figure 4.17: Growth rates of reconnected flux in the explosive growth phase versus viscosity for three different resistivity cases. The dashed line with arrow represents $P_r = 1$ and other dashes lines are for reference.

obvious scaling transition is revealed at $P_r = 1$. In the region of large viscosity ($P_r > 1$), the critical island width is increased almost linearly with the viscosity, since viscosity damps the inflows and outflows. However, the effect of viscosity in the $P_r < 1$ regime is not so obvious. It seems that the current sheet width is increased and the flow is reduced, but since the flux and flow are decoupled in this regime, there may an imbalance in the flux to flow ratio, which may reduce the critical island width for the X-point collapse. The results also show that for a given viscosity, the critical width $\Delta' w_c$ increases with the resistivity, which is in accordance with the new scaling (equation (4.8)).

4.9. Viscosity Effects on the Speed-up Reconnection Stage

Finally, it is interesting to extend our investigations on the viscosity effects to the abrupt reconnection stage after the X-point collapse. Note that Park *et al*. [126] predicted that the viscosity can modify the Sweet-Parker type reconnection, leading to a scaling of the

reconnection rate as $\dot{\psi}_s \sim \eta^{1/2} P_r^{-1/4}$ for $P_r \gg 1$, where $\dot{\psi}_s$ is the change rate of the magnetic flux at the X-point. To demonstrate the viscosity effects on the magnetic reconnection more clearly, we evaluate the scaling of the growth rate of reconnected flux, γ_{SP}, which is defined as $\psi_{rec} - \psi_{coll} = exp(\gamma_{SP}(t - t_{mc}))$. Here, ψ_{rec} is the reconnected flux, which is measured as the difference between the maximal and minimal fluxes through the X-point along the current sheet. ψ_{coll} is the reconnected flux at the critical time t_{mc}, which corresponds to the X-point collapse. For the case without viscosity, we confirm the Sweet-Parker scaling as $\gamma_{SP} \sim \eta^{1/2}$. However, the viscosity modifies it to deviate from the index of 1/2. Most importantly, it is observed that γ_{SP} is almost independent of the viscosity for $P_r < 1$ in a wide resistivity range, as shown in Figure 4.17. The value of the γ_{SP} moderately decreases around $P_r \sim 1$. However, the viscosity effect is prominent for $P_r \gg 1$, showing a scaling law as $\gamma_{SP} \sim \mu^{-1/4}$ in a wide resistivity range. Hence, similar to the linear growth rates and critical island width, γ_{SP} in the explosive growth phase also exhibits a transition behavior around $P_r \approx 1$.

4.10. Summary

We have performed a comprehensive investigation of the trigger mechanism for the onset of the X-point collapse and the drive force of the abrupt nonlinear growth of the resistive tearing mode for sufficiently large instability parameter Δ'. The X-point collapse occurs when the magnetic island exceeds a critical width $\Delta' w_c$ in the late Rutherford regime. Afterwards, the tearing mode grows explosively to form a current sheet, leading to fast magnetic reconnection. To explore the origin of such processes, a secondary instability analysis has been proposed, in which the zonal current quasilinearly modifies the equilibrium current profile. The peaking and broadening effects of the current profile due to the zonal current have further been examined. Secondary instability analyses show that the local current peaking due to the zonal current generation remarkably destabilizes the tearing mode in the inviscid limit. The combination of the secondary instability with the exponentially growing current peaking effect results in a positive nonlinear feedback to enhance the tearing mode fluctuations, suggesting a plausible mechanism responsible for the onset of X-point collapse and explosive nonlinear growth. Nonlinear simulations with a

parametric scan in a broad range of viscosity for fixed values of Δ' and η show that the zonal current peaking height δh and broadening width δw still grow exponentially in time in viscous tearing modes. The growth rates are found to be independent of the viscosity in low viscosity region corresponding to $P_r < 1$, while they decrease with increasing viscosity for $P_r > 1$, exhibiting a scaling transition around $P_r = 1$. On the other hand, the secondary instability due to the current peaking effect is weakened, but mainly in the region of $P_r < 1$, also showing a transition of the viscosity dependence around $P_r = 1$.

Furthermore, the viscosity effects on the nonlinear dynamics as well as the linear instability of the tearing mode have been inspected with a focus on the scaling transition versus the magnetic Prandtl number P_r. It is observed that the viscosity dependence of the linear resistive tearing mode instability is characterized by a scaling transition noticeably at $P_r = 1$. The linear growth rate for $P_r > 1$ decreases faster than that in the region of $P_r < 1$ as the viscosity increases. Most importantly, it is found that in the presence of finite viscosity, the critical island width for the X-point collapse is modified as expressed by $\Delta' w_c \approx C(\mu) + g(\Delta', \mu)\eta$. We found that the scaling of critical island width $\Delta' w_c$ versus the viscosity, exhibit a transition behavior at magnetic Prandtl number $P_r \approx 1$. However, the explosive growth seems to be independent of the viscosity in the $P_r < 1$ regime, while large viscosity plays a strong dissipative role.

Chapter 5

Impulsive Magnetic Reconnection with the Dynamic Flow Effects

5.1. Introduction

So far we have assumed the laminar tearing mode reconnection without any turbulence effects. However, the astrophysical and heliophysics environments where the reconnection occurs are usually turbulent because of the high Reynolds numbers. Since the turbulence occurs in various plasmas and can change the nonlinear processes, then it is essential and relevant to the real physical systems to investigate the impact of background small scale turbulence on the magnetic reconnection process. It is now well established that turbulence can enhance the reconnection process by generating the multiple reconnection sites along the current sheet [103-111]. In most of these studies the turbulence was introduced in the form of random noise. However, there is still no universal agreement on the role of added noise.

Besides the turbulence effects, shear flows may also play important role in the linear and nonlinear evolution of the magnetic island. Note that the shear flows can stabilize the resistive tearing mode and reduce the saturation island width [127]. Moreover, symmetric flows (potential) with radial even-parity can produce considerably higher stabilization effect compared to the antisymmetric ones. The flow shear at the rational surface can make the effective instability parameter Δ' more negative, playing a stabilizing role [128]. Recently, the shear flow effects have been considered in the case of plasmoid instability [129], which concluded that the effect of flow shear is negligible for fast growing modes in

the limit of high Lundquist number *S*. However, it became important at lower *S*, where the instantaneous growth rate of the perturbation flux was found to decay in time.

Instead of applying the turbulence forcing in the form of random noise or a static shear flow, it may be interesting to consider a dynamic turbulent flow with finite frequency, similar to ion temperature gradient (ITG) driven small scale turbulence in the tearing mode reconnection [112]. Such dynamic flows can be realized in magnetically confined fusion plasmas where the MHD activities such as the tearing mode and ITG driven drift wave coexist simultaneously. We consider both symmetric (even-parity) and anti-symmetric (odd-parity) dynamic flows, which commonly exist in real turbulent plasma environment. It is expected that the dynamic flows with different radial parity can not only affect the linear stability property of the resistive tearing mode, but most importantly may also contribute to the fast magnetic reconnection through the nonlinear interaction processes. It is expected that the background turbulence will facilitate the triggering of the plasmoid instability, leading to the fast reconnection. It will be interesting to explore how the dynamics of the plasmoids is affected with the flow features such as the radial parity and frequency of the dynamic turbulent flow. This chapter is thus devoted to the study of the tearing mode reconnection with the dynamic flow. The reconnection behavior is examined verses the dynamic flow properties, such as the radial parity, frequency and amplitude. The content of this chapter is mostly adopted from [125, 130].

The organization of this chapter is as follows: The modeling details as well as the definitions of key parameters are presented. Before starting the rigorous analysis, we introduce the typical simulation results, exhibiting the plasmoid-dominated fast reconnection. Dynamics of the multiple plasmoid is further explicated by plotting the 2D flux contours for several cases. The dependence of the plasmoids dynamics on the radial parity and frequency of the dynamic flow is explicated by the contour plots of the flux. Then, we present the linear stability analysis of the tearing mode with the dynamic flow. After that we comprehensively analyze the onset condition of the impulsive bursty reconnection as a function of the dynamic flow properties, such as radial parity, amplitude and frequency. The effective reconnection rate in the plasmoid-dominate fast reconnection phase is measured and scaling with resistivity is plotted.

5.2. Physical Model of the Dynamic Flow

In order to investigate the resistive tearing mode reconnection behavior with the background dynamic flow, we assume a dynamic flow ϕ^{DF}, similar to the electrostatic ITG eigenmode, which evolve independently and is represented as follows [112],

$$\phi^{DF}(t, x, k_y) = A\,\hat{\phi}^{(n)}(x) e^{-i\Omega t + ik_y^{DF} y}. \tag{5.1}$$

Where, A is the constant amplitude factor of the dynamic flow and $\hat{\phi}^{(n)}$ represents the radial eigen-function corresponding to the eigenfrequency Ω and the wave number k_y^{DF}. The eigen-function is expressed by the *n*th Hermite function, which determines the parity of the dynamic flow, whether odd/even, depending on the value of n odd/even. The independently evolving dynamic flow is included in the RMHD equations through Poisson brackets, i.e. $\phi = \phi^{MHD} + \phi^{DF}$, undergoing poloidal mode coupling with the perturbation flux and stream function. We here consider both symmetric (even-parity) and anti-symmetric (odd-parity) dynamic flows, which commonly exist in real turbulent plasma environment. It is expected that the dynamic flows with different radial parity can not only affect the linear stability property of the resistive tearing mode, but most importantly may also contribute to the fast magnetic reconnection through the nonlinear interaction processes. The radial profiles of dynamic flow with even- and odd-parity cases at a given time are depicted in Figure 5.1. The local flow shear (second derivate of the electrostatic potential) at the rational surface $x = 0$, is maximum for the radial even-parity flow and is zero for the radial odd-parity flow. This difference in the flow shear at the rational surface may play a key role in the linear and nonlinear evolution of the resistive tearing mode, which we will discuss further in later part of this chapter. In addition to the radial profile dependence, this flow has a dynamic behavior in time (having finite frequency), which is another key factor that can affect the tearing mode reconnection process.

The ultimate goal of this study is to determine the behavior of the resistive tearing mode reconnection during the impulsive nonlinear reconnection phase. For this purpose, we will explore the effective reconnection rate E_{eff} during the abrupt nonlinear growth phase of the tearing mode in six-dimensional parameter space, i.e. $E_{\text{eff}}(\eta, \mu, \text{parity}, k_y, A, \Omega)$. However, in this study we will investigate the impact of only four

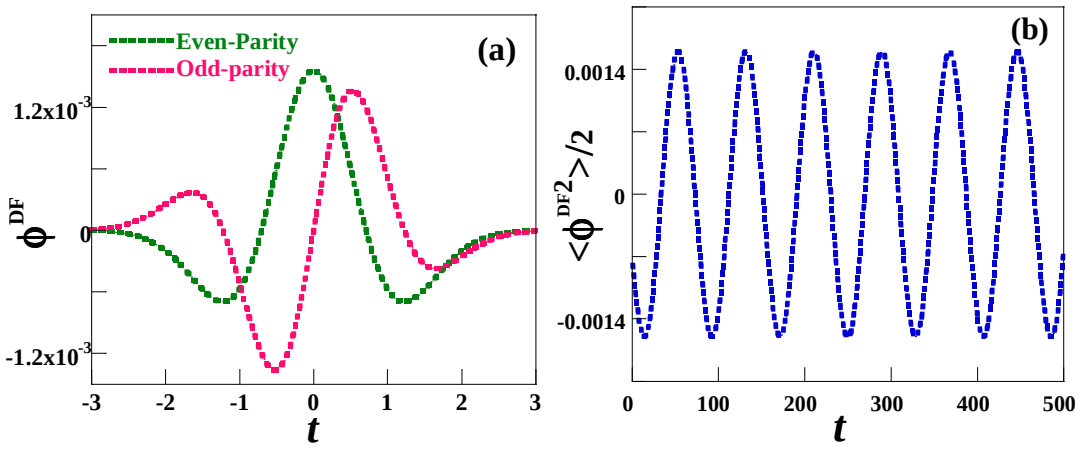

Figure 5.1: (a) Radial profiles of dynamic flow (ϕ^{DF}) at a given time for radial even- and odd-parity cases (b) Time evolution of the mean square dynamic flow at a fixed position $x = 0$. Simulation parameters are $\eta = 2.8 \times 10^{-4}$, $\Delta' = 17.3, and\ k_y^{DF} = 2.75$.

parameters η, $parity$, A and Ω. We assume a constant wave number $k_y^{DF} = 2.75$, set the amplitude of flow as $A = 10^{-10}$ to 10^{-3} and the frequency of flow in the range 0.02 to 2.0, based on the corresponding realistic frequency regime observed in the direct multiscale ITG and tearing mode simulations [112].

5.3. The Onset of Plasmoid Instability with the Dynamic Flow

We start our simulations from the case without the external dynamic flow. After the linear Furth-Killeen-Rosenbluth (FKR) growth phase [52], the magnetic island enters the slowly evolving Rutherford stage [53]. Note that for sufficiently large value Δ', the usual X-point configuration is replaced by secondary current sheet, leading to the formation of the secondary island [67, 125]. Similarly, for our selected instability parameter $\Delta' = 17.3$, the X-point collapses to a narrow current sheet, which finally results in a secondary island formation at the original X-point position. In order to analyze the effects of background dynamic flow on the magnetic island evolution, we compare the simulation results of the tearing mode in the cases with and without dynamic flow. The time history of mean square perturbations, i.e. mean square electrostatic potential ($E_k = < \tilde{\phi}^2 > /2$) and mean square

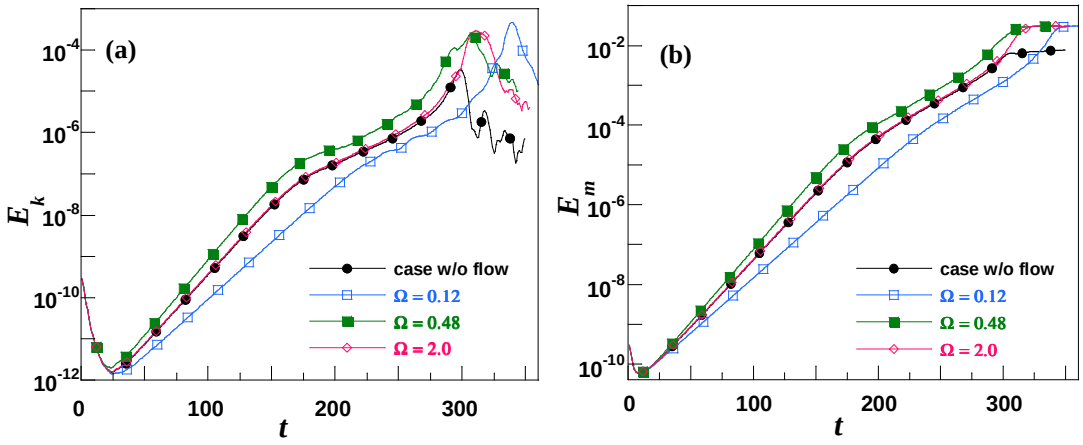

Figure 5.2: Time history of the mean square perturbed electrostatic potential $E_k = < \phi^2 > /2$ (a) and magnetic potential $E_m = < \psi^2 > /2$ (b) for the radial even-parity dynamic flows with different frequency. Simulation parameters are $\eta = 2.8 \times 10^{-4}$, $\Delta' = 17.3$, $k_y^{DF} = 2.75$ and $A = 8 \times 10^{-4}$.

magnetic potential $E_m = < \tilde{\psi}^2 > /2$, are plotted in Figure 5.2 for three different frequencies of the dynamic flow with radial even-parity (corresponding to the Hermite function of order $n = 2$). The linear stability of tearing mode is quite evidently affected by the dynamic flows with a strong dependence on the flow frequency. In the linear evolution phase, moderate stabilization is observed for low frequency $\Omega = 0.12$. However by increasing the flow frequency, the stabilization effect gets reduced and then a little destabilization effect is observed at higher frequency $\Omega = 0.48$, compared to the case without flow. Actually by increasing the flow frequency, the effective flow shear (which mainly reduces the linear growth rates of the tearing instability) gets reduced and this leads to the reduction in the linear stabilization impact of the flow. Finally, the growth rate of the tearing mode tends to approach to the case without flow at $\Omega = 2.0$.

The key objective of this study is to examine the effects of dynamic flow on the magnetic reconnection process of the resistive tearing modes. A common feature observed in the nonlinear evolution phase is that the nonlinear magnetic reconnection processes proceed in two phases: in the first phase, a narrow current sheet is generated with the SP scaling, and a plasmoid instability is triggered in the second phase where multiple

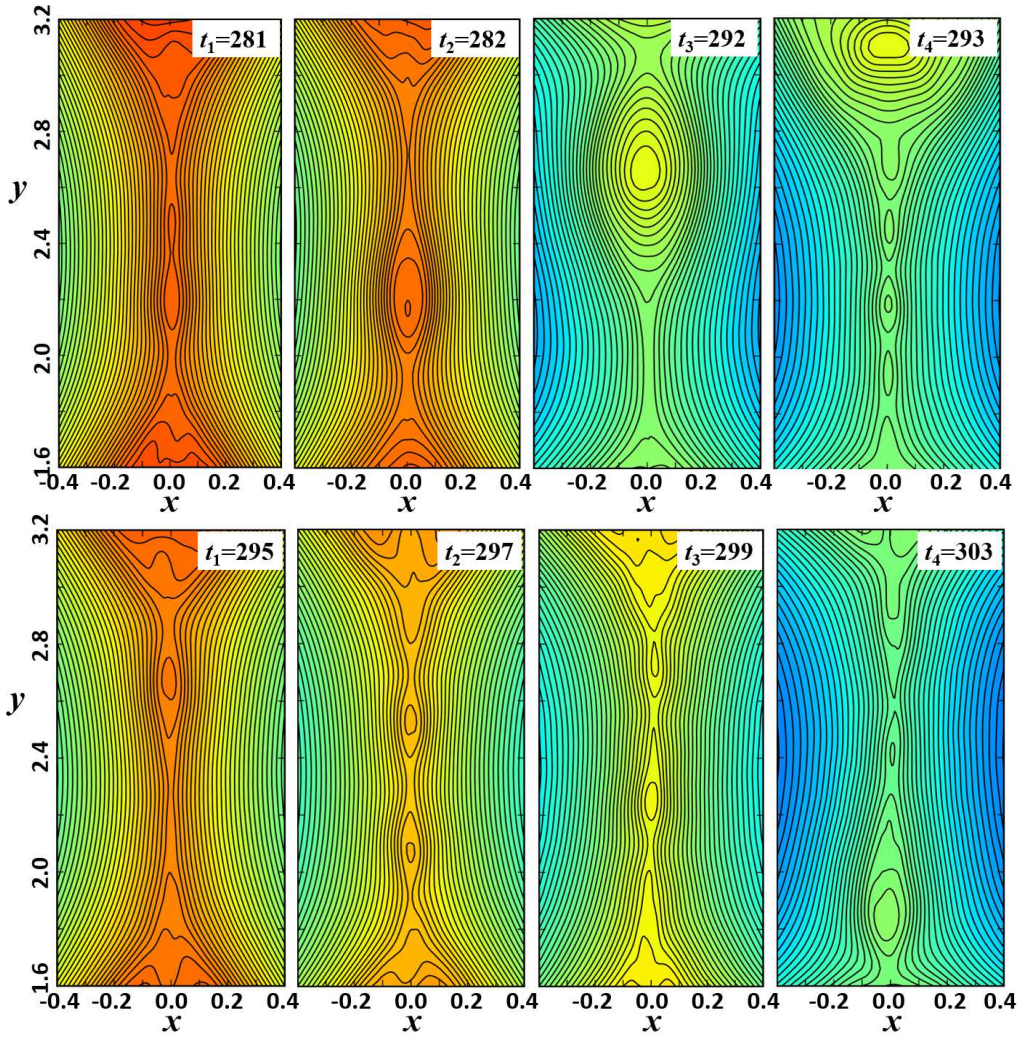

Figure 5.3: Contour plots of magnetic flux at different times in the simulations of Figure 5.2, with frequency $\Omega = 0.48$ (upper panel) and $\Omega = 2.0$ (lower panel), respectively.

plasmoids are continuously generated and ejected along the narrow current sheet, as depicted for the cases of $\Omega = 0.48$ (upper panel) and $\Omega = 2.0$ (lower panel) in Figure. 5.3. During the bursty reconnection phase, small plasmoids grow in size, coalesce with each other, occasionally form big monster plasmoids and eventually shift along the current sheet to merge with the primary island. Meanwhile, new plasmoids are being constantly generated and this process is repeated many times. From Figure 5.3, it is observed that the

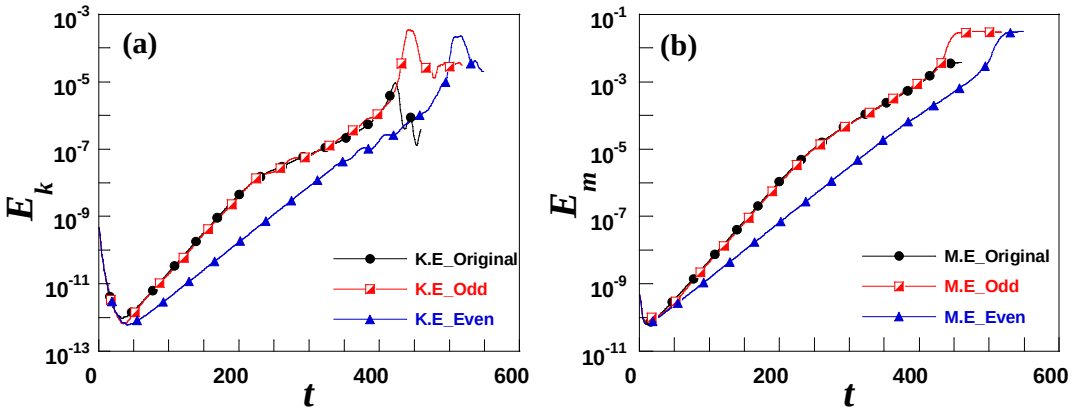

Figure 5.4: Time history of mean square perturbed electrostatic potential $E_k = < \phi^2 > /2$ (a) and magnetic potential $E_m = < \psi^2 > /2$ (b) for Even/Odd dynamic flows. The simulation parameters are $\eta = 1.4 \times 10^{-4}$, $A = 8 \times 10^{-4}$ and $\Omega = 0.08$.

direction of the plasmoids ejection depends on the frequency as well as radial parity of the dynamic flow. In the case of even-parity, the ejection direction alternates after the half period of the flow oscillation. Alternation of the direction of the plasmoids ejection tends to be fast as the flow frequency increases.

The impact of odd-parity flow on the linear and nonlinear evolution of the tearing mode is quite different from the even-parity flow case as depicted in Figure. 5.4. The linear growth rate is almost not affected. This is due to the fact that the flow shear at the rational surface is quite low (almost zero) in the odd-parity case. However, in the nonlinear evolution of the tearing instability, the odd-parity flow also leads to the plasmoid instability, similar to the case with even-parity flow. Comparison of the plasmoid evolution (contour plots of magnetic flux) during the impulsive reconnection phase for both even- and odd-parity flows is shown in Figure. 5.5. Due to small value of the flow frequency, we can see that plasmoids are ejected only in upward direction in the case of even-parity flow (upper panel). However, in the case of odd-parity, the flow has no effect on the direction of plasmoid ejection. This means the plasmoid will be ejected either in upward or downward direction, depending on its position where it is close to the upper or lower end of the current sheet. Interestingly, this behavior is somewhat consistent with previous simulation

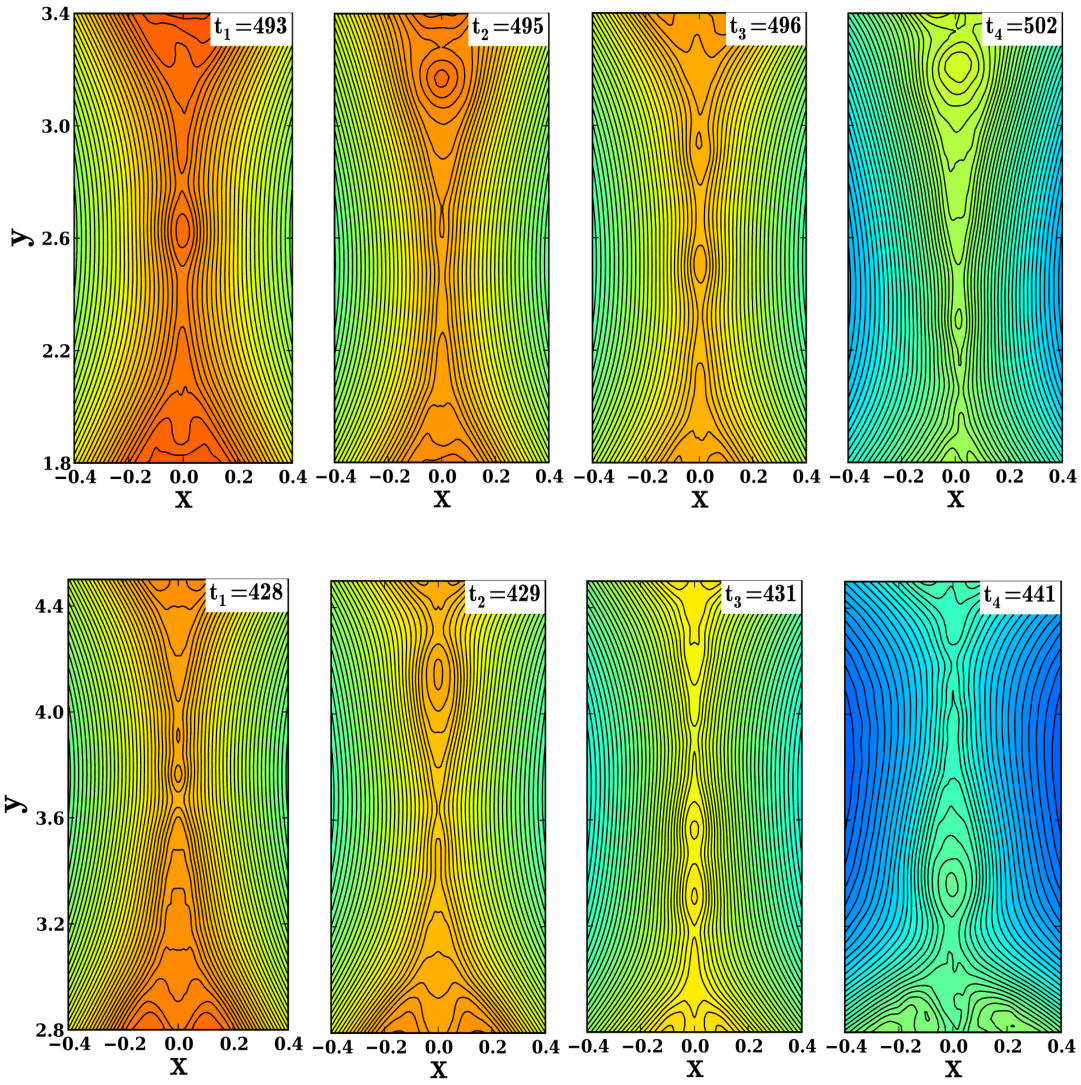

Figure 5.5: Contour plots of magnetic flux at different times in the nonlinear simulations of Figure 5.4, for even-parity (upper panel) and odd-parity flows (lower panel), respectively.

results [112], where the magnetic island showed an oscillatory behavior with even-parity flow but no effect in the case of odd-parity flow.

Another important feature of the plasmoid-dominated reconnection phase is the formation of monster plasmoid, which is a quite rare observation. Without the background turbulence, the plasmoids were observed to form in a statistical manner [81, 83]. They

have confirmed that in the linear growth phase, the plasmoids grow exponentially and then enter the complex nonlinear stage once the plasmoid width grows larger than the current sheet width. The plasmoids may be formed with different sizes and at different positions along the current sheet. The small plasmoids have short lifetime and are quickly coalesced with the bigger plasmoids. The monster plasmoids were occasionally observed with maximum width of $w_{max} = E_{\mathrm{eff}}^{1/2} L \sim 0.1L$, where E_{eff} and L are the effective reconnection rate and length of the secondary current sheet respectively. In this study, we observe quite similar behavior of the plasmoid instability, where initially small plasmoids are formed along the current sheet, which then coalesce with each other, forming larger plasmoids. In general, the monster plasmoid appears only if the secondary island is created at the center of the narrow secondary current sheet. Our observations suggest that monster plasmoids are generated, more probably in the case of even-parity flow with intermediate frequencies. The maximum size of the monster plasmoid can be roughly estimated as $w_{max} = E_{\mathrm{eff}}^{1/2} L \sim 0.164$, which is close to the observed value of $w_{max} \sim 0.17$, for the even-parity case of $\Omega \sim 0.48$ in Figure 5.3. Here the effective reconnection rate in the plasmoid dominated stage is $E_{\mathrm{eff}} \sim 0.027$ and the current sheet length $L \sim 1.0$. Thus, the plasmoid instability with the dynamic flow roughly follows the same tendency as observed in the previous cases without flows [81, 83]. In addition to the frequency and radial parity effect of the dynamic flow on the plasmoid dynamics, more importantly the critical condition for the plasmoid instability, i.e. $S \geq 10^4$, is relaxed.

The difference between even and odd-parity flows is further illustrated by plotting the full pictures of the flux contours as depicted in Figure 5.6. The primary magnetic island exhibits rotation in the case of even-parity flow with a frequency equal to that of the imposed dynamic flow. One complete cycle of the magnetic island oscillation is plotted from t=281 to t=293 (one time period is $\tau = 2\pi/\Omega \approx 13\tau_A$. The magnetic island rotation is evidently reversed after half of the time period of the flow oscillation. Such an oscillatory behavior of the magnetic island in case of even-parity dynamic flow may plausibly be responsible for the altering the plasmoid direction of plasmoid ejection along the current sheet. Actually, this kind of oscillations may come from the finitely large flow shear at the rational surface. This understanding is further substantiated by the fact that the

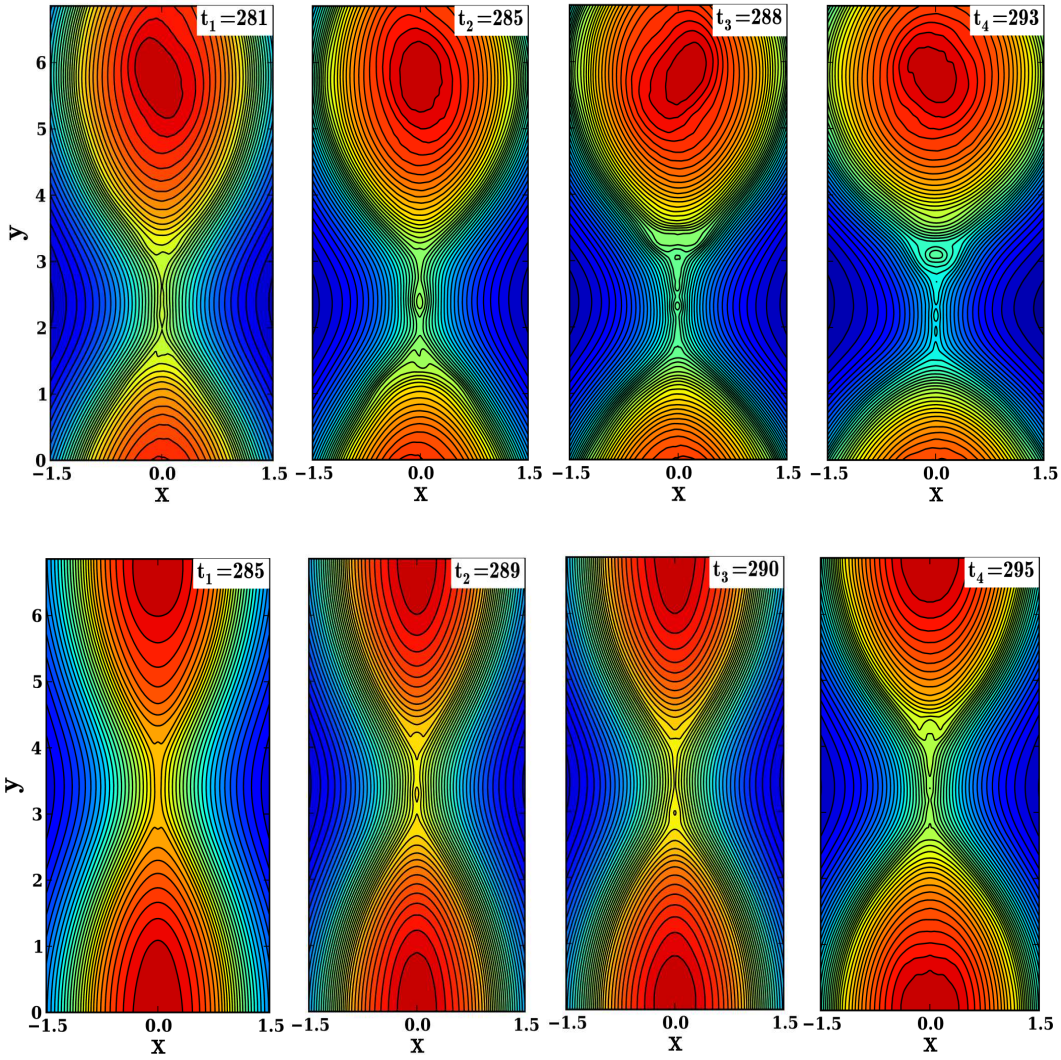

Figure 5.6: Contour plots of magnetic flux at different times during the nonlinear simulations for even-parity (upper panel) and odd-parity (lower panel), respectively. The other simulation parameters are, $\eta = 2.8 \times 10^{-4}$, $A = 8 \times 10^{-4}$ and $\Omega = 0.48$.

magnetic island oscillation effect is absent in the case of odd-parity flow as depicted in the lower panel of Figure 5.6. That's why in case of odd-parity flow, the plasmoid direction is not influenced by the dynamic flow.

It is noteworthy that the primary magnetic island is perfectly symmetric along the *y*-axis in the tearing mode evolution without flows, where the O-point of the single

secondary island coincides with the X-point of the primary island. However, including the dynamic flow with a finite k_y^{DF}, symmetries of the primary magnetic island along both *x*- and *y*-axes are affected significantly. The primary island is actually shifted either upward or downward along the *y*-axis and exhibits slight oscillations along *x*- and *y*-axes in the plasmoid dominated regime, depending on the flow properties. In the following, we will elaborate the linear stability analyses of the tearing mode by scanning the parametric dependence of the dynamic flows and quantify the flow effect on the magnetic reconnection by measuring the reconnected flux or effective reconnection rates.

5.4. Linear Stability Analysis

Though the main focus of our study is to explore the dynamics of impulsive nonlinear reconnection phase, however, it may be helpful to have a quick look at the linear stability properties of the tearing mode under the influence of a background dynamic flow. It is evident from Figure 5.4 that dynamic flows with even radial parity modify the linear growth rates of the tearing mode. However, in case of odd radial parity flows, the linear growths remain almost unaffected. This different response is identified to result from the local flow shear at the rational surface $x = 0$, which is maximum for the even parity flow and zero for the odd parity dynamic flow. To clarify this mechanism, we simulate the cases by artificially changing the local flow shear at the rational surface, confirming that as long as the local flow shear is strong in the resistive layer, the linear growth of the mode is significantly stabilized. Therefore, we limit the linear stability analysis of the tearing mode to even radial parity flow only. However, during the nonlinear evolution of tearing mode both even and odd parity flows are effective in modifying the reconnection properties.

5.4.1. Linear Growth Rate Dependence on the Dynamic Flow Amplitude

The dependence of linear tearing mode on the dynamic flow amplitude A, is investigated in the range of $A = 10^{-5} \sim 10^{-3}$. Simulations at a fixed frequency $\Omega = 0.08$ show that linear stabilization of the tearing mode is effective for the flow amplitude $A \geq 10^{-4}$. The maximum amplitude of the dynamic flow is chosen to be comparable to the level of the plasma flow. Figure 5.7(a) plots the growth rate verses the flow amplitude for three

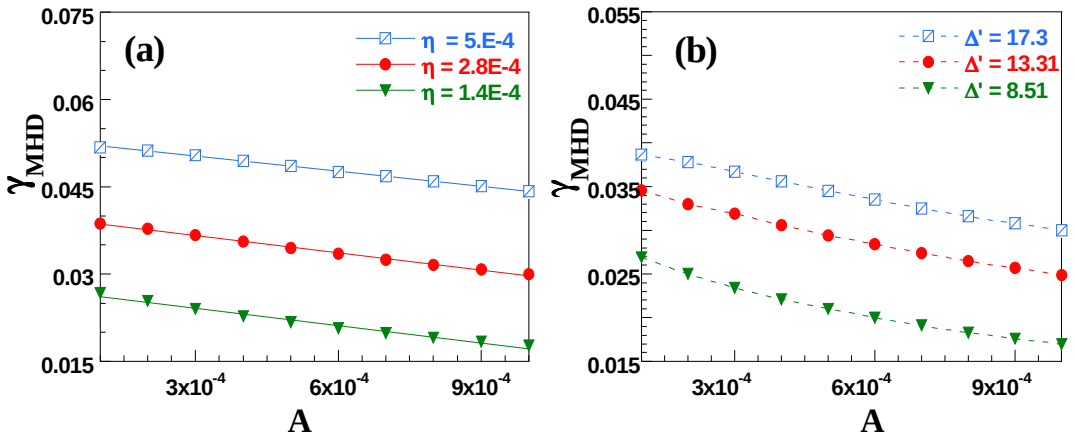

Figure 5.7: Linear growth rates of the tearing mode verses the amplitude of even radial parity dynamic flow for different values of η (a) and different values of Δ' (b).

resistivity cases at fixed $\Delta' = 17.3$. The stabilization effect due to the background dynamic flow gets enhanced with the flow amplitude and gets slightly stronger at lower resistivity. This is due to the fact that flow shear stabilization is more effective in narrow resistive layer (corresponding to lower η). Figure 5.7 (b) plots the growth rate verses the amplitude for three values of Δ' at a fixed resistivity $\eta = 2.8 \times 10^{-4}$, showing similar stabilization dependence.

5.4.2. Linear Growth Rate Dependence on the Dynamic Flow Frequency

Next, we analyze the frequency effect of the dynamic flow. Note that it is the finite frequency and k_y dependence of this flow, which distinguishes it from the usually considered random flows in turbulent reconnection. For the radial even parity flow with fixed k_y, linear simulations are performed in a broad frequency region with $\Omega = 0.0 \sim 2.0$, as shown in Figure 5.8, where the linear growth rates are plotted verses the turbulent flow frequency for three constant amplitudes. It seems reasonable to divide the entire frequency domain into three sub-regions: (I) Low frequency region, where the growth rate is remarkably reduced by the even-parity flow (even with negligible frequency), the stabilization weekly depends on the frequency. (II) Medium frequency

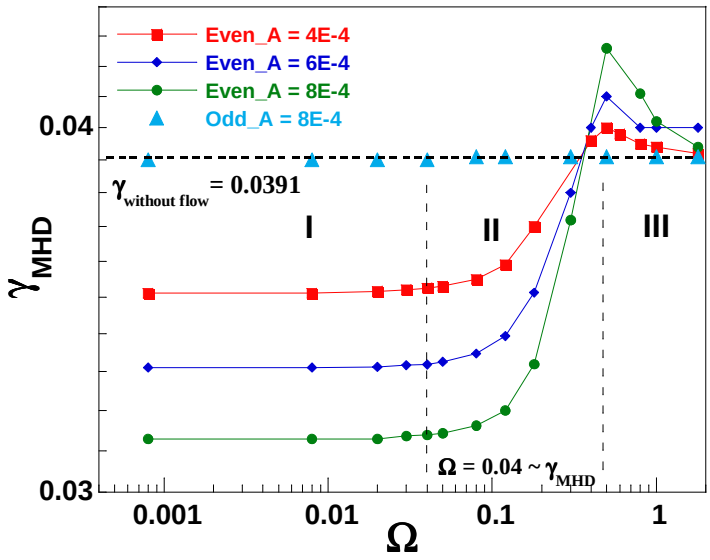

Figure 5.8: Linear growth rates of the tearing mode verses the frequency of radial even-parity dynamic flow for different amplitudes (solid curves). The triangular marks represent the case with odd-parity flow. The horizontal dashed line references the growth rate in the case without flow; vertical dashed lines partition the parameter region with different physical dependence. Simulation parameters are $\eta = 2.8 \times 10^{-4}$, $\Delta' = 17.3$ and $k_y^{DF} = 2.75$.

region with $\Omega \geq \Omega_c \approx \gamma_{\mathrm{MHD}}$, where the impact of dynamic turbulent flow becomes measurable. The critical frequency Ω_c in Fig. 4 is about 0.04. The tearing mode instability is significantly affected by the dynamic flow in this region. Specifically, the stabilization effect is evidently weakened by the finite frequency. This influence of the finite frequency flows on tearing mode instability is quite analogous to that of time dependent $\mathbf{E} \times \mathbf{B}$ flows in micro-turbulence [131, 132], where the flow frequency can reduce its role in suppressing the turbulence. (III) High frequency region with $\Omega \gg \gamma_{\mathrm{MHD}}$, where the flow stabilization effect almost disappears, and even slight destabilization takes place. In this region, the dependence of the dynamic flow effect on the flow frequency tends to be weak, suggesting that the macro-scale tearing mode perturbations hardly response directly to the micro-scale turbulent flow. However, high frequency dynamic flows may play vital role in

determining the onset criteria for the nonlinear impulsive reconnection phase even if they are linearly non-relevant. In addition, the growth rates verses the flow frequency for the case with odd-parity dynamic flow are also illustrated in Figure 5.8 (labeled by the blue triangular marks) for comparison, showing almost no impact of the odd-parity dynamic flow on the tearing mode instability.

5.5. Effective Reconnection Rates in Plasmoid-Dominated Phase

In order to explicate the two phase reconnection process in the presence of dynamic turbulent flow, we evaluate the magnetic reconnection by measuring the effective reconnection rate E_{eff} so that the flow effect can be quantitatively described. For the tearing mode without the external flow, the reconnection rate is defined in usual way as the rate of change of the reconnected magnetic flux along the current sheet, i.e. $E_{\text{eff}} = d\psi_{rec}/dt$, where ψ_{rec} is the reconnected flux, measured along the current sheet at $x = y = 0$. However, in the presence of background dynamic flow, this diagnostic is not applicable as it is, because of the turbulent motions of the current sheet and the plasmoids. In this case, reconnected magnetic flux ψ_{rec} is defined instead as the difference of maximum (O-point) and minimum (X-point) fluxes along the current sheet ($x = 0$). Thus the maximum and the minimum fluxes are evaluated at each time step to account for the dynamic behavior of the system. From this reconnected flux, instantaneous reconnection rate E is defined as follows:

$$E(t) = \frac{d\psi_{rec}}{dt} = \frac{d}{dt}\big(\max\big(\psi(0,y,t)\big) - \min\big(\psi(0,y,t)\big)\big). \tag{5.2}$$

In the plasmoid dominated impulsive reconnection regime, we get a fluctuating reconnection rate, which average value is defined as the effective reconnection rate E_{eff}. Alternatively, we get the same value of the effective reconnection rate by fitting slope to the fluctuating reconnected flux in the plasmoid dominated regime, where the reconnected flux approximately grows from 0.4 to 0.8 (for example, see Figure 9 (c)).

The reconnected flux and the corresponding reconnection rates are calculated for the dynamic flow with even radial parity and the corresponding original tearing mode without flow, by using this diagnostics and plotted in Figure 5.9 (c) and 5.9(d) respectively. In

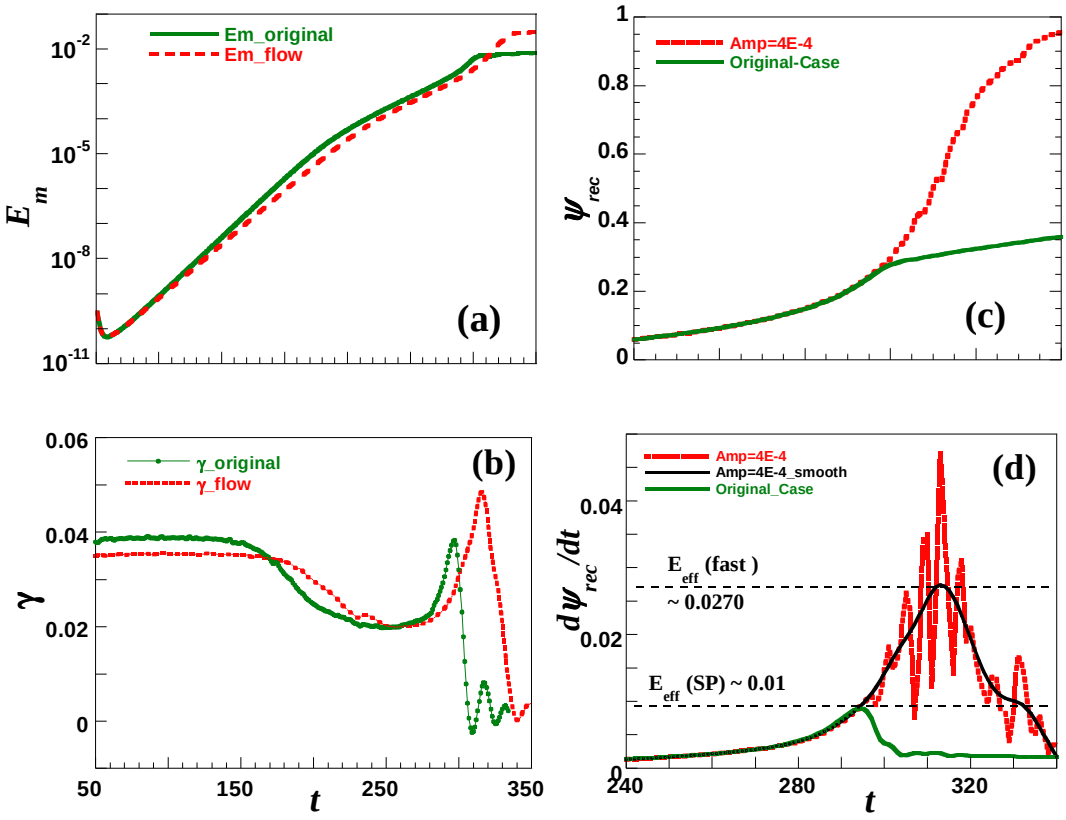

Figure 5.9: Time history of mean square perturbed magnetic potential $E_m = <\psi^2>/2$ (a); instantaneous growth rate of the corresponding magnetic flux (b); the reconnected magnetic flux(c); the reconnection rate (d) in a typical nonlinear simulation with even parity dynamic flow. Parameters are $\eta = 2.8 \times 10^{-4}$, $A = 4 \times 10^{-4}$ and $\Omega = 0.08$.

Figure 5.9(a) and 5.9 (b), we plot the time history of mean square magnetic potential and the instantaneous growth rate of the corresponding averaged magnetic flux. In the linear stage, the growth rate is stabilized by the dynamic flow, which plausibly delays the onset of the impulsive reconnection phase as evident from Figure 5.9 (b). After the quasistatic evolution of the current sheet in the SP reconnection phase, the plasmoids instability is triggered at once for the dynamic flow case, where the secondary plasmoids are continuously generated and ejected from the current sheet (see Figure 5.3 and Figure 5.5). These plasmoids grow in size, coalesce with each other, forming big monster plasmoid and finally coalesce with the primary island. This kind of plasmoid instability leads to sudden

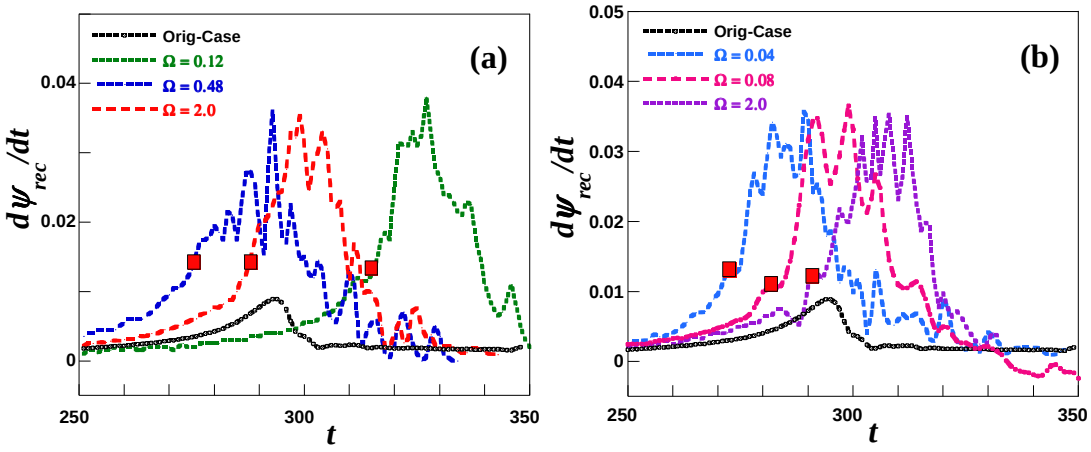

Figure 5.10: Time evolution of reconnection rates (a) for even-parity and, (b) odd parity dynamic flows with different frequencies. Parameters are $\eta = 2.8 \times 10^{-4}$ and $A = 8 \times 10^{-4}$. The symbols of red squares represent onset of the fast reconnection phase.

enhancement of the reconnected flux as depicted in Figure 5.9 (c). The impulsive bursty reconnection phase can easily be identified by the marked oscillations of the reconnected flux, which are more evident in the reconnection rate evolution (Figure 5.9 (d)). The corresponding effective reconnection rate in the plasmoid dominated phase is 0.027, which is much higher than the slow SP reconnection rate with a peak reconnection rate of 0.01.

5.6. Impulsive Reconnection as a Function of Flow Frequency

We next examine the onset conditions of the impulsive bursty reconnection as a function of frequency, parity and amplitude of the dynamic flow. For this purpose, we perform nonlinear simulations with different flow frequencies, both for odd and even radial parities. It is observed that the onset of the impulsive fast reconnection phase is considerably modified with the frequency of the dynamic flow, as depicted in Figure 5.10 for three different frequencies cases. The onset time of the impulsive bursty reconnection is marked by small squares, which actually indicate the start of the plasmoid instability. The onset time corresponds to the time when the secondary current sheet (SP type) starts fragmenting into small size plasmoids, which then enters into complex nonlinear stage.

From this time onward there is an evident increase in amplitude as well as fluctuations in the reconnection rate as depicted in Figure 10. Such fluctuations of the reconnection rate evolution correspond to the evolution dynamics of the plasmoids. The fluctuation level is modified with the plasmoid size. This fact is more evident from the magnetic flux contours of Figure 5.3. In the case of even-parity flow with $\Omega = 0.48$, the monster plamoids are formed at time $t = 292$, the corresponding fluctuation level in the reconnection rate is very high as shown in Figure 5.10 (a). For the higher frequency $\Omega = 2.0$, the level of fluctuation in the reconnection rate is low, because the plasmoid size is much smaller compared to that in the case of $\Omega = 0.48$. It seems that the fluctuation level scales almost linearly with plasmoid size however we have not confirmed the exact relation. In the case of the radial even-parity dynamic flows (Figure. 5.10 (a)), it is observed that the plasmoids dominated fast reconnection is triggered earlier with increasing the frequency, however, this tendency is reversed for higher frequency. On the other hand, for radial odd-parity flow, the onset time of the impulsive reconnection is delayed with the flow frequency as shown in Figure 5.10 (b).

5.7. Dependence of the Impulsive Reconnection on Flow Parity

To further clarify the dependence of the plasmoid onset on the flow frequency and radial parity, we plot the onset time of the plasmoid instability verses the flow frequency in a broad range of $\Omega = 0.04$ to 2.0, both for even and odd parity flows as depicted in Figure 5.11. For radial even parity dynamic flows, the onset of the impulsive reconnection is triggered early with the increasing flow frequency until $\Omega \sim 0.5$, beyond which this tendency of onset is reversed and becomes almost independent of the flow frequency. This kind of behavior is quite consistent with the linear analysis (Figure 5.8), where the stabilization effect gets reduced with the increasing flow frequency until some critical value, after which the growth rate comes back to the original value (that of without flow case). The odd radial flow exhibits different frequency dependence, where the onset time of the impulsive reconnection phase is delayed with the increasing flow frequency in a narrow frequency regime of $0.04 \leq \Omega \leq 0.12$ and finally not affected. This implies that the onset of the impulsive reconnection may not only depend on the linear growth

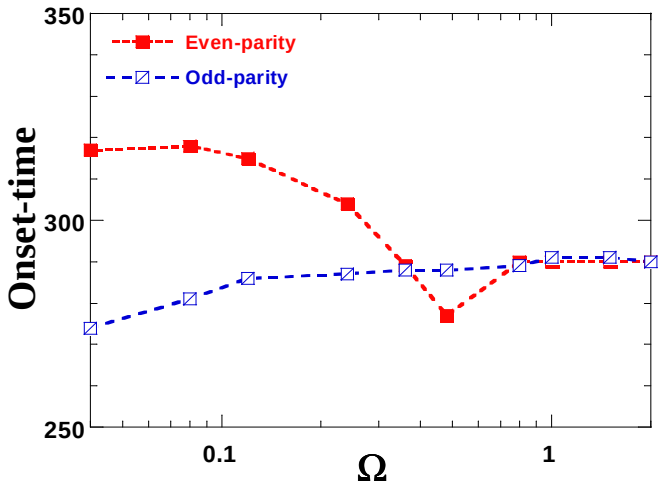

Figure 5.11: Onset time of the plasmoid dominated turbulent reconnection phase verses the dynamic flow frequency, both for even and odd radial parities. Parameters are $\eta = 2.8 \times 10^{-4}$, $A = 8 \times 10^{-4}$ and $\Omega = 0.08$.

behavior but also involve some nonlinear contributions. It is important to note that although the onset condition of the impulsive reconnection is significantly modified by the flow frequency, the effective peak reconnection rate in the turbulent phase is almost independent of the flow frequency, both for even and odd parity flows.

5.8. Impulsive Reconnection as a Function of Flow Amplitude

Amplitude of the dynamic flow is another important factor that can affect the impulsive reconnection behavior. Simulation results for three different flow amplitudes are presented in Figure 5.12 for both the odd and even radial parities. Compare to the high amplitude case in Figure 5.9, the two distinct reconnection phases are well separated for the low amplitudes flows. Actually, for low amplitude flows, the SP current sheet instead of directly inducing the plasmoid instability, leads to the formation of a single secondary island, which flows upward or downward, finally leading to the plasmoid instability. Thus, the onset time of impulsive bursty reconnection is delayed by decreasing the amplitude of the dynamic flow, both for even and odd parity flow. The difference in the onset time with

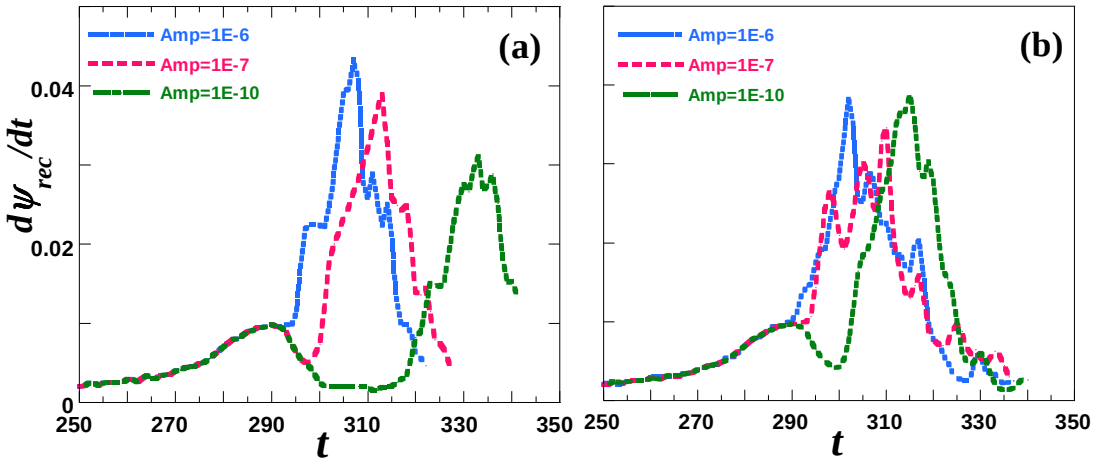

Figure 5.12: Time evolution of the reconnection rates for different dynamic flow with even (a) or odd (b) radial parity and amplitudes $A_{ITG} = 10^{-6}, 10^{-7}$ and 10^{-10}. Other parameters are $\eta = 2.8 \times 10^{-4}$ and $\Omega = 0.08$.

different flow amplitudes is more obvious for the even radial parity flow. The effective reconnection rate in case of even parity slightly decreases by reducing the flow amplitude, however, the effective reconnection rate is almost independent of the flow amplitude in case of odd parity dynamic flows. From this analysis we can conclude that the plasmoid instability is very weakly dependent on the turbulent flow amplitude. This is somewhat consistent with the previous turbulent reconnection studies [107] where they conclude that the role of the background turbulence is just to accelerate the triggering of the plasmoid instability and even very small amplitude random noise may be sufficient for the onset of the plasmoid instability. However, the role of external turbulence forcing and its type is still a debatable issue and further research is required in this regard.

5.9. Scaling Analysis of the Effective Reconnection Rate

Finally, it is worthwhile to confirm that the above mentioned plasmoid-dominated reconnection is truly a fast reconnection (which means independent of S). For this purpose, we perform scaling analysis of the effective reconnection rate with the Lundquist number. For fixed frequency and amplitude of the dynamic turbulent flow, effective peak

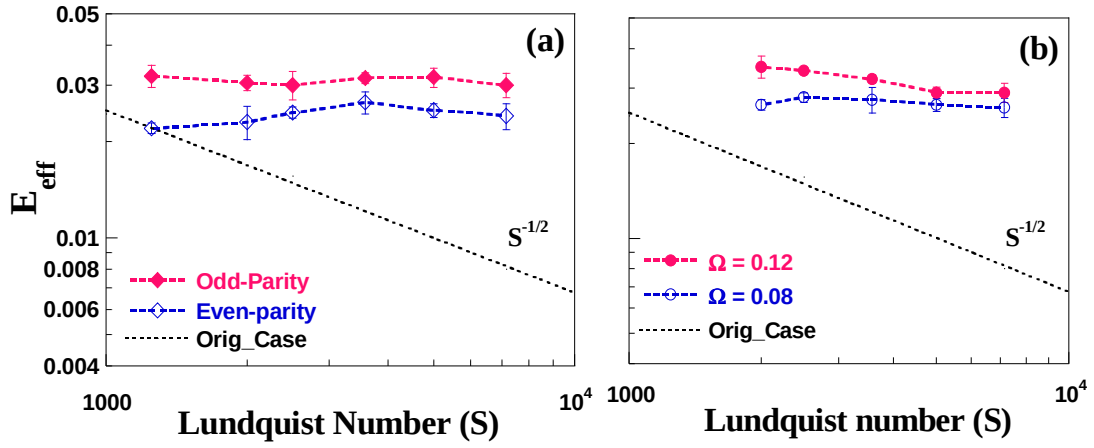

Figure 5.13: Effective reconnection rates verses S for different cases. (a) The flow with even or odd parity and frequency $\Omega = 0.08$ and amplitude $A_{ITG} = 4 \times 10^{-4}$; (b) the even parity flows with frequency $\Omega = 0.12$ or $\Omega = 0.08$ and amplitude $A_{ITG} = 8 \times 10^{-4}$. The dashed line shows the case without dynamic flow for reference.

reconnection rates are estimated for different resistivity runs with both even and odd radial parities. The resulting dependence of the effective reconnection rates on the Lundquist number $S = 1/\eta$ is depicted in Figure 5.13. For the sake of comparison, we also plot the reconnection rates of the resistive tearing mode without flow, depicting good agreement with the SP scaling $S^{-1/2}$ (represented by dashed line). Note that here the error bars represent the standard deviation. These results clearly demonstrate that the effective reconnection rate is almost independent of resistivity both for the odd and even parity flows as shown in Figure 5.13 (a), which implies that the plasmoid dominated turbulent reconnection is truly fast reconnection. It is noteworthy that the effective reconnection rate E_{eff} is higher for the odd radial parity case compared to the even parity at the same value of Lundquist number. The E_{eff} scaling with Lundquist number is also plotted for two different frequency cases as depicted in Figure 5.13 (b). A similar tendency is observed for the effective reconnection scaling with the Lundquist number, for both of the frequencies. However, the effective reconnection rate is slightly enhanced for higher frequency.

5.10. Discussion and Conclusions

We have performed a detailed numerical study of the two dimensional incompressible resistive magnetic reconnection with a finite frequency dynamic turbulent flow. We found that the linear stability properties of the tearing mode are moderately affected by dynamic flow with different radial parity, amplitude and frequency. More importantly, a two phase reconnection process is observed, where the quasistatic SP reconnection takes place in the first phase and is followed by the plasmoid-dominated fast reconnection in the second phase. The reconnection rate is significantly enhanced in the region of low resistivity for the typical dynamic flow parameters. In addition, the onset time of the plasmoid-dominated impulsive reconnection phase is strongly modified with the flow frequency and amplitude, and is more sensitive for the radial even-parity flows. The scaling of the effective reconnection rate with the Lundquist number S showed that the plasmoid-dominated reconnection is independent of S, which confirms that this is truly a fast reconnection. The enhancement of the reconnection rates which is observed by including the dynamic flow may be associated with the dynamic multiple plasmoid generation along the current sheet, quite similar to the previous observations in turbulent reconnection [103-111]. In most of those studies the turbulent effects were usually introduced by an external forcing term in the form of random noise. However, so far there is no universal agreement on the role of the random noise in the magnetic reconnection process. Thus, instead of the random noise we considered the ITG-like small scale turbulence in our study, which made it possible to explore the effects of finite frequency and radial parity of the turbulent flow on the magnetic reconnection process and is quite analogous to the real physical situation where the MHD tearing mode interacts with the small scale ITG driven turbulence.

In this study, we did not include the viscosity effects, however small values of viscosity (Prandtl number $Pr = \mu/\eta \ll 1$) are used to avoid numerical problems. The inclusions of strong viscosity $Pr \geq 1$ might affect the reconnection process by modifying the onset criteria of the current sheet and the SP scaling and therefore may also modify the impulsive reconnection phase. Therefore, finitely large values of viscosity may affect the impulsive reconnection process and is left for future study. Another, feature of the flow not covered in this study is the wave number k_y^{DF}. Throughout this study, we kept a constant

value of $k_y^{DF} = 2.75$ for the dynamic flow. However, in realistic physical situations, it may be necessary to consider a broad spectrum of k_y^{DF}, which may add further complexity to the nonlinear MHD turbulence interactions. Finally, it may be useful to analyze the impact of changing the boundary conditions and the equilibrium profiles on the magnetic reconnection behavior of resistive tearing mode with the pre-existing small scale turbulence.

Chapter 6

Conclusions and Future Work

In the limit of large instability parameter Δ' (strongly driven regime), the nonlinear dynamics of resistive tearing mode exhibit an abrupt growth phase after the Rutherford's slow nonlinear phase, which is accompanied by a collapse of the typical X-point configuration to Y-type current sheet. The physical trigger mechanism for the X-point collapse, leading to the explosive growth dynamics, is still an unresolved issue. Moreover, the role of viscosity in the transition from slow nonlinear phase to abrupt growth phase has not been considered in the previous studies. Another big issue in the present day reconnection research is the identification of mechanism responsible for the observed faster reconnection rates in weakly collisional plasmas with high Lundquist number $S = 1/\eta$, compared to the much slower reconnection rates predicted by the Sweet Parker (SP) theory. This thesis is thus devoted to the study of the complex nonlinear dynamics of the resistive tearing mode, focusing on the investigation of the trigger mechanism for the X-point collapse as well as the role of viscosity in the transition from slow growth phase to the abrupt reconnection phase. Furthermore, the case of turbulent magnetic reconnection is also addressed in this study, aiming to get faster reconnection rates by exciting the dynamic plasmoid instability and hence fill the gap between theory and observations.

In order to achieve these objectives, the incompressible two field reduced-magnetohydrodynamics (RMHD) equations are solved as initial value problem in the simplified two-dimensional slab geometry. The simulation code is first benchmarked for the linear growth rate scaling of the resistive tearing instability for various plasma parameters. The main achievements of this study includes the identification of the physical trigger mechanism for the X-point collapse, as well as the role of plasma viscosity μ on the critical conditions for the transition from the slow nonlinear growth phase to the abrupt

growth phase. A secondary instability analysis was proposed, which testified that zonal current peaking may plausibly be responsible for the onset of explosive growth dynamics. In addition, a new transition criterion for the critical island width of the X-point collapse was suggested by performing a comprehensive nonlinear scaling analysis of the critical island width in terms of $\Delta' W_c$ verses the viscosity. Moreover, by introducing a pre-existing dynamic turbulent flow in the RMHD system, the plasmoid-dominated impulsive bursty reconnection is studied. Through such analysis, we actually tried to realize the real physical situation where the MHD tearing mode interacts with the small scale ITG driven turbulence.

6.1. Conclusions

For the sake of convenience, the key findings of this research study are summarized as follows:

1. The nonlinear evolution of the resistive tearing mode is investigated in the framework of RMHD, where the transition from the slow Rutherford regime to the Sweet Parker reconnection phase is observed in the case of large enough instability parameter Δ' and low values of resistivity. This transition is identified by the change in the magnetic island configuration, where the X-point geometry is replaced by a narrow current sheet. The trigger mechanism of such X-point collapse is studied in detail.
2. A secondary instability analysis is proposed based on the quasilinear modification of the equilibrium current profile due to the zonal current. Thus, the new equilibrium contains two parts, the original equilibrium and the instantaneous value of the zonal current. The zonal current modifies the equilibrium profile in two ways, by inducing local peaking of the current profile at the rational surface and broadening of the current profile in the region away from the resistive layer.
3. The secondary instability analysis is applied separately for the zonal current peaking and broadening effects. The simulation results reveal that actually it is the local current peaking effect due to the zonal current that results in a nonlinear positive feedback to enhance the tearing mode fluctuations, signifying a probable

mechanism for the onset of X-point collapse and explosive nonlinear growth. On the other hand, flattening of the equilibrium profile causes stabilization of the growth rates. By including finitely large viscosity, the current peaking and broadening effect due to the zonal current is reduced, however, from secondary analysis a similar tendency as found in non-viscous case, is observed.

4. It is found that the previous scaling of the critical island width for the X-point collapse $\Delta' w_c$ [67] is modified in the presence of finite viscosity. A new transition criterion is suggested for the critical island width scaling by including the viscosity dependence [125]: $\Delta' w_c \approx C(\mu) + g(\Delta', \mu)\eta$ (Equation 4.8)

5. Viscosity modifies the scaling of critical island width mainly in two ways: reducing the slopes of its scaling with resistivity and up-shifting the value of the critical island width in the limit of zero resistivity. Most importantly, a transition behavior is observed in the critical island width scaling with the viscosity at $P_r = 1$.

6. In the speed up reconnection phase, the reconnection rate scaling strongly depends on the plasma viscosity, showing almost no change in $P_r < 1$ regime and strong stabilization effect in $P_r > 1$ regime.

7. The resistive tearing mode reconnection is found to be significantly modified by including a finite frequency dynamic turbulent flow, quite similar to an electrostatic ITG wave and is coupled with the stream function and magnetic flux through Poisson brackets.

8. The linear and nonlinear reconnection properties of the resistive tearing mode are analyzed by including a background dynamic turbulent flow. Linear stability properties of the tearing mode are found to be moderately modified with the dynamic flow, depending on the radial parity, frequency and amplitude of the flow. In particular, it is observed that by increasing the flow frequency beyond a critical value i. e. ($\Omega \geq \Omega_c \approx \gamma_{\mathrm{MHD}}$), the stabilization effect of the dynamic flow is reduced, quite analogous to that of time dependent $\mathbf{E} \times \mathbf{B}$ flows in micro-turbulence [131, 132].

9. The linear stability properties of the tearing mode are found to be modified only in the case of even-parity dynamic flow. This different response for even and odd parity flows is identified to result from the local flow shear at the rational surface $x = 0$, which is maximum for even-parity flow and zero for the odd-parity dynamic flow.

10. Most importantly, the nonlinear evolution of magnetic island exhibits two phase reconnection by including the dynamic flow. A current sheet is formed in the first phase where slow SP reconnection takes place and is followed by the plasmoid instability in the second phase, where multiple plasmoids are continuously generated and ejected along the current sheet, leading to a bursty impulsive reconnection. The onset time of the plasmoid-dominate impulsive reconnection is strongly modified with the flow frequency and parity.

11. The direction of ejection of the plamoids is found to be dependent on the radial flow profile (whether symmetric or anti-symmetric) as well as the flow frequency. In the case of even-parity, the ejection direction alternates after the half period of the flow oscillation. Alternation of the direction of the plasmoids ejection tends to be fast as the flow frequency increases. However, in the case of odd-parity, the flow has no effect on the direction of plasmoid ejection. This implies that the plasmoid will be ejected either in upward or downward direction, depending on its position where it is close to the upper or lower end of the current sheet.

12. The difference between the radial odd and even parity cases is further illustrated by the primary magnetic island dynamic behavior in the nonlinear phase. The primary magnetic island exhibit rotation with the radial symmetric dynamic flows and no impact for the anti-symmetric flows. The frequency of the island rotation is exactly the same as that of the imposed turbulent flow. This result is quite consistent with the previous simulations [112].

13. Another important result is the formation of monster plasmoid in the impulsive nonlinear reconnection phase. The monster plasmoid are formed only if the secondary island is created at the center of the narrow secondary current sheet. Our observations suggest that monster plasmoids occur more probably in the case of

even-parity flow with intermediate frequencies. The maximum size of the monster plasmoid can be roughly estimated to be ~ 0.164, which is close to the observed value of $w_{max} \sim 0.17$, for the even-parity case of $\Omega \sim 0.48$ in Figure 5.3.

14. Finally, the scaling of reconnection rates is found to be independent of resistivity, which signify the fact that plasmoid-dominated reconnection is truly fast reconnection. Thus our results suggest enhancement of the reconnection rates with the inclusion of finite frequency dynamic turbulent flow, most probably by the generation of multiple dynamic plasmoids along the current sheet.

6.2. Future Work

6.2.1. Improvement of the Numerical Code

The numerical study of the current sheet and plasmoid instability require very high resolution since such instability can only be observed in the limit of large values of the instability parameter Δ' and small resistivity η. Thus, we need to improve the numerical resolution of our simulation code (in spatial domain), to unearth the hidden physics of the nonlinear resistive tearing mode reconnection. Another possible improvement may be increasing the accuracy of the finite difference scheme by employing higher order schemes. This will make it easy to increase the numerical resolution along the radial direction. The tearing mode evolution continues for much longer times for small values η, which means it is the waste of computational resources to use fixed mesh size. Therefore, it will be very useful to implement the adaptive mesh algorithm in our simulation code, which will make it possible to study the more realistic high Lundquist number regimes. To further enhance the speed of our simulations, it will be really helpful to parallelize our numerical code.

6.2.2. The Multi-scale Problem

In the last part of this thesis, we discussed the impact of pre-existing dynamic turbulent flow similar to the ITG-like electrostatic wave, on the resistive tearing mode reconnection process. Actually, the coexistence of MHD activities including the tearing mode and ITG

driven drift wave have been reported to occur commonly in magnetic fusion plasmas[113-115]. Those studies have revealed that multi-scale turbulence and resistive MHD interaction may provide new destabilizing/stabilizing mechanism. The fluctuations from different scales can directly interact with each other or indirectly affect through a zonal flow. Thus, it is quite important to consider the impact of ITG-turbulence (with full spectrum of wavelengths) on the impulsive fast magnetic reconnection in the case of resistive tearing mode.

6.2.3. Reconnection beyond Resistive-MHD

In this study, we have analyzed the tearing mode reconnection in the framework of resistive MHD, where the nonlinear evolution exhibits the formation of slowly evolving Sweet Parker type current sheet. However, it has been known for quite some time that such a current sheet can be unstable to the plasmoid instability at high Lundquist number S with critical values of the order of $S{\sim}10^4$. Actually at such high values of S, the resistive MHD description is no more valid and the current sheet width reaches the kinetic scales. Then the two fluid (Hall) and kinetic effects become important. For example, without a guide field, the transition from the slow collisional (Resistive MHD) to the fast collisionless Hall MHD occurs if the half thickness of the current sheet predicted by SP model is smaller than the ion skin depth, i.e. $\delta_{SP} < d_i$, where δ_{SP} represent the SP current sheet width and d_i is the ion skin depth and which should be replaced by the ion Larmor radius at the sound speed ρ_s , if the strong guide field is considered [87-93]. There are two possibilities, either the secondary current sheet becomes thin enough to directly trigger the collisionless Hall reconnection or alternatively, the current sheet is unstable to the collisional plasmoid instability, leading to much thinner inter-plasmoid current sheets, which can onset the fast Hall reconnection. Therefore, transition from the collisional plasmoid instability to the collisionless Hall reconnection can be a promising future reconnection study. Furthermore, it may be interesting to investigate the impact of small scale background turbulence on the onset of plasmoid-induced Hall reconnection.

6.2.4. The 3D Effects

The results presented in this thesis are based on 2D study. The validity of these results in the more realistic 3D geometry is still poorly understood that needs further investigations. However, a few 3D studies have recently been performed using the Harris sheet equilibrium and including a strong guide field [133-134]. The main consequence of incorporating the guide field in the third dimension is that the 2D island now becomes flux ropes, which can are defined as regions of helical field. In addition to the formation of the flux ropes (magnetic island), there are many other 3D processes, which can affect the reconnection, e.g. streaming instability, low-hybrid drift instability and kinetic instabilities. Therefore, it is worthwhile to explore the physics of fast magnetic reconnection (for example the plasmoid-dominated impulsive reconnection) in complex but realistic 3D geometries.

Appendixes

A. Normalization of the RMHD equations

In this appendix, we describe the normalization implemented in RMHD equations. The details are as follows:

- Lengths are normalized to some characteristic length a (layer width of the current carrying region near the singular surface).
- Time is normalized to the Alfvén time, $\tau_A = a \,/\, v_A$, where v_A is Alfvén velocity defined by $v_A = B_0/\sqrt{\mu_0\rho_0} = B_0/\sqrt{\mu_0}$ (assuming that $\rho_0 = 1$) .
- The magnetic field is normalized to the in-plane guide magnetic field B_0.

For sake of convenience let rewrite the Ohm's law (equation (2.27)) and equation of motion (equation (2.37)):

$$\partial_t \psi + [\phi, \psi] = \frac{1}{\mu_0}\eta \nabla^2 \psi, \tag{A. 1}$$

$$\partial_t (\nabla^2 \phi) + [\phi, \nabla^2 \phi] = \frac{1}{\mu_0}[\psi, \nabla^2 \psi] + \mu \nabla^2 (\nabla^2 \phi) \tag{A. 2}$$

With these normalizations, the fields are represented as follows:

$$\hat{\psi} = \frac{\psi}{aB_0}, \qquad \hat{\phi} = \frac{\phi}{av_A},$$

$$\hat{k}_y = ak_y, \qquad \hat{B}_{0y}(x) = \frac{\mathrm{B}_{0y(x)}}{B_0}.$$

Implementing the above normalization, equation (A.1) can be written as:

$$\frac{aB_0}{\tau_A}\frac{\partial \hat{\psi}}{\partial \hat{t}} + \frac{1}{a^2}\left[av_A\hat{\phi}, aB_0\hat{\psi}\right] = \frac{\eta}{\mu_0}\frac{aB_0}{a^2}\hat{\nabla}^2\hat{\psi}, \tag{A. 3}$$

$$\Rightarrow aB_0\left\{\frac{1}{\tau_A}\frac{\partial\hat{\psi}}{\partial\hat{t}}+\frac{av_A}{a^2}\left[\hat{\phi},\hat{\psi}\right]\right\}=aB_0\frac{\eta}{\mu_0}\frac{1}{a^2}\hat{\nabla}^2\hat{\psi} \quad (A.4)$$

$$\Rightarrow \frac{1}{\tau_A}\frac{\partial\hat{\psi}}{\partial\hat{t}}+\frac{v_A}{a}\left[\hat{\phi},\hat{\psi}\right]=\frac{\eta}{\mu_0}\frac{1}{a^2}\hat{\nabla}^2\hat{\psi} \quad (A.5)$$

$$\Rightarrow \frac{1}{\tau_A}\frac{\partial\hat{\psi}}{\partial\hat{t}}+\frac{1}{\tau_A}\left[\hat{\phi},\hat{\psi}\right]=\frac{\eta}{\mu_0}\frac{1}{a^2}\hat{\nabla}^2\hat{\psi} \quad (A.6)$$

$$\Rightarrow \frac{\partial\hat{\psi}}{\partial\hat{t}}+\left[\hat{\phi},\hat{\psi}\right]=\frac{\eta}{\mu_0}\frac{\tau_A}{a^2}\hat{\nabla}^2\hat{\psi} \quad (A.7)$$

$$\Rightarrow \frac{\partial\hat{\psi}}{\partial\hat{t}}+\left[\hat{\phi},\hat{\psi}\right]=\frac{\eta}{\mu_0 a v_A}\hat{\nabla}^2\hat{\psi}, \quad (A.8)$$

$$\Rightarrow \frac{\partial\hat{\psi}}{\partial\hat{t}}+\left[\hat{\phi},\hat{\psi}\right]=\hat{\eta}\hat{\nabla}^2\hat{\psi}. \quad (A.9)$$

Where, $\hat{\eta}=\eta/\mu_0 a v_A=1\ /\ S$ (S represents the Lundquist number and is also defined as the ratio of the resistive time to Alfvén time).

Now, from the equation of motion we get:

$$\frac{av_A}{a^2\tau_A}\frac{\partial}{\partial\hat{t}}\left(\hat{\nabla}^2\hat{\phi}\right)+\frac{1}{a^2}\left[av_A\hat{\phi},\frac{av_A}{a^2}\hat{\nabla}^2\hat{\phi}\right]=\frac{1}{\mu_0}\frac{(aB_0)^2}{a^2}\left[\hat{\psi},\frac{1}{a^2}\hat{\nabla}^2\hat{\psi}\right]+\mu\frac{av_A}{a^4}\hat{\nabla}^2\left(\hat{\nabla}^2\hat{\phi}\right) \quad (A.10)$$

$$\Rightarrow \frac{1}{\tau_A}\frac{v_A}{a}\frac{\partial}{\partial\hat{t}}\left(\hat{\nabla}^2\hat{\phi}\right)+\frac{v_A^2}{a^2}\left[\hat{\phi},\hat{\nabla}^2\hat{\phi}\right]=\frac{1}{\mu_0}\frac{B_0^2}{a^2}\left[\hat{\psi},\hat{\nabla}^2\hat{\psi}\right]+\mu\frac{v_A}{a^3}\hat{\nabla}^2\left(\hat{\nabla}^2\hat{\phi}\right) \quad (A.11)$$

$$\Rightarrow \frac{1}{\tau_A^2}\frac{\partial}{\partial\hat{t}}\left(\hat{\nabla}^2\hat{\phi}\right)+\frac{1}{\tau_A^2}\left[\hat{\phi},\hat{\nabla}^2\hat{\phi}\right]=\frac{1}{\mu_0}\frac{B_0^2}{a^2}\left[\hat{\psi},\hat{\nabla}^2\hat{\psi}\right]+\mu\frac{v_A}{a^3}\hat{\nabla}^2\left(\hat{\nabla}^2\hat{\phi}\right) \quad (A.12)$$

$$\Rightarrow \frac{\partial}{\partial\hat{t}}\left(\hat{\nabla}^2\hat{\phi}\right)+\left[\hat{\phi},\hat{\nabla}^2\hat{\phi}\right]=\frac{\tau_A^2}{\mu_0}\frac{B_0^2}{a^2}\left[\hat{\psi},\hat{\nabla}^2\hat{\psi}\right]+\mu\frac{\tau_A^2 v_A}{a^3}\hat{\nabla}^2\left(\hat{\nabla}^2\hat{\phi}\right) \quad (A.13)$$

$$\Rightarrow \frac{\partial}{\partial\hat{t}}\left(\hat{\nabla}^2\hat{\phi}\right)+\left[\hat{\phi},\hat{\nabla}^2\hat{\phi}\right]=\left[\hat{\psi},\hat{\nabla}^2\hat{\psi}\right]+\frac{\mu}{a v_A}\hat{\nabla}^2\left(\hat{\nabla}^2\hat{\phi}\right) \quad (A.14)$$

$$\Rightarrow \frac{\partial}{\partial\hat{t}}\left(\hat{\nabla}^2\hat{\phi}\right)+\left[\hat{\phi},\hat{\nabla}^2\hat{\phi}\right]=\left[\hat{\psi},\hat{\nabla}^2\hat{\psi}\right]+\hat{\mu}\hat{\nabla}^2\left(\hat{\nabla}^2\hat{\phi}\right). \quad (A.15)$$

Where, $\hat{\mu}$ is the normalized viscosity. In addition, the diffusion of the equilibrium magnetic field in the Ohm's law is prevented by adding an externally applied electric field

$E_0 = -\eta\nabla^2\psi_0$ to the right-hand side of equation (A.9). Thus, dropping the hats, the final form of the normalized RMHD equations is given as follows:

$$\partial_t\psi = -[\phi, \psi] + \eta\nabla^2(\psi - \psi_0), \tag{A.16}$$

$$\partial_t(\nabla^2\phi) = -[\phi, \nabla^2\phi] + [\psi, \nabla^2\psi] + \mu\nabla^2(\nabla^2\phi). \tag{A.17}$$

The above two equations are actually solved in our simulation studies to analyze the evolution of the perturbed flux and plasma flow.

B. Delta Prime Calculations

In this section, we detail calculations of the instability parameter Δ' for two types of equilibrium profiles. First, we consider the 1/cosh^2 and latter will repeat the analysis for the Harris equilibrium. The basic approach is the same as reported in [121].

B.1 Equilibrium profile of 1/cosh^2(x)

Let consider the equilibrium in generalized form as follows:

$$\psi_{0y}(x) = \psi_0 \,\mathrm{sech}^2(x/a) \tag{B.1}$$

The analytical expressions for the corresponding B_{0y}, J_{0z} and J'_{0z} are given below.

$$B_{0y}(x) = \left(\frac{\partial \psi_{0y}}{\partial x}\right) = -\frac{2}{a}\psi_0 \,\mathrm{sech}^2(x/a)\,\tanh(x/a) \tag{B.2}$$

$$\mathrm{J}_{0z}(x) = \left(\frac{\partial^2 \psi_0}{\partial x^2}\right) = \frac{2}{a^2}\psi_0 \,\mathrm{sech}^4(x/a)\,[\cosh(2x/a) - 2] \tag{B.3}$$

$$\mathrm{J}'_{0z}(x) = \frac{8}{a^3}\,\psi_0 \mathrm{sech}^5(x/a)\,\sinh\,(x/a)[3 - \cosh^2(x/a)] \tag{B.4}$$

To calculate the instability parameter Δ', we have to solve equation (3.12) for the perturbation flux ψ_1. For the sake of convenience, we rewrite the equation (3.12):

$$\psi_1''(x) - \left(k_y^2 + \frac{\mathrm{J}'_0}{\mathrm{B}_{0y}}\right)\psi_1(x) = 0 \tag{B.5}$$

Inserting the equilibrium expression into the above equation, we obtain:

$$\psi_1''(x) - \left(k_y^2 + \frac{\frac{8}{a^3}\,\psi_0 \mathrm{sech}^5(x/a)\,\sinh\,(x/a)[3 - \cosh^2(x/a)]}{-\frac{2}{a}\psi_0 \,\mathrm{sech}^2(x/a)\,\tanh(x/a)}\right)\psi_1(x) = 0 \tag{B.6}$$

After simplification, we can easily obtain the following equation:

$$\psi_1''(x) - \left(k_y^2 + \frac{4}{a^2} - \frac{12}{a^2\cosh^2(x/a)}\right)\psi_1(x) = 0 \tag{B.7}$$

$$\Rightarrow \psi_1''(x) - \frac{1}{a^2}\left(a^2k_y^2 + 4 - \frac{12}{\cosh^2(x/a)}\right)\psi_1(x) = 0$$

$$\Rightarrow \psi_1''(x) - \frac{1}{a^2}\left(\bar{\mathrm{k}}^2 - \frac{12}{\cosh^2(x/a)}\right)\psi_1(x) = 0 \qquad \text{(B. 8)}$$

Where, $\bar{\mathrm{k}}^2 = a^2k_y^2 + 4$.

$$\Rightarrow \psi_1''(x) - \frac{4}{a^2}\left(\frac{\bar{\mathrm{k}}^2}{4} - \frac{3}{\cosh^2(x/a)}\right)\psi_1(x) = 0 \qquad \text{(B. 9)}$$

In order to solve the above equation, we make use of the following transformation;

$\mathrm{z} = 1/\cosh^2(x/a)$ and $\psi(x) = \psi_{\mathrm{z}}(x)\mathrm{z}^{-\bar{\mathrm{k}}/2}$.

To avoid confusion, we may write it as, $\psi(x) = \phi_{\mathrm{z}}(x)\mathrm{z}^{-\bar{\mathrm{k}}/2}$, (i.e. $\psi_{\mathrm{z}}(x) = \phi_{\mathrm{z}}(x)$)

Therefore,

$$\frac{\partial \mathrm{z}}{\partial x} = -\frac{2}{a}\mathrm{sech}^2\left(\frac{x}{a}\right)\tanh\left(\frac{x}{a}\right) \quad \Rightarrow \frac{\partial \mathrm{z}}{\partial x} = -\frac{2}{a}z\sqrt{(1-z)},$$

$$\frac{\partial^2 \mathrm{z}}{\partial x^2} = \frac{4}{a^2}\left(z - \frac{3}{2}z^2\right).$$

Now, we can write:

$$\psi(x) = \phi_z(x)z^{-\bar{k}/2} \Rightarrow \psi'(x) = \frac{\partial\phi}{\partial z}\frac{\partial z}{\partial x}z^{-\bar{k}/2} - \phi_z\frac{\bar{k}}{2}z^{-\frac{\bar{k}}{2}-1}\frac{\partial z}{\partial x}$$

$$\Rightarrow \psi'(x) = \left[z'\phi_z' - \frac{\bar{k}}{2}\frac{z'}{z}\phi_z\right]z^{-\bar{k}/2} \qquad \text{(B. 10)}$$

Similarly we can have,

$$\Rightarrow \psi''(x) = \left(z'\phi_z' + z'^2\phi_z'' + \frac{\bar{k}}{2}\frac{1}{z^2}z'^2\phi_z - \frac{\bar{k}}{2}\frac{1}{z}z''\phi_z - \frac{\bar{k}}{2}\frac{1}{z}z'^2\phi_z'\right)z^{-\bar{k}/2}$$

$$+\left(z'\phi_z' - \frac{\bar{k}}{2}\frac{1}{z}z'\phi_z\right)(-\bar{k}/2)(z'.z^{-\frac{\bar{k}}{2}-1}) \qquad \text{(B. 11)}$$

After some simplifications, finally we get:

$$\psi''(x) = \left[z.z(1-z)\phi_z'' + z\left\{\left(1-\bar{k}\right) - \left(\frac{3}{2}-\bar{k}\right)z\right\}\right.$$
$$\left. + \left\{\frac{\bar{k}^2}{4} - \frac{\bar{k}^2}{4}z - \frac{\bar{k}}{2}z + \frac{3\bar{k}}{4}z\right\}\phi_z\right]\left(\frac{4}{a^2}\right)z^{-\frac{\bar{k}}{2}} \quad \text{(B. 12)}$$

Putting the values of $\psi'(x)$ and $\psi''(x)$ into equation (B.12), we obtain:

$$z(1-z)\psi_z'' + \left(\left(1-\bar{k}\right) - \left(\frac{3}{2}-\bar{k}\right)z\right)\psi_z' - \left(\frac{\bar{k}^2}{4} - \frac{\bar{k}}{4} - 3\right)\psi_z = 0 \quad \text{(B. 13)}$$

This is the well known Gauss' hypergeometric equation, which is easy to solve.

Now, let compare this equation with the general form of hypergeometric equation:

$$z(1-z)\psi_z'' + (c-(a+b+1)z)\psi_z' - ab\psi_z = 0 \quad \text{(B. 14)}$$

Comparing equations (B.13) and (B.14), we get:

$$c = 1-\bar{k} \quad \text{(B. 15)}$$

$$ab = \frac{\bar{k}^2}{4} - \frac{\bar{k}}{4} - 3 \quad \text{(B. 16)}$$

$$a+b+1 = \frac{3}{2} - \bar{k}. \quad \text{(B. 17)}$$

Inserting the value of "a" from equation (B.16) into equation (B.15), we get the following quadratic equation.

$$4b^2 + \left(4\bar{k}-2\right)b + \left(\bar{k}^2 - \bar{k} - 12\right) = 0 \quad \text{(B. 18)}$$

Solving this equation, we obtain: $b = 2 - \bar{k}/2$ and $a = -3/2 - 3\bar{k}/2$

The standard solution of the hypergeometric equation (B.14) is given as:

$$\psi_k(z) = {}_2F_1(a, b;\ c;\ x) + x^{1-c}\,{}_2F_1(a-c+1, b-c+1;\ 2-c;\ x) \quad \text{(B. 19)}$$

In the same, the solution of equation (B.13) is given as follows:

$$\psi_{\mathrm{k}}(\mathrm{z}) = \mathrm{C}_1\,{}_2\mathrm{F}_1\left(-\frac{3}{2}-\frac{\bar{\mathrm{k}}}{2}, 2-\frac{\bar{\mathrm{k}}}{2}; 1-\bar{\mathrm{k}}; \mathrm{z}\right) + \mathrm{C}_2\mathrm{z}^{\bar{\mathrm{k}}}\,{}_2\mathrm{F}_1\left(-\frac{3}{2}+\frac{\bar{\mathrm{k}}}{2}, 2+\frac{\bar{\mathrm{k}}}{2}; 1+\mathrm{k}; \mathrm{z}\right) \quad \text{(B. 20)}$$

In terms of the original variables, equation (B.20) is written as:

$$\psi_k(x)z^{\frac{\bar{k}}{2}} = C_1\,{}_2F_1\left(-\frac{3}{2}-\frac{\bar{k}}{2}, 2-\frac{\bar{k}}{2}; 1-\bar{k}; \cosh^{-2}\left(\frac{x}{a}\right)\right)$$

$$+C_2 z^{\bar{k}}\,{}_2F_1\left(-\frac{3}{2}+\frac{\bar{k}}{2}, 2+\frac{\bar{k}}{2}; 1+\bar{k}; \cosh^{-2}(x/a)\right) \qquad \text{(B. 21)}$$

$$\Rightarrow \psi_k(x) = C_1\left(\cosh^{-2}(x/a)\right)^{-\bar{k}/2}\,{}_2F_1\left(-\frac{3}{2}-\frac{\bar{k}}{2}, 2-\frac{\bar{k}}{2}; 1-\bar{k}; \cosh^{-2}(x/a)\right)$$

$$+C_2\left(\cosh^{-2}(x/a)\right)^{\bar{k}/2} z^{\bar{k}}\,{}_2F_1\left(-\frac{3}{2}+\frac{\bar{k}}{2}, 2+\frac{\bar{k}}{2}; 1+\bar{k}; \cosh^{-2}(x/a)\right) \qquad \text{(B. 22)}$$

To vanish this solution at large *x*, we assume $C_1 = 0$ and $C_2 = 1$, thus we get:

$$\Rightarrow \psi_{\bar{k}}(x) = \left(\cosh(x/a)\right)^{-\bar{k}}\,{}_2F_1\left(-\frac{3}{2}+\frac{\bar{k}}{2}, 2+\frac{\bar{k}}{2}; 1+\bar{k}; \cosh^{-2}(x/a)\right) \qquad \text{(B. 23)}$$

The instability parameter can now be estimated as follows:

$$\Delta' = \frac{\psi_1'(0+) - \psi_1'(0-)}{\psi_1(0)} \approx 2\frac{\psi_1'(0+)}{\psi_1(0)} \qquad \text{(B. 24)}$$

From equation (B. 23) we get:

$$\psi_{\bar{k}}(0) = {}_2F_1\left(-\frac{3}{2}+\frac{\bar{k}}{2}, 2+\frac{\bar{k}}{2}; 1+\bar{k}; 1\right)$$

$$\Rightarrow \psi_{\bar{k}}(0) = \frac{\Gamma(\bar{k}+1).\Gamma\left((\bar{k}+1) - \left(-\frac{3}{2}+\frac{\bar{k}}{2}\right) - \left(2+\frac{\bar{k}}{2}\right)\right)}{\Gamma\left((\bar{k}+1)\left(-\frac{3}{2}+\frac{\bar{k}}{2}\right)\right)\Gamma\left((\bar{k}+1) - \left(2+\frac{\bar{k}}{2}\right)\right)}$$

$$\Rightarrow \psi_{\bar{k}}(0) = \frac{\Gamma(\bar{k}+1).\Gamma\left(\frac{1}{2}\right)}{\Gamma\left(\frac{\bar{k}}{2}-1\right)\Gamma\left(\frac{\bar{k}}{2}+\frac{5}{2}\right)} \qquad \text{(B. 25)}$$

Note that in above manipulations, we have used the following property:

$${}_2F_1(a, b; c; 1) = \frac{\Gamma(c).\Gamma(\mathrm{c}-\mathrm{a}-\mathrm{b})}{\Gamma(c-a)\Gamma(c-b)} \qquad \text{(B. 26)}$$

Next, each term in equation (B.25) is simplified using the properties;

$$\Gamma(z+1) = z\Gamma(z)$$

$$\Gamma(z)\Gamma(z+1/2) = \frac{2\sqrt{\pi}}{2^{2z}}\,\Gamma(2z)$$

Finally in simplified form, the equation (B.25) is expressed as:

$$\Rightarrow\ \psi_{\bar{k}}(0) = \frac{2^{\bar{k}}.\,\bar{k}(\bar{k}-2)}{(\bar{k}+1)(\bar{k}+3)} \tag{B.27}$$

Next, we determine $\psi'_{\bar{k}}(x)$;

By definition,

$$\psi'_{\bar{k}}(x) = \frac{d\psi(z)}{dz}\frac{dz}{dx} \tag{B.28}$$

Now,

$$\psi_{\bar{k}}(z) = z^{\bar{k}/2}\,{}_2F_1(\alpha,\beta;\gamma;z)$$

$$\frac{d\psi(z)}{dz} = \frac{d}{dz}\left\{dz^{\frac{\bar{k}}{2}}\,{}_2F_1(\alpha,\beta;\gamma;z)\right\}$$

$$\Rightarrow \frac{d\psi(z)}{dz} = \frac{\bar{k}}{2}z^{\frac{\bar{k}}{2}-1}\,{}_2F_1(\alpha,\beta;\gamma;z) + z^{\frac{\bar{k}}{2}}.\frac{\alpha\beta}{\gamma}\,{}_2F_1(\alpha+1,\beta+1;\gamma+1;z) \tag{B.29}$$

Since,

$$\frac{d\psi(z)}{dz} = -\frac{2}{a}z\sqrt{1-z} \tag{B.30}$$

Putting equations (B.29) and (B.30) into equation (B.28), we get:

$$\psi'_{\bar{k}}(x) = \frac{\bar{k}}{a}z^{\bar{k}/2}\sqrt{1-z}\ {}_2F_1(\alpha,\beta;\gamma;z) - \frac{2\alpha\beta}{a\gamma}z^{\frac{\bar{k}}{2}+1}\ {}_2F_1(\gamma-\alpha,\gamma-\beta;\gamma+1;z) \tag{B.31}$$

Where we have used, the properties;

$${}_2F_1(\alpha,\beta;\gamma;z) = {}_2F_1(\gamma-\alpha,\gamma-\beta;\gamma;z)$$

From equation (B.13) in the limit of $x \to 0^+(z \to 1)$, the first term goes to zero, we get;

$$\lim_{x\to 0^+}\psi'_{\bar{k}}(0^+)=\lim_{z\to 1}\psi'_{\bar{k}}(0^+)=-\frac{2\alpha\beta}{a\gamma}\ {}_2F_1(\gamma-\alpha,\gamma-\beta;\gamma+1;z) \tag{B.32}$$

$$\Rightarrow\ \psi'_{\bar{k}}(0^+)=-\frac{2\left(-\frac{3}{2}+\frac{\bar{k}}{2}\right)\left(2+\frac{\bar{k}}{2}\right)}{a\left(1+\bar{k}\right)}\ {}_2F_1\left(\frac{\bar{k}}{2}+\frac{5}{2},\frac{\bar{k}}{2}-1;\bar{k}+2;1\right) \tag{B.33}$$

$$\Rightarrow\psi'_{\bar{k}}(0^+)=-\frac{2^{\bar{k}}\left(\bar{k}-1\right)\left(\bar{k}-3\right)}{a\left(\bar{k}+2\right)} \tag{B.34}$$

Thus the instability parameter can now be calculated as follows:

$$\Delta'=\ 2\frac{\psi'_1(0+)}{\psi_1(0)}=-\frac{2.2^{\bar{k}}\left(\bar{k}-1\right)\left(\bar{k}-3\right)}{a\left(\bar{k}+2\right)}\ \frac{\left(\bar{k}+1\right)(\bar{k}+3)}{2^{\bar{k}}.\bar{k}(\bar{k}-2)} \tag{B.35}$$

$$\Rightarrow\ \Delta'=\ -\frac{2}{a}\frac{\left(\bar{k}^4-10\bar{k}^2+9\right)}{\bar{k}(\bar{k}^2-4)} \tag{B.36}$$

$$\Rightarrow\ \Delta'=\ \frac{2}{a}\frac{\left(-\bar{k}^4+6\bar{k}^2+4\bar{k}^2-9\right)}{\bar{k}(\bar{k}^2-4)} \tag{B.37}$$

$$\Rightarrow\ \Delta'=\ \frac{2}{a}\left[\frac{6\bar{k}^2-9}{\bar{k}(\bar{k}^2-4)}-\bar{k}\right] \tag{B.38}$$

Where, $\bar{k}^2=a^2k_y^2+4$. This is the instability parameter Δ' for the given equilibrium profile $\psi_{0\mathrm{y}}(x)=\psi_0\,\mathrm{sech}^2(x/a)$. Note that in this study, we have considered the equilibrium profile with $a=1$ and $\psi_0=1$.

B.2 Equilibrium profile of Harris sheet

Let consider Harris sheet equilibrium:

$$\psi_{0\mathrm{y}}(x)=\mathrm{a}\psi_0\log[\cosh(x/a)] \tag{B.39}$$

The analytical expressions for the corresponding B_{0y}, J_{0z} and J'_{0z} are given below.

$$B_{0y}(x)=\left(\frac{\partial\psi_{0y}}{\partial x}\right)=\psi_0\tanh(x/a) \tag{B.40}$$

$$\mathrm{J}_{0z}(x)=\left(\frac{\partial^2\psi_0}{\partial x^2}\right)=\frac{\psi_0}{a}\ \mathrm{sech}^2(x/a) \tag{B.41}$$

$$J'_{0z}(x) = -\frac{2\psi_0}{a^2}\,\mathrm{sech}^2(x/a)\tanh(x/a) \qquad (B.42)$$

To calculate the instability parameter Δ', we have to solve equation (3.12) for the perturbation flux ψ_1. For the sake of convenience, we rewrite the equation (3.12):

$$\psi_1''(x) - \left(k_y^2 + \frac{J'_0}{B_{0y}}\right)\psi_1(x) = 0 \qquad (B.43)$$

Inserting the equilibrium expression into the above equation, we obtain:

$$\psi_1''(x) - \left(k_y^2 + \frac{-\frac{2\psi_0}{a^2}\,\mathrm{sech}^2(x/a)\tanh(x/a)}{\psi_0\tanh(x/a)}\right)\psi_1(x) = 0 \qquad (B.44)$$

After simplification, we can easily obtain:

$$\psi_1''(x) - \left(k_y^2 - \frac{2}{\cosh^2(x/a)}\right)\psi_1(x) = 0 \qquad (B.45)$$

$$\Rightarrow\ \psi_1''(x) - \frac{4}{a^2}\left(\frac{a^2k_y^2}{4} - \frac{1}{2\cosh^2(x/a)}\right)\psi_1(x) = 0 \qquad (B.46)$$

$$\Rightarrow\ \psi_1''(x) - \frac{4}{a^2}\left(\frac{k^2}{4} - \frac{1}{2\cosh^2(x/a)}\right)\psi_1(x) = 0 \qquad (B.47)$$

Where, $k^2 = a^2k_y^2$.

In order to solve the above equation, we use similar transformation as applied in the previous equilibrium case;

$$\mathrm{z} = 1/\cosh^2(x/a),$$
$$\psi(x) = \psi_{\mathrm{z}}(x)\mathrm{z}^{-\mathrm{k}/2}$$

To avoid confusion, we may write it as, $\psi(x) = \phi_{\mathrm{z}}(x)\mathrm{z}^{-\mathrm{k}/2}$, (i.e. $\psi_{\mathrm{z}}(x) = \phi_{\mathrm{z}}(x)$)

Therefore,

$$\frac{\partial \mathrm{z}}{\partial x} = -\frac{2}{a}z\sqrt{(1-z)},$$

$$\frac{\partial^2 \mathrm{z}}{\partial x^2} = \frac{4}{a^2}\left(z - \frac{3}{2}z^2\right).$$

Thus, we can write:

$$\psi(x) = \phi_z(x)\mathrm{z}^{-\mathrm{k}/2}$$

$$\Rightarrow \psi'(x) = \left[z'\phi_z' - \frac{\mathrm{k}}{2}\frac{z'}{z}\phi_z\right]\mathrm{z}^{-\mathrm{k}/2} \qquad \text{(B.48)}$$

After some simplifications, we can get:

$$\psi''(x) = \left[z.z(1-z)\phi_z'' + z\left\{(1-k) - \left(\frac{3}{2}-k\right)z\right\}\right.$$
$$\left. + \left\{\frac{\mathrm{k}^2}{4} - \frac{\mathrm{k}^2}{4}z - \frac{\mathrm{k}}{2}z + \frac{3\mathrm{k}}{4}z\right\}\phi_z\right]\left(\frac{4}{a^2}\right)\mathrm{z}^{-\frac{\mathrm{k}}{2}} \qquad \text{(B.49)}$$

Putting the values of $\psi'(x)$ and $\psi''(x)$ into equation (B.47), we obtain:

$$z(1-z)\psi_z'' + \left((1-k) - \left(\frac{3}{2}-k\right)z\right)\psi_z' - \left(\frac{\mathrm{k}^2}{4} - \frac{\mathrm{k}}{4} - \frac{1}{2}\right)\psi_z = 0 \qquad \text{(B.50)}$$

This is the Gauss' hypergeometric equation, which is solved in the same manner as done in the previous case, by comparing with the general form.

Comparing equations (B.50) and (B.14), we get:

$$c = 1 - k \qquad \text{(B.51)}$$

$$ab = \frac{k^2}{4} - \frac{k}{4} - 3 \qquad \text{(B.52)}$$

$$a + b + 1 = \frac{1}{2} - k. \qquad \text{(B.53)}$$

Solving the above relations for *a* and *b*, we can easily obtain;

$$a = -\frac{1}{2} - \frac{k}{2} \;\; and \;\; b = 1 - \frac{k}{2}$$

Now, the solution of the hypergeometric equation (B.50) is given as follows:

$$\psi_k(z) = C_1\,{}_2F_1\left(-\frac{1}{2} - \frac{k}{2}, 1 - \frac{k}{2}; 1-k; z\right)$$

$$+C_2 z^k \, {}_2F_1\left(-\frac{1}{2}+\frac{k}{2}, 1+\frac{k}{2}; 1+k; z\right) \quad \text{(B.54)}$$

In terms of the original variables, equation (B.20) is written as:

$$\psi_k(x) z^{\frac{k}{2}} = C_1 \, {}_2F_1\left(-\frac{1}{2}-\frac{k}{2}, 1-\frac{k}{2}; 1-k; \cosh^{-2}\left(\frac{x}{a}\right)\right)$$

$$+C_2 z^k \, {}_2F_1\left(-\frac{3}{2}+\frac{k}{2}, 2+\frac{k}{2}; 1+k; \cosh^{-2}(x/a)\right) \quad \text{(B.55)}$$

$$\Rightarrow \psi_k(x) = C_1\left(\cosh^{-2}(x/a)\right)^{-k/2} \, {}_2F_1\left(-\frac{3}{2}-\frac{k}{2}, 2-\frac{k}{2}; 1-k; \cosh^{-2}(x/a)\right)$$

$$+C_2\left(\cosh^{-2}(x/a)\right)^{k/2} z^{\bar{k}} \, {}_2F_1\left(-\frac{3}{2}+\frac{k}{2}, 2+\frac{k}{2}; 1+k; \cosh^{-2}(x/a)\right) \quad \text{(B.56)}$$

At large *x*, we assume $C_1 = 0$ and $C_2 = 1$, thus we get:

$$\Rightarrow \psi_{\bar{k}}(x) = \left(\cosh(x/a)\right)^{-k} \, {}_2F_1\left(-\frac{3}{2}+\frac{k}{2}, 2+\frac{k}{2}; 1+k; \cosh^{-2}(x/a)\right) \quad \text{(B.57)}$$

The instability parameter can now be estimated as follows:

$$\Delta' = \frac{\psi_1'(0+) - \psi_1'(0-)}{\psi_1(0)} \approx 2\frac{\psi_1'(0+)}{\psi_1(0)} \quad \text{(B.58)}$$

$$\psi_{\bar{k}}(0) = {}_2F_1\left(-\frac{1}{2}+\frac{k}{2}, 1+\frac{k}{2}; 1+k; 1\right)$$

$$\Rightarrow \psi_{\bar{k}}(0) = \frac{\Gamma(k+1).\Gamma\left(\frac{1}{2}\right)}{\Gamma\left(\frac{k}{2}\right)\Gamma\left(\frac{k}{2}+\frac{3}{2}\right)} = \frac{2^k.k}{(k+1)} \quad \text{(B.59)}$$

Next, we determine $\psi_k'(x)$;

By definition,

$$\psi_k'(x) = \frac{d\psi(z)}{dz}\frac{dz}{dx} \quad \text{(B.60)}$$

Now,

$$\psi_k(z) = z^{k/2}\,{}_2F_1(\alpha,\beta;\gamma;z)$$

$$\frac{d\psi(z)}{dz} = \frac{d}{dz}\left\{dz^{\frac{k}{2}}\,{}_2F_1(\alpha,\beta;\gamma;z)\right\}$$

Finally, we get:

$$\psi_k'(x) = \frac{\bar{k}}{a} z^{\bar{k}/2}\sqrt{1-z}\;{}_2F_1(\alpha,\beta;\gamma;z) - \frac{2\alpha\beta}{a\gamma} z^{\frac{k}{2}+1}\;{}_2F_1(\gamma-\alpha,\gamma-\beta;\gamma+1;z) \qquad (B.61)$$

From equation (B.61) in the limit of $x \to 0^+ (z \to 1)$, the first term goes to zero, we get;

$$\lim_{x\to 0^+}\psi_k'(0^+) = \lim_{z\to 1}\psi_k'(0^+) = -\frac{2\alpha\beta}{a\gamma}\;{}_2F_1(\gamma-\alpha,\gamma-\beta;\gamma+1;z) \qquad (B.62)$$

$$\Rightarrow\ \psi_k'(0^+) = -\frac{2\alpha\beta}{a\gamma}\;{}_2F_1\left(\frac{k}{2}+\frac{3}{2},\frac{k}{2};k+2;1\right) \qquad (B.63)$$

$$\Rightarrow\ \psi_k'(0^+) = -\frac{2\left(-\frac{1}{2}+\frac{k}{2}\right)\left(1+\frac{k}{2}\right)}{a(1+k)}\left(\frac{\Gamma(k+2).\,\Gamma\left(\frac{1}{2}\right)}{\Gamma\left(\frac{k}{2}+\frac{1}{2}\right)\Gamma\left(\frac{k}{2}+2\right)}\right)$$

$$\Rightarrow \psi_k'(0^+) = -\frac{2^k(k-1)}{a} \qquad (B.64)$$

Thus the instability parameter can now be calculated as follows:

$$\Delta' = 2\frac{\psi_1'(0+)}{\psi_1(0)} = -\frac{2.\,2^k(k-1)}{a} \qquad (B.65)$$

$$\Rightarrow\ \Delta' = -\frac{2}{a}\left(k-\frac{1}{k}\right) \qquad (B.66)$$

Where, $k^2 = a^2k_y^2$.

C. List of Scientific Contributions

Reviewed Journal Papers

- Ahmad Ali, Jiquan Li, Yasuaki Kishimoto, "On the abrupt growth dynamics of nonlinear resistive tearing mode and the viscosity effects".
  Physics of Plasmas **21**, 052312 (1-9) (2014).

- Ahmad Ali, Jiquan Li, Yasuaki Kishimoto, "On the magnetic reconnection of resistive tearing mode with the dynamic flow effects".
  Accepted for publication in Physics of Plasmas (March 4, 2015).

Conference Contributions and Presentations

- Ahmad Ali, Jiquan Li, Yasuaki Kishimoto, "On the magnetic reconnection of resistive tearing mode with the dynamic flow effects", Plasma Conference 2014, November 18-21, 2014, Niigata, Japan (oral presentation), Proceeding of Plasma Conference 2014, 18pC2-7.

- Ahmad Ali, Jiquan Li, Yasuaki Kishimoto, "Viscosity effects on the explosive growths of nonlinear resistive tearing mode", the 23rd International Toki Conference (ITC-23) November 18-21, 2013, Ceratopia Toki-City, Gifu, Japan (poster presentation), Special Issue 2 (2014), Plasma and Fusion Research 9, 3401036 (2014), the 23rd International Toki Conference (ITC-23) on Large-Scale Simulation and Fusion Science.

- Ahmad Ali, Jiquan Li, Yasuaki Kishimoto, "Viscosity effects on the explosive growth dynamics of nonlinear resistive tearing mode", NIFS-Workshop on "Theory and Simulation for the Stability of Flow in MHD and Fluid Dynamics", Dec 18-19, 2013, NIFS, Japan (oral presentation).

- Ahmad Ali, Jiquan Li, Yasuaki Kishimoto, “Secondary instability analysis of current sheet formation in tearing mode”, Sokendai Asian Winter School, Jan 29-Feb1, 2013, NIFS, Japan (poster presentation).

- Ahmad Ali, Jiquan Li, Yasuaki Kishimoto, “Numerical study of nonlinear explosive behavior of tearing mode”, 4th GCOE International Symposium, 22-23 May, 2012, Bangkok, Thailand (poster presentation).

Bibliography

[1] G.M. McCracken and P.E. Stott, “Fusion: The Energy of the Universe”, Complementary Science Series, Elsevier Academic Press, 2005.

[2] W. M. Stacey, “An Introduction to the Physics and Technology of Magnetic Confinement”, John Wiley & Sons, Inc, New York, 1984.

[3] J. Reader *et al.*, ‘‘Controlled Nuclear Fusion”, John Wiley and sons New York, 1986.

[4] M. Kikuchi *et al.*, “Fusion Physics”, International Atomic Energy Agency, Vienna, 2012.

[5] ENDF database at the IAEA: http://www-nds.iaea.org/exfor/e4explorer.htm

[6] NRL Plasma Formulary, pages 44-45, Edn 2007.

[7] Eurofusion Organization, “Tokamak Principle”.

https://www.euro-fusion.org/2011/09/tokamak-principle-2/?view=gallery-11

[8] ITER Organization: http://www.iter.org/sci/beyonditer

[9] M. Keilhacker *et al.*, Nuclear Fusion, **39**, 209 (1999).

[10] A. Kitsumezaki *et al.*, Fusion Science and Technology **42**,179 (2002).

[11] R. J. Hastie, Astro Phys. Space Sci, **256**, 177 (1997).

[12] A. Retino, D. Sundkvist, A. Vaivads, F. Mozer, M. Andre and C. J. Owen, Nature Phys. **3**, 236 (2007).

[13] Dieter Biskamp, “*Magnetic Reconnection in plasmas”*, Cambridge University Press, 2000.

[14] Eric Priest and Terry Forbes, “*Magnetic Reconnection*”, Cambridge University Press, 2000.

[15] K. Shibata and T. Magara, Living Rev. Solar Phys. **8**, 6 (2011).

[16] B. B. Kadomtsev, Sov. J. Plasma Phys. **1**, 389 (1975).

[17] J. Wesson, Tokamaks (Clarendon, London, 1987).

[18] M. Yamada *et al.* Phys. Plasmas **1**, 3269 (1994).

[19] J. B. Taylor, Rev. Mod. Phys. **58**, 741 (1986).

[20] M. Yamada, *et al.* Phys. Fluids B **3**, 2379 (1991).

[21] R. Giovanelli, Nature **158**, 81 (1946).

[22] E. Zweibel and M. Yamada, Annu. Rev. Astron. Astrophys. 47, 291 (2009).

[23] M. Yamada, R. Kulsrud, and H. Ji, Rev. Mod. Phys. **82**, 603 (2010).

[24] R. C. Carrington, Description of a singular appearance seen in the Sun on September 1, 1859, Mon. Not. R. Astron. Soc., XX, **13** (1859).

[25] R. Hodgson, "on a curious appearance seen in the Sun", Mon. Not. R. Astron. Soc., XX, **15** (1859).

[26] H. Carmichael, in The Physics of Solar Flares, Proceedings of the AAS-NASA Symposium, edited by W. N. Hess NASA, Washington, D.C., p. 451 (1964).

[27] P. A. Sturrock, Nature, London **211**, 695 (1966).

[28] T. Hirayama, Sol. Phys. **34**, 323 (1974).

[29] R. A. Kopp and G. W. Pneuman, Sol. Phys. **50**, 85 (1976).

[30] J. Dungey, Phys. Rev. Lett. **6**, 47 (1961).

[31] E. Loomis, On the geographic distribution of auroras in the northern hemisphere, Am. J. Sci. Arts, **30**, 89–94 (1860).

[32] S.-I. Akasofu, The development of the auroral substorm, Planet Space Sci., **12**, 273–282 (1964).

[33] S.-I. Akasofu, Auroral Phenomenology and Magnetospheric Processes, Geophysical Monograph Series **197**, (2012).

[34] S. von Goeler, W. Stodiek, N. Sauthoff, Phys. Rev. Lett. **33**, 1201 (1974).

[35] M. Yamada, Phys. Plasmas **18**, 111212 (2011).

[36] P. A. Sweet, in Proceedings of the IAU Symposium 6: Electromagnetic Phenomena in Cosmical Physics, Cambridge University Press, Cambridge, England, p. 123 (1958).

[37] E. N. Parker, J. Geophys. Res. **62**, 509 (1957).

[38] Edwards et al, Phys. Rev. Lett. **57**, 210 (1986).

[39] R. M. Green, Modes of annihilation and reconnection in magnetic fields, in Stellar and Solar Magnetic Fields. Proc. IAU Symp. 22, edited by R. Lust, pp. 398–404, North-Holland (1965).

[40] B. V. Somov and S. I. Syrovatskii. Hydrodynamic Plasma Flow in a Strong Magnetic Field. In N.G. Basov, editor, *Neutral Current Sheets in Plasmas*, p. 13 (1976).

[41] A. H. Boozer, Phys. Plasmas, **19**, 092902 (2012).

[42] R. Horiuchi and T. Sato, Phys. Plasmas **6**, 4565 (1999).

[43] Karimabadi *et al.*, "Ion-ion kink instability in the magnetotail:2", J. Geophys. Res, 108, 1401 (2003).

[44] Drake *et al.*, "Formation of electron holes and particle energization during magnetic reconnection", Science 299, 873 (2003).

[45] Yin et al., Phys Rev. Lett. **101**, 125001 (2008).

[46] H. E. Petschek, NASA Spec. Publ., **50**, 425 (1964).

[47] Y. Ishii *et al.*, Phys. Plasmas **7**, 4477 (2000).

[48] Y. Ishii, M. Azumi and Y. Kishimoto, Phys. Rev. Lett. **89**, 205002 (2002).

[49] Z. X. Wang *et al.*, Phys. Rev. Lett. **99**, 185004 (2007).

[50] M. Janvier, Y. Kishimoto, and J. Li, Phys. Rev. Lett. **107**, 195001, (2011).

[51] M. Janvier, Y. Kishimoto, and J. Li, Nucl. Fusion, **51**, 083016 (2011).

[52] H. P. Furth, J. Killeen, and M.N. Rosenbluth, Phys. Fluids **6**, 459 (1963).

[53] P.H. Rutherford, Phys. Fluids **16**, 1903 (1973).

[54] R.B. White *et al.*, Phys. Fluids **20**, 800 (1977).

[55] F. Militello and F. Porcelli, Phys. Plasmas **11**, L13 (2004).

[56] D. F Escande and M. Ottaviani, Phys. Plasmas **13**, 052305 (2006).

[57] D. Biskamp and H. Welter, Numerical studies of resistive instabilities, Plasma Phys. and Controlled Nuclear Fusion Research, IAEA, Vienna, **I**, 579–89 (1976).

[58] R.B. White *et al.*, Non-linear tearing modes in tokamaks, Plasma Phys. and Controlled Nuclear Fusion Research, IAEA, Vienna, **1**, 569–577 (1977).

[59] R. S. Steinolfson and G. Van Hoven, Nonlinear evolution of the resistive tearing mode, Phys. Fluids, **27**(5), 1207–14 (1984).

[60] D. Biskamp, Nonlinear Magnetohydrodynamics, Cambridge University Press, Cambridge, 1993.

[61] S. Migliuolo, F. Pegoraro and F. Porcelli, Phys. Fluids B, **3(6)**, 1338-45 (1991).

[62] S. V. Bulanov, J. Sakai and S.I. Syrovatskii, Sov. J. of Plasma Phys., **5**, 157–63 (1979).

[63] F. L. Waelbroeck, Phys. Fluids B **1**, 2372 (1989).

[64] F. L. Waelbroeck, Phys. Rev. Lett. **70**, 3259 (1993).

[65] B. D. Jemella *et al*. Phys. Rev. Lett. **91**, 125002 (2003).

[66] B. D. Jemella, J. F. Drake and M. A. Shay, Phys. Plasmas **11**, 5668 (2004).

[67] N. F. Loureiro *et al*. Phys. Rev. Lett. **95**, 235003 (2005).

[68] K. Itoh *et al*., J. Phys. Soc. Jpn **62**, 4269(1993).

[69] A. Furuya, S. Itoh, and M. Yagi, J. Phys. Soc. Jpn. **70**, 407 (2001).

[70] S. C. Guo, R. Paccagnella and F. Romanelli, Phys. Plasmas **1**, 2741(1994).

[71] K. Takeda et al, Phys. Plasmas **15**, 022502 (2008).

[72] S. L. Spitzer, *Physics of fully ionized gases*, (Inter-Science, Newyork, 1956).

[73] F. Pocelli, Phys. Fluids **30**, 1734 (1987).

[74] D. Grasso, R. J. Hastie, F. Porcelli and C. Tebaldi, phys. Plasmas 15, 072113 (2008).

[75] F. Militello *et al*., Phys. Plasmas **18**, 112108 (2011).

[76] G. Einaudi and Rubini, Phys. Fluids B **1**, 2224 (1989).

[77] L. Ofman, X. L. Chen, and P. J. Morrison, Phys. Fluids B 3, 1364 (1991).

[78] A. Bhattacharjee *et al.*, Phys. Plasmas **16**, 112102 (2009).

[79] W. Daughton *et al*., Phys. Rev. Lett. **103**, 065004 (2009).

[80] Samtaney *et al.*, Phys. Rev. Lett. **103**, 105004 (2009).

[81] D. A. Uzdensky, N. F. Loureiro, and A. A. Schekochihin, Phys. Rev. Lett. **105**, 235002 (2010).

[82] Y. M. Huang, A. Bhattacharjee, and B. P. Sullivan, Phys. Plasmas **18**, 072109 (2011).

[83] N. F. Loureiro *et al.* Phys. Plasmas **19**, 042303 (2012).

[84] N. F. Loureiro, A. A. Schekochihin and S. C. Cowley, Phys. Plasmas **14**, 100703 (2007).

[85] N. F. Loureiro, A. A. Schekochihin, and D. A. Uzdensky, Phys. Rev. **E 87**, 013102 (2013).

[86] Y. M. Huang, and A. Bhattacharjee, Phys. Plasmas **20**, 055702 (2013).

[87] Z. W. Ma, and A. Bhattacharjee, Geophys. Res. Lett. **23**, 1673 (1996).

[88] D. Biskamp, E. Schwarz, and J. F. Drake, "Ion controlled collisionless magnetic reconnection", Phys. Rev. Lett. **75**, 3850 (1995).

[89] M. A. Shay, J. F. Drake, and B. N. Rogers, Geophys. Res. Lett. **26**, 2163 (1999).

[90] J. Birn *et al*., J. Geophys. Res. **106**, 3715 (2001).

[91] M. Yamada *et al*., Phys. Plasmas **13**, 052119 (2006).

[92] P. A. Cassak, M. A. Shay, and J. F. Drake, Phys. Rev. Lett. **95**, 235002 (2005).

[93] Doughton. Phys. Plasmas **13**, 072101 (2006).

[94] M. Ugai, T. Tsuda, and J. Plasma Phys. **17**, 337 (1977).

[95] T. Sato and T. Hayashi, Phys. Fluids **22**, 1189 (1979).

[96] M. Scholer, J. Geophys. Res. **94**, 8805 (1989).

[97] R. Kulsrud, Earth, Planets Space **53**, 417 (2001).

[98] D. A. Uzdensky, Astrophys. J. **587**, 450 (2003).

[99] D. Biskamp, Phys. Fluids **29**, 1520 (1986).

[100] D. Uzdensky, and R. Kulsrud, Phys. Plasmas **7**, 4018 (2000).

[101] N. V. Erkaev *et al.*, Phys. Plasmas, **8**, 4800 (2001).

[102] Malyshkin, L., T. Linde, and R. Kulsrud, Phys. Plasmas **12**, 102902 (2005).

[103] W. H. Matthaeus and S. L. Lamkin, Phys. Fluids, **29**, 2513 (1986).

[104] A. Lazarian and E. T. Vishniac, ApJ, **517**, 700 (1999).

[105] G. Lapenta, Phys. Rev. Lett., **100**, 235001 (2008).

[106] G. Kowal, A. Lazarian, E. T. Vishniac and K. Otmianowska-Mazur, ApJ, **700**, 63 (2009).

[107] N. F. Loureiro *et al*., Mon. Not. R. Astron. Soc. 399, L146 (2009).

[108] Y. M. Huang and A. Bhattacharjee, Phys. Plasmas **17**, 062104 (2010).

[109] C. S. Ng and S. Ragunathan, ASP Conference Series, Vol. 444, edited by N. V. Pogorelov, E. Audit, and G. P. Zank (2011) pp. 124–129.

[110] Z. B. Guo, P. H. Diamond, and X. G. Wang, Astrophys. J. **757**, 173 (2012).

[111] H. Karimabadi and A. Lazarian, Phys. Plasmas **20**, 112102 (2013).

[112] Jiquan Li and Y. Kishimoto, Phys. Plasmas **19**, 030705 (2012).

[113] F. Militello *et al.*, Phys. Plasmas **15**, 050701 (2008).

[114] Jiquan Li *et al.*, Nucl. Fusion **49**, 095007 (2009).

[115] M. Muraglia *et al., Phys. Rev. Lett.* **103**, 145001(2009).

[116] H. R. Strauss, *"Nonlinear three-dimensional magnetohydrodynamics of noncircular tokamaks"*, Physics of Fluids, vol. 19, 134-140, 1976.

[117] J.P Friedberg: *Ideal Magnetohydrodynamics,* Plenum Press, New York, (1987).

[118] R. D. Hazeltine, J. D. Meiss, *Plasma Confinement*, Courier Dover Publications, 2003.

[119] J. Goedbloed, R. Keppens and S. Poedts, *"Advanced Magnetohydrodynamics"*, Cambridge Press, 2010.

[120] S. I. Braginskii, *Transport processes in plasma*. Rev. Plasma Phys. **1**, 205–311, 1965.

[121] N. F. Loureiro, *"Studies of Nonlinear Tearing Mode Reconnection"*, PhD thesis, Imperial College of London, 2005.

[122] H. P. Furth, P. H. Rutherford and H. Selberg, *"Tearing mode in the cylindrical tokamak"*, Phys. Fluids **16**, 1054 (1973).

[123] B. Coppi *et al.*, *Resistive internal kink modes.* Sov. J. Plasma Phys. **2**, 533–35, 1976.

[124] M. Abramowitz and I.A. Stegun. *Handbook of mathematical functions*. Dover Publications, Inc., New York, 1970.

[125] A. Ali, Jiquan Li, Y. Kishimoto, Phys. Plasmas **21**, 052312 (2014).

[126] W. Park, D. A. Monticello, and R. B. White, Phys. Fluids **27**, 137 (1984).

[127] L. Ofman, P. J. Morrison and R. S. Steinolfson, Phys. Fluids B, **5**, 376‑387 (1993).

[128] R. J. La Haye, D. P. Brennan, R. J. Buttery and S.P. Gerhardt, Phys. Plasmas **17**, 056110 (2010).

[129] L. Ni, K. Germaschewski, Y. Huang, B. P. Sullivan, H. Yang and A. Bhattacharjee, Phys. Plasmas **17**, 052109 (2010).

[130] A. Ali, Jiquan Li, Y. Kishimoto, Phys. Plasmas (Accepted on March, 2015).

[131] S. Maeyama *et al.*, Phys. Plasmas **17**, 062305 (2010).

[132] T. S. Hahm *et al*., Tang Phys. Plasmas **6**, 922 (1999).

[133] W. Daughton *et al.*, Nature Phys. 7, 539 (2011).

[134] S. D. Baalrud *et al.*, Phys. Plasmas 19, 022101 (2012).